Inverse Estimation of the Cardiac Purkinje System from Electroanatomical Maps

Fernando Barber Miralles

DOCTORAL THESIS UVEG / December 2019
Programa de Doctorat en Tecnologies de la Informacio,
Comunicacions i Computacio

Directors of the thesis

Dr. Ignacio Garcia and Dr. Rafael Sebastian
Department of Computer Sciences

VNIVERSITAT DE VALÈNCIA

Directors

Dr. Rafael Sebastian Aguilar	Associate Professor Universitat de Valencia Valencia, Spain
Dr. Ignacio Garcia Fernandez	Associate Professor Universitat de Valencia Valencia, Spain

Review Committee (Main):

Prof. Javier Saíz Rodríguez	Universidad Politecnica de Valencia
Prof. Juan de Mata Domingo Esteve	Universitat de Valencia
Prof. Esther Pueyo Paules	Universidad de Zaragoza

Review Committee (Reserve):

Prof. Oscar Cámara Rey	Universitat Pompeu Fabra
Dr. Jose Felix Rodriguez Matas	Universidad Politecnica de Milan
Dr. Esther Durá Martínez	Universitat de Valencia

This work was carried out in the research group *Computational Multiscale Simulation Lab (CoMMLab)*, at the Departament de Informática of Universitat de Valencia, Valencia, Spain.

A mi familia.

Abstract / Resumen

Abstract Cardiovascular disease is the number one cause of mortality in the world, accounting for 17.7 million deaths each year, an estimated 31% of all deaths worldwide (World Health Organization (WHO) 2018). Ventricular arrhythmias are a major cause of sudden death, which accounts for approximately half of cardiac mortality. Some of those arrhythmias are attributed to the Purkinje network (PKN), which under certain conditions can generate both automatic and triggered focal rhythms, and its network configuration can sustain re-entrant circuits. Focal Purkinje triggers can serve as initial points of ventricular fibrillation in a wide spectrum of patients.

The management of cardiac electrical diseases is an expanding clinical activity. New non-invasive imaging and mapping technologies, allow to acquire high resolution clinical images (MRI, CT) that can be used to localize and characterize pathological cardiac tissue. Furthermore, electroanatomical navigating (EAM) systems, can aid electrophysiologist to find the sources of arrhythmogenic activity or circuits maintaining arrhythmia, and eliminate them by radio-frequency ablation (RFA).

Despite all the technical advances, overall clinical outcome for those diseases is still perceived as suboptimal, with long-term treatment success rates in the range of 60 to 65%. Therefore, there is a compelling need to improve clinical outcomes for the benefit of the patients and the healthcare system.

The area of computational biophysical modeling has already started to penetrate in clinical environments in a few technologically advanced research oriented hospitals in the world. The main objective of these techniques is the development of realistic 3D models of different organs, such as the heart, that include, with a high degree of detail, genetic characteristics of the ionic currents, their mutations, the electrophysiological characteristics of the different cardiac cell types, the anatomical structure of cardiac tissues, and in

general of the human body. Following, the models are used to simulate the heart function, e.g., electrophysiology, to try to stratify patients or improve therapy planning and delivery.

Computer-based approaches are still facing several challenges that prevent their complete penetration into clinical environments. Arguably, one of the most important obstacles is the time and expertise required to build a patient-specific model of the heart, even if all necessary clinical data are available. In that sense, one of the model components that has remained largely elusive to modelers has been the PKN, which is key for cardiac electrophysiology. The main reason is that due to its small dimensions there is no clinical technique with enough resolution to allow its visualization in vivo.

The main purpose of this thesis is to develop a methodology able to inversely estimate a reduced PKN of patient from his EAM. That involves, first, finding in the EAM the sources of electrical activation, so called Purkinje-myocardial junctions (PMJs), and, following, finding the structure that interconnects those PMJs and reproduces the patient sequence of activation. In summary, the main contributions of this thesis are:

- Methodology to estimate the PMJs, or the sources of electrical activity, from a 3D representation of the ventricular endocardium provided by an EAM. The method developed can process directly the data acquired by an electrophysiologist in the Cathlab, re-annotate the time samples, and obtain the PMJ locations and activation times, explicitly considering noise in the samples.

- Methodology to estimate the patient PKN from the estimated PMJs, that is able to reproduce the patient's sequence of electrical activation with a minimal error. The method has been validated on synthetic EAMs as well as in 28 real EAMs, showing errors of a few milliseconds. In addition, an estimated PKN has been used to simulate the virtual ECG of a patient, showing a good match with the clinical one.

  In conclusion, I have developed and validated a methodology that permits the estimation of a patient's PKN with small errors in the sequence of activation, that can be used to personalize biophysical simulations of the heart or aid electrophysiologist in the planning of RFA interventions.

Resumen Las enfermedades cardiovasculares son la primera causa de mortalidad en el mundo, con 17.7 millones de muertes cada año, aproximadamente el 31% de las muertes en todo el mundo (Organización Mundial de la Salud (OMS) 2018). Las arritmias ventriculares son una causa importante de muerte súbita, que representa aproximadamente la mitad de la mortalidad cardíaca. Algunas de esas arritmias se atribuyen a la red de Purkinje (PKN), que bajo ciertas condiciones puede generar ritmos focales automáticos, y su configuración de red puede sostener circuitos eléctricos reentrantes. Los ritmos focales originados desde la red de Purkinje pueden servir como puntos de inicio en casos de fibrilación ventricular en un amplio espectro de pacientes.

El manejo de las enfermedades eléctricas cardíacas es un área clínica en expansión. Las nuevas tecnologías de imágenes y mapeo no invasivas, permiten adquirir imágenes clínicas de alta resolución (MRI, CT) que se pueden utilizar para localizar y caracterizar el tejido cardíaco patológico. Además, los sistemas de navegación electroanatómica (EAM) pueden ayudar al electrofisiólogo a encontrar las fuentes de actividad o circuitos arritmogénicos que mantienen la arritmia y eliminarlos mediante ablación por radiofrecuencia (RFA).

A pesar de todos los avances técnicos, los tratamientos clínicos para esas enfermedades todavía se perciben como subóptimos, con tasas de éxito del tratamiento a largo plazo en el rango de 60 a 65%. Por lo tanto, existe una necesidad imperiosa de mejorar los resultados clínicos en beneficio de los pacientes y el sistema de salud.

El área del modelado biofísico computacional ha comenzado a penetrar en entornos clínicos en unos pocos hospitales tecnológicamente avanzados y orientados a la investigación en el mundo. El objetivo principal de estas técnicas es el desarrollo de modelos 3D realistas de diferentes órganos, como el corazón, que incluyen, con un alto grado de detalle, características genéticas de las corrientes iónicas, sus mutaciones, las características electrofisiológicas de los diferentes tipos de células cardíacas, la estructura anatómica de los tejidos cardíacos y, en general, del cuerpo humano. A continuación, los modelos se utilizan para simular la función cardíaca, por ejemplo, electrofisiología, para tratar de estratificar a los pacientes o mejorar la planificación y ejecución de la terapia.

Los enfoques por computador aún se enfrentan a varios desafíos que impiden su penetración completa en entornos clínicos. Podría decirse que uno de los obstáculos más importantes es el tiempo y la experiencia necesarios para

construir un modelo del corazón personalizado a paciente, incluso si todos los datos clínicos necesarios están disponibles. En ese sentido, uno de los componentes del modelo que se ha mantenido elusivo a los modeladores ha sido la PKN, que es clave para la electrofisiología cardíaca. La razón principal es que debido a sus pequeñas dimensiones no existe una técnica clínica con resolución suficiente para permitir su visualización in vivo.

El objetivo principal de esta tesis es desarrollar una metodología capaz de estimar inversamente un PKN reducido de paciente a partir de su EAM. Eso implica, primero encontrar en el EAM las fuentes de activación eléctrica, llamadas uniones de Purkinje-miocardio (PMJ), y seguir la estructura que interconecta esos PMJ y reproduce la secuencia de activación del paciente. En resumen, las principales contribuciones de esta tesis son:

- Metodología para estimar los PMJ, o las fuentes de actividad eléctrica, sobre una representación 3D del endocardio ventricular, proporcionada por un EAM. El método desarrollado puede procesar directamente los datos adquiridos por un electrofisiólogo en el Cathlab, volver a anotar los tiempos en las muestras adquiridas y obtener las ubicaciones de los PMJs y los tiempos de activación, considerando explicitamente ruido en las muestras.

- Metodología para estimar el PKN del paciente a partir de los PMJ estimados, que es capaz de reproducir la secuencia de activación eléctrica del paciente con un error mínimo. El método ha sido validado tanto en EAM sintéticos como en 28 EAM reales, mostrando errores de unos pocos milisegundos. Además, se ha utilizado un PKN estimado para simular el ECG virtual de un paciente, donse se observa coincidencia entre el ECG real y el simulado.

  En conclusión, he desarrollado y validado una metodología que permite la estimación de la PKN de un paciente con errores mínimos en la secuencia de activación, y que puede usarse para personalizar simulaciones biofísicas del corazón o ayudar al electrofisiólogo en la planificación de intervenciones de RFA.

Acknowledgements

There are many people who I want to thank, that helped in one way or another to make this thesis a reality. Specially my thesis directors Rafael Sebastian, who gave me an interesting topic for the thesis and introduced me in this world of computational biophysical modeling and simulation, and Ignacio García, who always helped me with the mathematical foundations of this work. A very important role was also played by Miguel Lozano, my tutor, specially with the beginning of the work. With all three I had fruitful discussions about the algorithms presented in this thesis. Without them this thesis would not have been possible.

I also want to thank all the people in COMMLAB group, since here I have always felt a friendly and supportive environment. Finally, a special thank to Alejandro, who helped me in the processing of real data.

The Computer Science Department, where this work has been carried out, a place where I have good friends and colleagues. And I also want to thank Vicente Cavero for some discussions and ideas at lunch time.

And finally to my family, my wife Lara and my daughter Sofía, for their support and for the time I sometimes couldn't spent with them. And my parents, for all the help throughout my life.

Contents

1 Introduction **1**
- 1.1 Motivation . . . 2
- 1.2 Objectives . . . 4
- 1.3 Outline of the thesis . . . 5

2 Literature Review: Clinical and Computational Cardiac Electrophysiology **9**
- 2.1 Anatomy and function . . . 10
- 2.2 The cardiac conduction system . . . 12
- 2.3 Cardiac arrhythmias . . . 18
- 2.4 Electroanatomical mapping systems . . . 19
- 2.5 Catheter ablation . . . 20
- 2.6 Biophysical modeling of the heart . . . 21

3 Inverse Estimation of Sources of Electrical Activation on a two-dimensional tissue Sheet **29**
- 3.1 Introduction . . . 31
- 3.2 PMJ estimation method . . . 32
  - 3.2.1 Algorithm description . . . 35
  - 3.2.2 Discussion of the method . . . 36
- 3.3 Performance Evaluation . . . 38
  - 3.3.1 Methodology . . . 39
- 3.4 Results and discussion . . . 41
- 3.5 Conclusions . . . 44

4 Estimation of Purkinje-Myocardial Junctions **47**
- 4.1 Introduction . . . 49
- 4.2 Material and methods . . . 50

4.2.1 PMJ characterization . . . 50
4.2.2 Algorithm description . . . 53
4.2.3 Experiments . . . 58
4.2.3.1 Euclidean, 2-dimensional scenarios . . . 58
4.2.3.2 3-Dimensional human ventricles . . . 59
4.3 Results and discussion . . . 60
4.4 Conclusions . . . 70

5 Estimation of Personalized Minimal Purkinje Systems 71
5.1 Introduction . . . 73
5.2 Material and methods . . . 74
5.2.1 Patient Data . . . 74
5.2.2 EAM processing . . . 76
5.2.3 Synthetic data . . . 77
5.2.4 Estimation of the PMJs . . . 78
5.2.5 Estimation of PKN . . . 79
5.2.6 Biophysical Simulations . . . 81
5.3 Results . . . 82
5.3.1 Estimation of PKN from synthetic data . . . 82
5.3.2 Estimation of PKN from EAMs . . . 89
5.3.3 ECG simulation . . . 94
5.4 Discussion . . . 95
5.5 Conclusions . . . 98

6 Conclusions and Future Work 101
6.1 Summary . . . 102
6.2 Main findings . . . 103
6.3 Contributions . . . 105
6.4 Limitations . . . 106
6.5 Future Work . . . 107

7 Publications 109

A Appendix 111
A.1 Complete catalogue of PMJ estimation results from synthetic PKNs . . . 112
A.2 Additional PKN models estimated from synthetic data and patient EAMs . . . 121

Bibliography 125

List of Figures

2.1 Diagram of Heart Anatomy 11
2.2 Gross macroscopic Anatomy of the Cardiac conduction system . 13
2.3 Example of an EAM 20

3.1 The relationship between PMJs and measurement points 33
3.2 Two different measurement point sets, and their corresponding Delaunay triangulations 34
3.3 Voronoi region containing three measurement points 38
3.4 Example of generated synthetic trees 39
3.5 Solutions provided for scenario B3D4 and B3D6 41
3.6 Results for a single main branch, and for three main branches. . 43
3.7 Number of PMJs detected and mean absolute error. 44
3.8 Estimation results for scenarios B1D2 and B3D6 45
3.9 Results for the gradient method. 45

4.1 Distribution of the values of a_i for a simulated scenario 52
4.2 Simplified grid scenario. 53
4.3 Candidate Source Points after the application of Algorithm for two real sources with a deviation in the error of 0.5ms and 1.5ms. 56
4.4 2-dimensional scenarios with random set of measurement points, real sources and location of estimated source points. 59
4.5 Purkinje tree models developed with an increasing number of PMJs and PMJ density. 60
4.6 Absolute error for scenarios B3D2 and B3D4 with different number of measurement points and a standard deviation error. . . . 62
4.7 Estimation in low PMJ density model. 66
4.8 Spatial distribution of LAT errors. 66
4.9 Plots of the absolute error for 5 different scenarios in increasing order of PMJs density. 67

4.10 Plots of the distance from estimated PMJs to real PMJs for 5 different scenarios in increasing order of PMJs density. 68

5.1 Example of EAM data for patient P12 75
5.2 LV original EAMs and re-annotated EAM, projected into a 2D unitary disk 77
5.3 Graphical results for estimation of synthetic model PK3 with Gaussian error $\sigma = 0.5$ 83
5.4 Detailed comparison of PK3 with different Gausian errors in the samples 84
5.5 PKN estimated from patient P2 LV EAM using different conduction velocities (CVs) 91
5.6 Comparison between projected LV LAT maps 92
5.7 Comparison of PKNs estimated from two different EAM studies on the same patient 93
5.8 Comparison between Simulated LAT and EAM for P12 94
5.9 Comparison between real and simulated ECG of patient P12 . . 95

A.1 Plots of the absolute error for scenarios PK1 to PK8. 115
A.2 Plots of the absolute error for scenarios PK9 to PK16. 116
A.3 Plots of the absolute error for scenarios PK17 to PK20. 117
A.4 Plots of the distance from estimated PMJs to real PMJs for scenarios PK1 to PK8. 118
A.5 Plots of the distance from estimated PMJs to real PMJs for scenarios PK9 to PK16. 119
A.6 Plots of the distance from estimated PMJs to real PMJs for scenarios PK17 to PK20. 120
A.7 Complete views for estimated and real synthetic PK3. 121
A.8 Estimated PKN for P1 LV EAM for different CVs. 122
A.9 Estimated PKN for P1 RV EAM for different CVs. 122
A.10 Estimated PKN for P2 RV EAM for different CVs. 123

List of Tables

4.1 Results for 2-dimensional scenarios with 1000 measurement points and Gaussian noise with a standard deviation of $\sigma = 0.5$ms and $\sigma = 2.5$ms. 61
4.2 Information about six representative 3-dimensional scenarios. . . 65
4.3 Results for six representative 3-dimensional scenarios with 1000 measurement points and Gaussian noise with standard deviation of 0.5 and 2.5. 65

5.1 Clinical EAM data 75
5.2 Description of Synthetic PKNs. 78
5.3 Estimation of the PKN directly from the real PMJs without error. 86
5.4 Estimation of the PKN from estimated PMJs and error $\sigma = 0.5ms$. 86
5.5 Estimation of the PKN from EAMs. 88

A.1 Information and results for all 3-dimensional scenarios with 1000 measurement points and Gaussian noise with standard deviation of 0.5 113
A.2 Information and results for all 3-dimensional scenarios with 1000 measurement points and Gaussian noise with standard deviation of 2.5 114

Acronyms

AF	Atrial fibrilation
AHA	American Heart Association
AP	Action potential
APD	Action potential duration
AVN	Atrioventricular node
BSPM	Body surface potential map
CCS	Cardiac conduction system
CV	Conduction velocity
EAM	Electro-anatomical map
ECG	Electrocardiogram
HB	His bundle
LAT	Local activation time
LBB	Left bundle branch
LA	Left atrium
LV	Left ventricle
MRI	Magnetic Resonance Imaging
NICD	Nonspecific intraventricular conduction delay
PKN	Purkinje Network
PMJ	Purkinje-myocardial junction
QCM	Quasi-conformal projection
RA	Right atrium
RV	Right ventricle
RFA	Radiofrequency ablation
VF	Ventricular fibrilation
VT	Ventricular Tachycardia

1

Introduction

1.1 Motivation

Personalized medicine, computational biology and the medical device industry are growing at an incredibly rapid pace. Our overall understanding of patho-physiology and the molecular basis of diseases steadily increases, as does the number of available therapies to treat specific health problems. This remains particularly true in the field of cardiovascular care. With this rapid growth rate in cardiac medicine, clinicians and biomedical engineers alike have been challenged to either re-engineer or continue looking for sources of concise information.

However, the epidemiological burden imposed on the society by cardiac disease requires the development of novel advanced cost-effective methodologies that optimize both therapy planning and delivery. These new tools have to build upon current advanced clinical systems that allow to explore with a high level of detail cardiac anatomy and function *in vivo*. For instance, it is possible to non-invasively explore cardiac anatomy by means of computed tomography (CT) or magnetic resonance imaging (MRI) [1], or assess tissue damage after an infarct by means of delay-enhanced MRI (de-MRI) [2]. In addition, electroanatomical mapping systems (EAM), introduced in the last decade, allow to analyze patient's electrical function, and complement the information provided by the electrocardiogram (ECG), to treat complex arrhythmias. All those technologies have rapidly penetrated in clinical environments and have become part of current international guidelines for management of arrhythmia [3].

Despite advances in medicine, cardiac arrhythmias are still one of the leading causes of mortality in Europe and impose a huge healthcare burden on society. Long-term success rates for several cardiac disease such as ventricular tachycardia (VT) or ventricular fibrillation (VF) remain too low due to the number of variables and interactions underlying those pathological processes. The mechanisms that govern initiation and maintenance of certain arrhythmias are highly complex, dynamic, and involve interactions across multiple temporal and spatial scales, leading to unpredictable outcomes at the organ level. In addition, the amount of disparate data that has to be considered by electrophysiologist is overwhelming, and very difficult to integrate to stratify patients or optimize therapy planning and delivery. As a consequence, the overall clinical outcome in such therapies is still perceived as sub-optimal, with success rates in the range of 60% to 65%. It is necessary to develop novel methodologies and tools that help us to gain

understanding in the pathophysiology of the heart, and at the same time serve to improve patient management, therapy planning and delivery.

Modeling and simulation of cardiac electrophysiology and arrhythmias have emerge as a new approach not only in hypothesis-driven research at various levels of integration, but also in providing the framework for the unification of diverse experimental findings [4]. Those models can integrate information on cardiac physiology at various scales and allow to carry out detailed biophysical simulations of cardiac electrophysiology including pathological substrates [5]. Therefore, advanced information on disease and its evolution is within clinician's reach, who could apply novel therapeutic strategies to treat patients. Even though the increase of computational power has open the possibility of translating those new models into clinical environments, they have not penetrated yet due to a number of challenges, such as the complexity of personalizing the models to specific patients, or the inclusion of key heart substructures [6]. If a solution for those challenges is found, simulations could be used to build and test physical prototypes, or carrying large clinical trials, which makes this technology an interesting alternative.

In the current clinical and modeling literature, there are some key structures of the heart which cannot be observed for a specific patient, but still play a fundamental role in cardiac electrophysiology and arrhythmias. One of such structures is the cardiac conduction system (CCS), and in particular the distal section called the Purkinje network (PKN) [7]. It is known that, under pathological conditions, the PKN is responsible for the triggering and maintenance of deadly cardiac arrhythmias such as ventricular fibrillation (VF) [8, 9]. Since currently there is not a reliable technique to extract the PKN from clinical data *in vivo*, it is not usually incorporated into patient-specific models of the heart, nor available for electrophysiologists during interventions such as RFA. Being able to extract and incorporate the PKN in a computational model of the heart would enable to go one step beyond towards electrophysiology personalization obtaining more accurate simulations of cardiac electrophysiology. Moreover, fusing this information into current EAMs, electrophysiologist could have additional information, therefore, improving therapy planning and optimization of RFA or cardiac resynchronization therapy (CRT).

1.2 Objectives

The main aim of this thesis is to develop a methodology to estimate for a given patient his personalized PKN from an EAM acquired by an electrophysiologist in the Cathlab. For this, an inverse estimation methodology has been developed to obtain automatically the PKN, which has been evaluated on synthetic and real clinical data. These novel technology is expected to improve the accuracy of personalized biophysical simulations of cardiac electrophysiology, as well as to provide new information to electrophysiologists to plan RFA interventions.

This overall objective can be divided in the following goals:

- To develop a methodology to estimate the sources of electrical activity from local activation maps on synthetic 2D tissue models.
- To develop a methodology to estimate the PMJ locations and activation times from synthetic 3D tissue models of the endocardium, including noise in the samples.
- To develop a methodology to estimate the PMJs and PKN from EAMs acquired from real patients in sinus rhythm.

To achieve the first goal, an algorithm to build simplified fractal-based PKN was developed. It could construct PKN models with different branching depth, so that the local complexity of branches and the density of PMJs was variable. The algorithm was used to create a set of configurations on a 2D plane representing a sheet of tissue. In addition, since the real data would consist in a set of randomly distributed samples from a patient's heart, I sampled the sheet model randomly and obtained local activation information for each sample. In order to generate that data, the synthetic PKN, and in particular the PMJs, were used to simulate the sheet electrical activation sequence.

The second goal of the thesis involved an improvement of the method to work with realistic computational domains and data. In that line, I obtained a left ventricular endocardial anatomy from a previously segmented patient heart, and meshed it with triangles. Following, I used a methodology based on L-systems and physiological rules, to create a set of 20 PKN which showed complex configurations, including loops, and a variable density of

PMJs, which were non-homogeneously distributed. For each PKN scenario, I generated on the left ventricular (LV) mesh the corresponding activation sequences, and subsequently I sampled them to emulate a virtual EAM. At this point, I included Gaussian noise in all the sampled data to mimmic the types of error that we could find in real clinical data. Those simulations helped us to validate the PMJ estimation methodology in more realistic scenarios and assess its accuracy and main limitations.

The third goal wrapped up the two previous by extending the methodology to estimate not only the PMJs but also the PKN structure that interconnects them. For that purpose, an iterative algorithm that takes as an input an EAM and a set of estimated PMJs was implemented. The method connects all the estimated PMJs to a branching structure that extends from the His bundle, optimizing the local activation times at the PMJs by calculating geodesic paths on the endocardial mesh between PMJs and the PKN. The accuracy of the complete method was studied on both synthetic PKN and real EAMs. To further validate the results a biophysical model for one of the patients was constructed and used to simulate the sequence of activation on the ventricles using the estimated PKN. In addition, the forward problem in electrophysiology was calculated, obtaining the virtual ECG that can be compared with the one recorded on the patient.

The methodological and clinical problems tackled in this thesis are challenging and are of great interest, not only for modelers but also for electrophysiologists. In the last years only a few works have proposed approaches to deal with this problem, but never with the goal of obtaining patient-specific solutions. Therefore, the work can be considered a novel contribution to the current state-of-the-art.

1.3 Outline of the thesis

After this chapter, the rest of the thesis is organized as follows.

Chapter 2. Presents the background about heart physiology required to understand the importance of the PKN for electrophysiologists and modelers. It also summarizes the most important concepts on heart anatomy and function, with special emphasis on the PKN, and links them with certain pathologies such as arrhythmias. Finally, it introduces the field of biophysical modeling of the heart for electrophysiology simulation, its requirements, its advantages and applications.

The importance of incorporating the PKN into a 3D patient-specific model of the ventricles for cardiac simulation is also discussed.

Chapter 3. I develop and present the methodology to inversely estimate PMJs on a continuous 2D tissue sheet. I create several synthetic simplified PKN on a 2D plane, and show the accuracy of the methodology for different PKN configurations, considering an increasing number of sample points. The simplified PKN configurations used have different properties, such as branching depth, number of PMJs (sources), and as a result different PMJ density. I conclude showing the number of PMJs properly estimated, and the errors in local activation time for each of the PKN configurations and density of sampling points.

Chapter 4. I extend the methodology previously described for continuous 2D sheets to be able to work on discrete 3D triangular meshes, similar to those obtained from EAMs systems. I solve the backward Eikonal problem on a mesh to estimate the location and activation time of PMJs from a discrete set of samples. To test the methodology, I build 20 complex branching PKN structures using L-systems, and estimate their PMJs subject to different levels of Gaussian noise on the samples. I present results of a simulation study to show the accuracy of the estimation method for different levels of noise, and for various PKN morphologies.

Chapter 5. I complete the pipeline including the methodology to estimate a PKN structure compatible with the estimated PMJs and the patient's EAM. The structure built for each case is the minimal PKN that reproduces the patient EAM with the smallest local activation time error. In addition, I estimate the optimal conduction velocity (CV) in the PKN for each potential structure, and derive general parameters. The methodology is first tested on a set of five representative synthetic PKN used previously to estimate PMJs. A qualitative analysis is provided to show errors in PKN morphology, as well, as errors related to the endocardial sequence of activation. Finally, the study is completed with the estimation of PKNs from real patient EAMs in sinus rhythm. I compare the local activation maps acquired in the cathlab with those obtained by simulations after estimating the PKN. In addition, the PKN model is further validated by building a patient-specific biophysical heart-torso model for one of the patients to simulate cardiac electrophysiology and obtain the virtual ECG, which is subsequently compared to that of the patient.

Chapter 6. This chapter summarizes the most important ideas and contributions of this thesis. I highlight the strengths and limitations, and propose future research directions.

2

Literature Review: Clinical and Computational Cardiac Electrophysiology

2.1 Anatomy and function

The heart is a complex organ responsible for pumping oxygenated blood into the vessels of the circulatory system. In humans, the heart is located in the middle of the chest surrounded by the lungs, within a compartment called the mediastinum. It has a cone shape and a mass of 250-350 grams, which is approximately the size of a fist [10]. The heart and the roots of the great vessels are sheltered by a double-walled sac called the pericardium that encloses them and provides lubrication.

It is divided in four chambers, two atria and two ventricles with differentiated functions (see Figure 2.1). The upper chambers collect blood while the lower chambers pump the blood to the lungs and the body. As depicted in Figure 2.1, the right atrium (RA) receives through the superior and inferior vena cava oxygen-depleted blood from the systemic circulation. From the RA the blood flows to the right ventricle (RV) through the tricuspid valve and is pumped out to the pulmonary circulation during ventricular systole, where it is oxygenated and released from carbon dioxide. Oxygenated blood is returned from the pulmonary circulation into the left atrium (LA) through the pulmonary veins, and then passes to the left ventricle (LV) through the mitral valve where it is pumped away from the heart through the aorta into the systemic circulation. In summary, the right heart (RA and RV) is responsible for collecting oxygenated-poor blood and pumping it to the lungs, while the left heart (LA and LV) is responsible for collecting oxygenated-rich blood from the lungs and pumping it to the rest of the body. The LV is also responsible to pump blood to the heart circulatory system. During the diastolic period the ventricles are filled with blood, while during the systolic period the ventricles contract and the blood is ejected. Note that there is a one-way blood flow in the heart thanks to the four heart valves.

The ventricles present a more regular and simpler morphology than the atria in general terms. The gross anatomy of the right heart is considerable different from that of the left heart, yet the pumping principles of each are basically the same. The LV has the shape of a cone with the RV hugging it. The wall that separates the ventricles is called the interventricular septum, while the wall opposing the septum is the so-called lateral or free wall. The lowest area of the ventricles is named the apex, and the area that is in contact to the atria is the base. The lateral wall is thicker at the base of the heart than in the apical area.

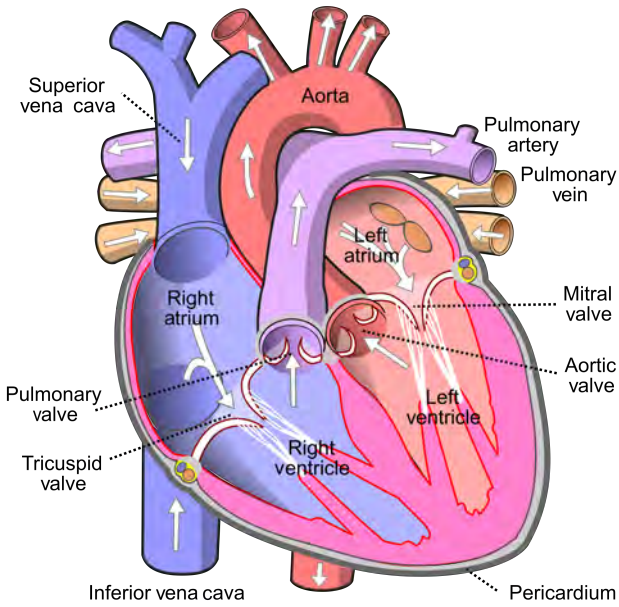

Figure 2.1: Description of heart Anatomy including its main components. Image from Wikimedia Commons (CC BY-SA 4.0).

The ventricular walls are formed by three layers, the endocardium (inner), the myocardium (middle), and the epicardium (outer). The endocardium is a thin layer that protects the heart chambers, valves, chordae tendinae and papillary muscles, and is primarily made up of endothelial cells. The (mid-)myocardium is the largest in volume compared to endocardium and epicardium, and also the main responsible for the heart contraction. The RV is characterized by an irregular endocardium with abundant trabeculae carneae. Trabeculae carneae are irregular muscular tissue blocks with tubular shape which project from the ventricular inner surfaces. This feature allows to distinguish morphologically the endocardial surface of the ventricles, because the RV presents thick trabeculae, while in the LV they are thinner and crisscross in a more organized way.

The effective pumping action of the heart requires a precise coordination of the myocardial contractions (millions of cells), that is initiated by electrical excitatory impulses. The electrical currents generated in the heart also spread to other tissues in the body, and can be recorded on the torso surface, which provides the electrocardiogram (ECG). Alterations in the cardiac

impulse can lead to cardiac arrhythmia, a condition in which the heart rhythm is irregular and beats systematically faster or slower than the normal range of 60-100 beats per minute at rest.

2.2 The cardiac conduction system

Heart contraction results from the precise coordination of cardiac cells, and this is accomplished via the conduction system of the heart. Contractions of each cell are normally initiated when electrical excitatory impulses (action potentials) propagate along their surface membranes. The myocardium can be viewed as a functional syncytium; action potentials from one cell conduct to the next cell via the gap junctions.

A thorough understanding of the anatomy and function of the cardiac conduction system is important for designing cardiovascular devices, procedures, and optimize treatments. The gross anatomy of the cardiac conduction system (CCS) has been widely studied, specially its suprahisian (above the His bundle (HB), see Figure 2.2) structures owing to their clearer implications in supraventricular rhythm disorders and the complexity of the CCS at distal sections (see Figure 2.2).

The fundamental function of the specific cardiac conduction tissue is to trigger and spread at fast speeds the electrical impulse responsible for the heartbeat, maintaining the heartbeat at an average of 60-90 beats per minute in an adult healthy heart.

The different elements of the specific cardiac conduction system are responsible for the generation and maintenance of the cardiac cycle. The effectiveness of the cardiac contraction depends on the coordinated sequence of the different events of the cardiac cycle. The atrial contraction must happen before the ventricular, which in turn must first occur at the level of the papillary muscles (attached to the valves), extending from there to the ventricular apex and then to the ventricles and pulmonary and aortic outflow tract.

The CCS comprises the sino-atrial node (SAN), the heart's pacemaker, located in the atria; the atrio-ventricular node (AVN), that communicates the electrical impulse from the atria to the ventricles; the HB and the right (RBB) and left bundle branches (LBB) that diverge the impulse to both ventricles through the septal wall; and finally the Purkinje network (PKN), that functions as a highway that spreads at fast speed the electrical impulse

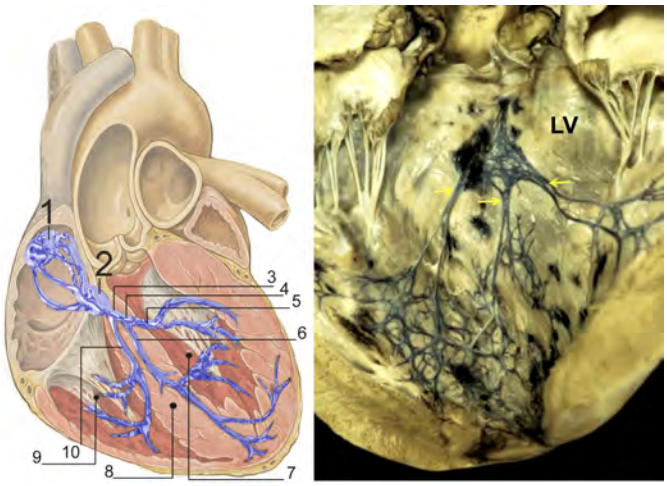

Figure 2.2: Gross macroscopic Anatomy of the Cardiac conduction system. Left panel shows a simplified representation of the cardiac conduction system (blue) with the most important components. Labels correspond to the following substructures; (1) Sino-atrial node (SAN); (2) Atrio-ventricular node (AVN); (3) His Bundle; (4) Left bundle branch (LBB); (5) Posterior LBB; (6) Anterio LBB; (7) Left Ventricle (LV); (8) Septal wall; (9) Right ventricle (RV); (10) Right bundle branch (RBB). Right panel shows a picture of a calf ventricle where the Purkinje networks is reveal thanks to a micro-injection of Chinese ink. Left image adapted from Wikimedia Commons (CC BY-SA 4.0), and right image courtesy of Prof. Damian Sanchez-Quintana.

across the ventricular muscle, and connects to the working myocardial tissue at discrete locations called PMJs [11]. Those components are formed by three cell types morphologically different from the cells that make up the "working" myocardium: P cells, transitional cells and Purkinje fibers.

The electrical impulse is generated in the P cells located in the SAN, and it is transmitted to the AVN, where a conduction delay occurs, which allows the atria to contract completely before the ventricles start to contract. The depolarizing impulse is transmitted then to the bundle of His and its branches and, finally, the PKN, which distributes the cardiac impulse to the apex and from there extends along the ventricular walls, thus causing the ventricular contraction. The transitional cells connect the PKN to the working myocardial cells.

The sinus node

The sinus node or SA node (SAN) is also called the Keith and Flack node because it was first described by both in 1907 [12]. It is the pacemaker of the heart, that is, its cells are responsible for the start of the cardiac impulse. It is situated in roughly the same location in all hearts: high on the RA wall near the junction of the superior vena cava and the RA. At the boundaries of the node in the human heart, short areas of histologically transitional cardiomyocytes insert into the musculature of the terminal crest. Conduction spreads through the atria to the AVN and then to the HB, which is the normal conducting pathway from the atria to the ventricles [13].

During an extended period of time, it was believed that a specialized insulated pathway existed between the sinus node and the AVN. In reality it does not exist, however, there are preferential conduction pathways that permit to transmit rapidly the electrical impulse generated by the SAN to the AVN. The main pathways are the crista terminalis and the margins of the oval fossa. The pectinate muscles also transport the electrical impulse at higher speeds within the RA, while the Bachmann's bundle is the preferential fast connection towards the LA.

The Atrioventricular node and conduction axis

The AVN was first described by Sunao Tawara in 1906 [14], who also clarified the existence of a bundle of connective tissue described by His in 1893. Tawara also described for the first time how the bundle of His was continued with the ventricular PKN.

Anatomy

The atrioventricular conduction axis has atrial, penetrating, and ventricular components [15]. The HB continues as a short non-branching segment that gives rise to the fascicles of the LBB (see Figure2.2, left for a schematic representation). The RBB takes its origin from the most distal left-sided fascicles, located beneath the septum on its left side, and courses buried through the septum towards the RV. The right branch runs through the right side of the septum until reaching the base of the septal papillary muscle of the RV. Subsequently, it penetrates the septomarginal trabecula and extends from the septal wall of the RV to its anterior wall, through the

moderating band. Finally, it is divided into the Purkinje subendocardial network. On the other hand, the specialized cardiomyocytes of the LBB fan out subendocardially giving rise to three fascicles, superior, septal and inferior that run on the LV ((see Figure 2.2, right, for a frontal visualization of the three main fascicles).

Activation sequence

Toward the end of atrial depolarization, the excitatory signal crosses the AVN. Since the atria and ventricles are electrically isolated from each other by dense connective tissue rings, the AVN located in the triangle of Koch is the only conduction pathway between upper and lower chambers [16]. The AVN has the mission of delaying the electrical signal before transmitting it to the ventricle. This will allow the atria to completely pump the blood into the ventricles, since simultaneous contraction would cause inefficient filling and backflow. It is worth to mention that in pathological conditions (e.g. Wolff-Parkinson-White syndrome) there exist aberrant paths between the atria and ventricles such as the bundle of Kent. The AVN also presents depolarization automaticity, but with a slower frequency (40 to 50 beats per minute) than the SAN.

The Purkinje Network

The goal of the Purkinje network is twofold, to act as a fast conduction pathway that reduces the total activation time of the ventricles, and to synchronize and coordinate the activation pattern. Following I review its anatomy and function.

Anatomy

After the RBB and LBB span and divide into the main fascicles, they become a complex and extensive network that furcates and anastomose subendocardially on both ventricles, forming the PKN. Initially the fascicles direct towards the base of the papillary muscles, since they have to be electrically activated before the ventricle contracts [15]. There have been also reported morphological differences in the HB and bundle branches configuration between individuals [17].

In both ventricles the PKN forms a complex mesh of branches that emerge from the fascicular branches and extend subendocardial throughout the ventricles transporting the electrical impulse at fast speeds, and triggering the activation of the rest of the myocardium at discrete locations [18, 19]. Note that both the HB and the Purkinje strands are surrounded by a perifascicular sheath of connective tissue that isolates them electrically from working cardiomyocytes until transitional areas where they are connected [15]. The perifascicular connective tissue sheath is important in organizing the contraction of the myocardium by preventing lateral spread of conduction and by permitting transmission of the impulse only at the termination of the Purkinje fibers, that is, the so called Purkinje-myocardial junctions (PMJs) [20]. At the PMJs, the perifascicular sheath is lost, and the electrical impulse can travel from the PKN into the working myocardial tissue.

The PKN has only been described macroscopically from photographs, microCT imaging, and microscopically from histological samples, in different species such as rabbit [21], pig [22] or human [23]. However, the full reconstruction of the PKN in 3D has never been achieved in humans or animals. The proximal sections have been macroscopically visualized using inks or specific markers (bovine, sheep, murine) [14, 18, 20], but only high resolution microscopy imaging can reveal the details of the system or the PMJs at distal locations, which reduces its scope of analysis. Therefore, in humans the distribution and number of PMJs remains elusive, although some histological studies have shed some lights in animals [22]. Note that, in human hearts the conduction system and PMJs have only been observed subendocardially, unlike other species such as ungulate hearts in which the system can run transmurally as far as the epicardium [22].

There is scarce information on PMJ density and distribution on the endocardium. Some studies suggest that the distribution of subendocardial PMJs and their coupling is spatially inhomogeneous, and that the junction regions themselves have variable degrees of electrical coupling [13]. Some detailed electrophysiology studies have shown the continuous coupling between the PKN and the myocardium, suggesting a more dense and complex network with thousands of PMJs [24]. In addition, from histological observations, there are large endocardial areas where PMJs would not be expected due to the lack of PK branches, such as the base of the ventricles and portions of the septum [25].

Activation sequence

In a healthy human heart, the PKN functions as a 'highway' placed in the inner cardiac surface, where the electrical signals travel fast up to the PMJs. At each PMJ the impulse enters the 'working' contractile myocardium, which slowly propagates the electrical signal as a wavefront activating the heart tissue. Once a given cell has been activated, it cannot be activated again during a certain period (effective refractory period) by a second electrical wavefront. As a result, not all PMJs are *functional*, in the sense that some might try to trigger cardiac tissue that has been already activated. Therefore, they have no practical effect, or their contribution is masked by other surrounding PMJs.

In the LV, myocardial activation triggered from the most proximal PMJs starts at a central area on the LV surface of the interventricular septum, and at the posterior paraseptal area at about one third of the distance from apex to base. These two initial activated areas spread and grow in size during 5ms to 10ms, and become confluent at 15ms to 20ms after the initial onset of excitation [26]. At this point, the depolarization wavefront has activated most of the endocardium, with exception of the posterobasal area, a middle lateral area, and an apical anterior area. Since the septum is initially activated from the LV, a wavefront spreads within the septum from left-to-right ventricle, and from apex-to-base. A breakthrough due to the PKN also occurs in the middle third of the RV septum before the wavefront initiated in the LV arrives, which produces a collision of both wavefronts within the septum.

Note that thanks to the PKN, the endocardium activates from different locations faster than it propagates from endocardium to epicardium. After 30 ms the wavefront has activated all the endocardium, except at the posterolateral area, and has arrived to the epicardium at some regions. The last area that activates in the LV is usually the posterolateral or the posterobasal. In the RV, the activation starts between 5ms to 10ms after the onset of the LV potential. The first region that activates is the anterior papillary muscle, and following both the septal and the lateral wall activate in parallel. Since the RV has a thin wall, the wavefront reaches the epicardium 20ms after the initial breakthrough. The last region that activates at around 60ms, is the pulmonary conus and the posterobasal area [26].

2.3 Cardiac arrhythmias

Cardiac arrhythmia is a condition in which the heart rhythm is irregular and beats systematically faster or slower than the normal range of 60-100 beats per minute at rest. Faster rhythms are called tachycardia, and slow rhythms bradycardia. It is considered an electrical disorder, which compromises cardiac mechanics and affects the heart pumping efficiency. The term cardiac arrhythmia covers a very large number of very different conditions. The most general symptom is the feeling of palpitations, or a pause between heartbeats, or in more severe cases shortness of breath, or chest pain.

The most common way to diagnose an arrhythmia is by evaluating the patients' ECG, which can be complemented by an eco-cardiographic study, and in specific cases with an EAM. Apart from the classification as a function of the heart rate in tachycardia and bradycardia, arrhythmia can be analyzed by mechanism. There are three basic mechanisms that can elicit heart tachycardia: automaticity produced by ectopic focus, re-entrant activity produced by rotors and spiral waves, and triggered activity produced by cell afterdepolarizations. Tachycardia might degrade into fibrillation due to the electrical changes at ionic level produced by sustained fast heart rhythms. With respect to the duration of the episodes they can be classified as paroxysmal, sustained, or permanent.

The ventricles can develop ventricular tachycardia due to a number of reasons that include coronary heart disease, aortic stenosis, cardiomyopathy, electrolyte problems, inherited channelopathies (e.g., long-QT syndrome), or a heart attack. Ventricular tachycardia is characterized by abnormal electrical impulses that originate in the ventricular conduction system, ischemic myocardium or scar tissue [27].

Clinically, the PKN structure is very relevant since it is responsible for the initiation and maintenance of life-threatening arrhythmias [28, 29]. For instance, it is known that some His-Purkinje system-related macro re-entry Ventricular Tachycardia (VT) are triggered or supported by the PKN, and that the ablation of specific PMJs or bundles can stop the arrhythmia [30, 31]. These ventricular tachy-arrhythmias can be called Purkinje-related arrhythmias, and include monomorphic VT, polymorphic VT, and ventricular fibrillation (VF). Purkinje-related monomorphic VTs are classified into distinct groups: i) verapamil-sensitive left fascicular VT; ii) Purkinje fiber-mediated VT post infarction, iii) bundle branch reentry (BBR) and interfascicular reentry VTs; and iv) focal Purkinje VT [32]. Note that,

these VTs usually occur in specific locations and have specific QRS morphologies. The VT mechanisms of i), ii) and iii) are macroreentry, whereas iv) is abnormal automaticity. In cases of idiopathic ventricular fibrillation (IVF), the main cause of unexplained sudden cardiac death, the majority of cases (up to 93%) are triggered by premature ventricular contractions (PVCs) that originate from the PKN [8, 9].

The treatment for sustained ventricular tachycardia is usually tailored to the specific person, depending on how frequently episodes occur, and his comorbidities. The most common treatments for arrhythmia include, the use of drugs (beta blockers, blood thinners), implantation of pacemakers and intra-cardiac defibrillators (cardiac resynchronization therapy), and surgery (radio-frequency ablation).

Radio-frequency ablation (RFA) is considered a potential first-line therapy for patients with idiopathic VT, because these VTs can be eliminated by ablation in a high percentage of patients. However, in some types such as focal Purkinje VT, the recurrence rate is around 29% [32], and there are several complications associated to ablation.

2.4 Electroanatomical mapping systems

EAMs are powerful tools since they provide electrophysiologists with the ability to map the three-dimensional anatomy of the heart and determine the cardiac electrical activity at any given mapped point. The system combines anatomical structure and electrophysiological data and displays the information in an easily readable, visual fashion [33].

The system consists of a moving mapping catheter with small magnetic sensors at the tip, a fixed sensor that acts as a reference point, a low magnetic field generating platform and a data acquisition and visualization system. When the moving catheter moves in a three-dimensional space, its location in relation to the fixed sensor is monitored by the system, with a resolution of < 1 mm [34]. By gating the acquisition of points in space to cardiac electrical activity, points representing both the location and the electrical activity in that location can be acquired and displayed on a computer screen. After acquiring a series of points, a three-dimensional representation is constructed, and can be displayed from any viewing projection (see Figure 2.3). The clinical applications of the system include defining the mechanisms of arrhythmias, designing ablation strategies, guiding ablations and improving

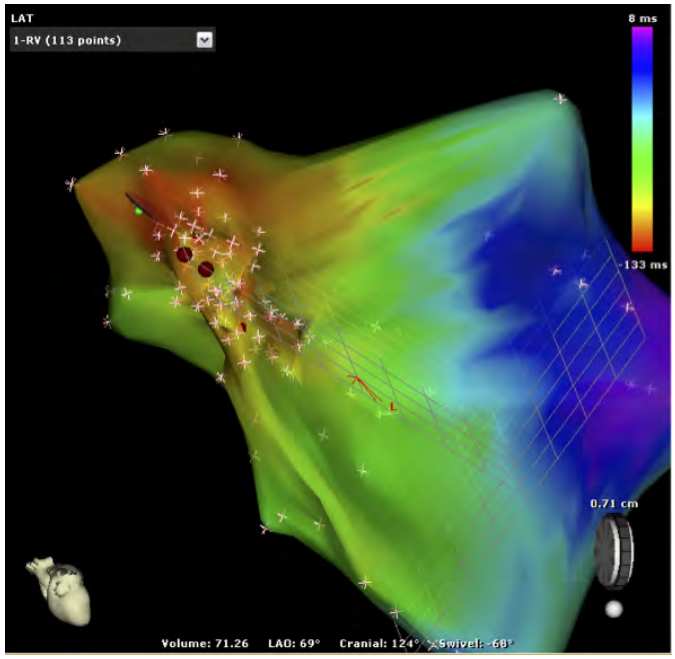

Figure 2.3: Example of an EAM of the RV, where colors correspond to the local activation times manually annotated by the technician, recorded *in vivo* on the endocardial walls using a catheter.

the safety of mapping and ablation procedures by allowing the location of critical cardiac structures such as the AVN and the HB [35, 36].

2.5 Catheter ablation

Catheter ablation is a minimally-invasive surgical procedure that aims to terminate a faulty electrical pathway in the heart of subjects prone to develop cardiac arrhythmias such as atrial fibrillation, atrial flutter, ventricular fibrillation, ventricular tachycardias or Wolff-Parkinson-White syndrome [37]. It involves introducing several flexible catheters through the femoral vein (or the subclavian vein), and advance them towards the heart chambers. Once inside the heart, catheters are used to induce the arrhythmia, which is subsequently stopped by applying local heating or freezing to ablate the abnormal electrical pathways.

The ablation basically has as a goal the creation of lesions in the tissue

that change the conduction patterns. Catheter ablation is recommended in people with no or little structural heart disease where rhythm control by medication or cardioversion fails to maintain normal heart rhythms (recurrent or persistent arrhythmia), or requires very long drug treatments that prolong for years [3, 38]. The procedure can be classified by energy source: radiofrequency ablation (RFA) and cryoablation.

Before the ablation is performed the electrophysiologist constructs a chamber EAM, that guides him towards the regions that need to be ablated. EAM allows operators to record intracardiac electrical activation in relation to anatomic location in a cardiac chamber of interest, during arrhythmia mapping. While originally applied towards relatively straightforward arrhythmias with a single discrete target site (such as AVN reentry or tachycardias associated with Wolff-Parkinson-White syndrome), they are increasingly being used to address more complex arrhythmias, including atypical atrial flutter, atrial fibrillation, and ventricular tachycardia. This latter group of rhythm disturbances is often associated with significant underlying structural cardiac abnormalities, such as congenital, ischemic and post-surgical heart disease. The greatest impact of EAM is probably its application to facilitate pulmonary vein isolation for treatment for atrial fibrillation

Nowadays, several different EAM systems utilizing various technologies are available to facilitate mapping and ablation. Each EAM system has its strengths and weaknesses, and the system chosen must depend upon what data is required for procedural success (activation mapping, substrate mapping, cardiac geometry), the anticipated arrhythmia, the compatibility of the system with associated tools (i.e. diagnostic and ablation catheters), and the operator's familiarity with the selected system.

2.6 Biophysical modeling of the heart

Emerging research fields have the potential to contribute in the evolution of the health care system, and in particular in cardiology [6]. Computational cardiology still lacks maturity, but that considerable improvement is accessible. Many different steps are required to go from the raw biological data to the patient-specific simulation for diagnosis and therapy planning. This is a very interdisciplinary work that involves clinicians and biologists to acquire and analyze biological samples, mathematicians and engineers to formalize, develop and implement the computational models, companies

that develop implantable devices and drugs, and electrophysiologist that plan and perform interventions, and validate the models. All the biological and clinical data has to be transformed into a representative mathematical model, that can be personalized with additional specific data in a patient basis.

Multiscale models for electrophysiology simulation

Over the last years, a large number of mathematical models have been developed to simulate the electrical (cardiac electrophysiology) and mechanical (tissue deformation) dynamics of cardiac cells and tissues. Although models are by definition simplifications of a real object or phenomenon, they can serve the important purpose of helping researchers in gaining knowledge about a given process or function, and avoid at the same time unnecessary animal experiments. This is particularly important in biological systems where millions of interactions take place at the micro scale within microseconds. The cardiac processes are highly non-linear and result from very complex interaction between subsystems. Models can yield excellent approximations of very complicated processes even though some of the details of the real system are neglected. For instance, when modeling electrical propagation in cardiac tissue the genetic details of an individual can be ignored if they do not influence the target of the study. Hodgkin and Huxley used their mathematical model of the nerve cell to test fundamental hypothesis not directly measurable by experiments [39]. That model was the precursor of a large number of cellular cardiac models, being the first one by Denis Noble [40].

In the cardiac modeling literature, it is important to be aware of the existence of two difference types of mathematical models, the so-called phenomenological models and the predictive (biophysical) models. Phenomenological models are often macroscopic representations of a given phenomenon that can reproduce experimental results but do not have a reference to the physical system. On the other hand, predictive models can provide new findings, allowing insights into underlying mechanisms, outside the set of experimental conditions used to fit the model. Those latter models rely on anatomical and biophysical definitions of the phenomena under study.

In the past decades, there have been built hundreds of predictive biophysical models of cardiac myocytes that can reproduce the bioelectrochemical phenomena occurring through cardiac cellular membranes [41]. They allow

to study the interplay between anatomical structures and functional behavior, which is particularly important in pathological conditions. Models of cardiac cells are able to facilitate insights into the mechanisms underlying cardiac electrical dynamics, since they incorporate formulations of transmembrane ionic currents along with the voltage, ionic concentrations, and ion channel kinetics responsible for the currents [4]. They can capture the time-dependent processes that underlie common electrical pathologies at cellular level [42, 5, 43]. Those models are based on experimental electrophysiology data acquired from *in vivo* and exvivo samples using techniques such as patch-clamp (invented by Erwin Neher and Bert Sakmann in the 1970's), which could be assimilated thanks to mathematical and numerical models of computational electrocardiology, such as the Poisson-Nernst-Planck (PNP) system. Hence, there are mathematical models to simulate ventricular myocytes, atrial myocytes, specialized conducting tissues such as Purkinje cells or fibroblast.

Most of the models have also been adapted to take into account the electrophysiological heterogeneity present in real tissues [44]. However, it is important to be aware that all those models only consider a number of components from the real physical system, and therefore it is essential to find out which are the most important questions that one aims to answer with the model in order to identify the key elements and parameters. For instance, one could use a biophysical model of the cell to study the effect of a drug that blocks a particular ionic channel, and hence the model selected will have to include a mathematical description of the specific channel and its relation with other part of the whole system [45, 46].

Since cellular models by themselves will not allow to perform whole heart studies, they have to be integrated into tissue and organ level models [47, 48]. The integrating approach is known as multiscale modelling, and has to deal with the coupling of different temporal and spatial scales into a single main model. Therefore, we have subsystems with different levels of detail coupled together by a few interface variables. In cardiac electrophysiology modelling, cell models are coupled together by means of the so-called bidomain model, a generalization of the one-dimensional cable theory, that takes into account the evolution of the intra-, and extracellular potential fields. The bidomain model is a reaction-diffusion set of equations that can incorporate the information from the cellular scale, but not in an individual fashion, since it is a continuous-based model that averages the properties of many cells up to the body surface [49]. The bidomain model only receives one parameter from the cellular level, the transmembrane potential, that

results from a large number of ionic exchanges that are only traced at cellular level. As the bidomain model is very expensive computationally, it is often simplified by assuming that the relationship between intra- and extracellular domains has equal conductivity anisotropy ratios, which allows to obtain a simplified representation called the monodomain model [50]. This model has been widely used for cardiac simulation because of its reduced computational cost.

The use of biophysical models of the heart has made already important contributions to the understanding of cardiac electrophysiology, such as unveiling underlying mechanisms of arrhythmia [46, 42, 6] or proposing novel tools for patient risk stratification [51]. The multiscale biophysical models of the heart allow to model cardiac electrophysiology from cell to body scale. When those models are combined with three-dimensional representations of the heart, it is possible to simulate heart function with a great level of detail, and to perform experiments that could be impossible in a real clinical setting [42, 45]. However, the utility of the models relies on its accuracy and fidelity to reproduce experimental or clinical results, and therefore they have to be tailored to fit available data.

Some challenges still need to be overcome and have prevented the translation of such models in clinical environments. Among them the most important are the computational cost associated to cardiac simulations, the lack of patient-specific information that could be used to feed a generic model to personalize it, the lack of a comprehensive suite of tools to model and simulate cardiac tissues, and the lack of a proper validation of the computational techniques that are to be translated into the clinic.

Modelling whole heart electrical activity can be very complicated and time consuming. Once the anatomical model is built, if one wants to simulate cardiac electrophysiology in a full heart model, both monodomain and specially bidomain models are very demanding in terms of memory and computation resources. An average human heart is approximately 130 mm $\times$ 90 mm $\times$ 70 mm, that is $8.19 \times 10^5 mm^3$, from which 50% corresponds to myocardial muscle. If the heart is discretized into a 3D model with a spacing of 100 μm, we obtain 4.23×10^8 computational points. For each computational point we have to solve a cellular model which could consist of 30 ordinary differential equations (ODE), which makes 1.27×10^{10} ODEs to be solved at each time instance. Assuming that each ODE involves 100 floating point operations per second (Flop), we would have 1.27×10^{12} flops per time instance. Using a time step of 1 ms would give rise to 1.27×10^{15} flops/s.

If we perform the simulation in a 2.4 GHz Intel Core 2 (1.7 Gflops), then to simulate one-minute real time, we require 4.48×10^7 s, that is 518.5 days [52]. Therefore, time requirements for a single simulation are far from what would be reasonable in a clinical workflow. Fortunately, the evolution of parallel computing and the advance in GPU computing are easing considerably the problem, and reducing the timing for a simulation from days to a few hours.

Personalization of models

An important challenge that is also hampering the integration of biophysical simulation tools into a clinical environment is the difficulty in personalizing the computational models (e.g. geometric personalization or patient-specific parameter estimation from physical measurements).

There are two fundamental sources of data to adjust the models, the so-called patient-specific data, and population-based data. Patient-specific data are acquired from each individual, and are limited to the clinical invivo techniques available in each medical centre. On the other hand population-based data comprise all the data collected from invivo and exvivo experiments in several species for years. These data are very useful since most of the information required for the models cannot be retrieved easily, however, its use is opposed to the patient-specific philosophy.

Model personalization is a key component to understand the underlying physiological phenomena of a given patient and thus to provide personalized simulations for better diagnosis, decision making, and treatment planning. The effective personalization of model parameters requires the integration of a large amount of data provided from disparate diagnostic tools, imaging modalities and physiological measurement systems acquired across a range of anatomical levels (e.g. cell, tissue, organ or systemic levels). Data for personalization can include, MR and CT to reconstruct the patient specific anatomy of the ventricles, EAM data to obtain the patient-specific activation sequence, de-MRI to reconstruct the patient specific scar region, or genetic information to include the proper mutations in cell models, among others. It is important to remark that data is not only important to personalize models, but also to validate them by verifying their correctness and scope of use.

The difficulty of implementing rapid, robust and efficient model personalization has resulted in models that are fit to a specific geometry and thus

cannot be qualitatively validated for other individuals. The time and the amount of manual input required for personalizing a model remains prohibitive for integration into a clinical workflow. In addition, the routine clinical workflows do not include the very specific protocols and techniques required to personalize properly the models due to several reasons: cost per patient, time required to perform and acquire all the data per patient, cutting-edge equipment availability, and willingness of clinical staff.

Even though there are already available tools and software environments that are helping in the development of complex computational pipelines for cardiac modeling and simulations, they are in general individual efforts of single research labs [53].

Among the most complex cardiac substructures that are fundamental for modeling of patient-specific cardiac electrophysiology are the organization of cardiomyocytes (fiber orientation), and the cardiac conduction system [6]. The arrangement of cardiomyocytes in the atria and ventricles follows a specific configuration that has been studied both in animal and human hearts [54, 55], and has permitted the definition of mathematical models that describe it [56]. In order to obtain the patient-specific fibre orientation of the ventricular tissue, non-trivial techniques such as diffusion tensor MRI have to be employed [57]. However, due to the long acquisition times required and the fact that the heart is beating, only a few heart planes can be imaged invivo, and the rest have to be interpolated, which hampers the original goal.

This thesis focuses on the development of methods to estimate the PKN for a given patient, to improve the personalization of the activation sequence.

Modeling the PKN

The structure of the PKN and the location of the PMJs cannot be directly segmented from any in-vivo imaging technique. This fact has led researchers to the construction of generic population-based computational models of the CCS in the ventricles [58, 7]. Among the most popular techniques to build a synthetic PKN, there is the use of fractals [59], or L-Systems [60, 7], which in some cases are enhanced with rules and permit the generation of loops to create networks instead of trees. Other researcher have opted for manually delineating the PKN on the endocardium of a segmented 3D model [61, 62]. Ex-vivo images have also been used to build reference models in humans [63, 11], and different animals such as rat, rabbit or dog where

the most prominent structures can be observed [64, 65, 66], overlooking the complex morphology of the network. In some cases, modellers have opted for paying little attention to it, and instead have indirectly considered its function by altering the model's endocardial properties, e.g. increasing the tissue endocardial conduction velocities. The reader is referred to [7] for a review on different techniques commonly used to build computer models of the CCS.

Since it has been described the interaction of the PKN with disease [58, 67], therapies [61, 68] and drugs [45], some modelers are trying to obtain personalized PKNs. Therefore, recent studies have started to use patient-specific data obtained from EAMs of the ventricles to estimate a patient PKN [69, 70]. In an EAM procedure, the local activation time (LAT) at different tissue locations can be measured using catheters on the inner surface of the ventricles. EAMs are one of the few *in vivo* clinical sources of information that can be directly used to obtain the electrical function of the heart. The LAT maps obtained from EAMs can be used to estimate the location of PMJs, and therefore, to somewhat personalize the PKN in a ventricular model [71, 72, 73]. In addition, in some studies such as [70], the PKN was further personalized not only to match the normal activation from PKN to the myocardium, but also for cases in which the PKN is activated retrogradely from an abnormal ectopic focus out of the AVN.

In the works by [69] and [72], a mathematical method to optimize positions of randomly placed PMJs is presented that reduces simulated activation errors given a pre-computed generic Purkinje tree structure. In [71], the location of PMJs is determined from singularity points on highly dense activation maps obtained from simulations.

Application to therapy planning

Despite all the drawbacks, biophysical models are also starting to be embraced in clinical research environments to assess their predictive capacity for treatment delivery and optimization [74, 5, 75]. The applications are countless, and although they will require a long validation process and acceptance from the clinical community, the initial results are promising. For instance, related to the PKN, they have been used to study the relation of Purkinje-muscle reentry as a mechanism of polymorphic ventricular arrhythmias [28], sawtooth effects on the Purkinje system [62], the interaction of

the PKN and CRT pacemaker configuration [76], or the Purkinje-mediated effects in the response of quiescent ventricles to defibrillation shocks [77].

Some of the therapies that could potentially benefit from biophysical models are cardiac resynchronization [78] or radio-frequency ablation [79], among others. Both are electrical therapies with a medium-low rate of success (up to 35% patients do not respond to the therapy) in which a large number of input parameters needs to be considered to deliver the therapy optimally, and increase the response in the patients. However, the basic principle of the therapy remains unchanged, pacing and ablation approaches being largely non-dependent on individual patient's characteristics.

Detailed biophysical models have been reported to mimic the therapy outcomes in reduced groups of patients, but are validated against measurements obtained from experimental laboratories providing animal and human data in well controlled conditions. Basically they could predict in a procedure of radiofrequency ablation where the optimal ablation points are to stop a scar-derived ventricular tachycardia before the intervention. Therefore, those studies are paving the road for more complex and realistic clinical settings in which the biophysical models can be useful. However, it is important to remark that all those models results are to some extent approximations of reality where assumptions and approximations have been taken, and therefore outcomes have to be carefully interpreted.

3

Inverse Estimation of Sources of Electrical Activation on a two-dimensional tissue Sheet

Abstract – Modeling the cardiac conduction system is a challenging problem in the context of computational cardiac electrophysiology. Its ventricular section, the Purkinje system, is responsible for triggering tissue electrical activation at discrete terminal locations, which subsequently spreads throughout the ventricles. In this chapter, we present an algorithm that is capable of estimating the location of the Purkinje system triggering points from a set of random measurements on a synthetic tissue sheet. We present the properties and the performance of the algorithm under controlled synthetic scenarios. Results show that the method is capable of locating most of the triggering points in scenarios with a fair ratio between terminals and measurements. When the ratio is low, the method can locate the terminals with major impact in the overall activation map. Mean absolute errors obtained indicate that solutions provided by the algorithm are useful to accurately simulate a complete patient ventricular activation map.

This chapter is adapted from: Barber F., Lozano M., Garcia-Fernandez. I., Sebastian R. Inverse Estimation of Terminal Connections in the Cardiac Conduction System. Mathematical Methods in Applied Sciences, Vol. 41(6):, pp. 2340 - 2349, 2018.

3.1 Introduction

Computational modeling of the heart aims at helping to understand the complex structure and function of the heart in health and disease. The construction of realistic computational cardiac models that can be personalized to a patient is challenging and requires the fusion of disparate medical and biological data [6, 80]. On the one hand, clinical images from computed tomography (CT) or magnetic resonance imaging (MRI) can be acquired and segmented to build patient-specific 3D heart geometries. Those segmented hearts would be meshed to create a fine computational domain in which finite element methods can be applied. On the other hand, to model heart function ex-vivo measurements from cell and tissue samples are needed to feed models, which are commonly represented by sets of differential equations that describe its coupled nonlinear behavior. However, the heart is highly complex and inhomogeneous, and not all the cardiac structures and tissue properties can be personalized due to imaging resolution limits.

Among these structures, there is the cardiac conduction system (CCS) or PKN (in the ventricles), which is responsible for the synchronized activation of the cardiac muscle that triggers the heart contraction.

In recent works by [71, 69, 72], summarized in Chapter 2, some techniques have already been developed to infer the location of PMJs and structure of a Purkinje tree from EAMs acquired in-vivo. None of those techniques try to estimate the real location of PMJs, but a distribution of them that is coherent with tissue global activation sequences. Estimating the real location of heart electrical triggers, i.e. PMJs or ectopic foci in pathological tissue, is highly relevant for both constructing realistic models of the heart and providing substrate data to planning interventions. For instance the CCS is known to interact retrogradely with the electrical impulse triggered by pacing leads of cardiac resynchronization therapy devices [61, 81]. In addition, it is still unknown how ablation lines carried out in ventricular tissue to interrupt ventricular tachycardia can affect CCS and in particular PMJs, and therefore a better knowledge in their localization might help in planning interventions.

Our goal is to perform an inverse estimation of the location and activation time of PMJs on the inner surface of the heart, given a set of randomly distributed measurements, similar to those obtained in EAMs.

Before addressing the problem on a 3D structure representing a patient's heart, in this chapter, we present an estimation method, and evaluate it

on several synthetic 2D scenarios. To represent the complex PKN patterns described in the literature [82], we build synthetic tree structures recursively. Basically, we create two perpendicular child branches at the end of each branch with decreasing length and locating the PMJs at the leaf nodes of the tree. We build several scenarios by constructing Purkinje trees with an increasing number of branches and PMJ density, to assess the potential of the algorithm to estimate PMJs. The estimation of the underlying Purkinje system branching structure is not addressed in this chapter.

3.2 PMJ estimation method

To develop and test the methodology we take the following assumptions: the cardiac tissue is represented by a 2D, Euclidean domain, $\Omega \subset \mathbb{R}^2$; the signal propagation is considered isotropic, and the propagation velocity is constant. According to the previous description of a Purkinje tree, we assume that the signal enters cardiac tissue through a set $\mathcal{S}$ of n PMJs, with locations $\mathbf{s}_k \in \Omega, k = 1, \ldots, n$. The activation time of PMJ k will be denoted as $\tau_k \in \mathbb{R}$.

Given a point $\mathbf{p} \in \Omega$, its local activation time (from now on LAT) will be the earliest arrival time of the signal from the source nodes, i.e. PMJs, and is given by

$$t(\mathbf{p}) = \min_k \left(\tau_k + \frac{\|\mathbf{p} - \mathbf{s}_k\|}{v} \right), \tag{3.1}$$

where v is the propagation velocity of the signal through the cardiac tissue. Figure 3.1 (a) shows a simple scenario with two PMJs represented with solid circles, and several points with measurements (LATs) represented with crosses. Three of the measurement points displayed with LATs t_{i1}, t_{i2} and t_{i3}, were activated by the same PMJ (indicated with arrows).

Since the Purkinje tree cannot be observed, PMJs will be considered as unknown, both in their number and location. Our goal is to estimate the location of the set of *effective* PMJs that produces the observed measurements, which are the activation times at m given locations. Thus, we state our problem as

Problem 3.2.1 (PMJ estimation)**.** *Given a set $\mathcal{P}$ of tuples $(\mathbf{p}_l, t_l) \in \Omega \times \mathbb{R}, l = 1, \ldots, m$, where t_l is the known activation time at $\mathbf{p}_l$, find a set $\hat{\mathcal{S}}$ of estimated PMJs and associated activation times $(\hat{\mathbf{s}}_i, \hat{\tau}_i)$, $i = 1, \ldots, r$, that*

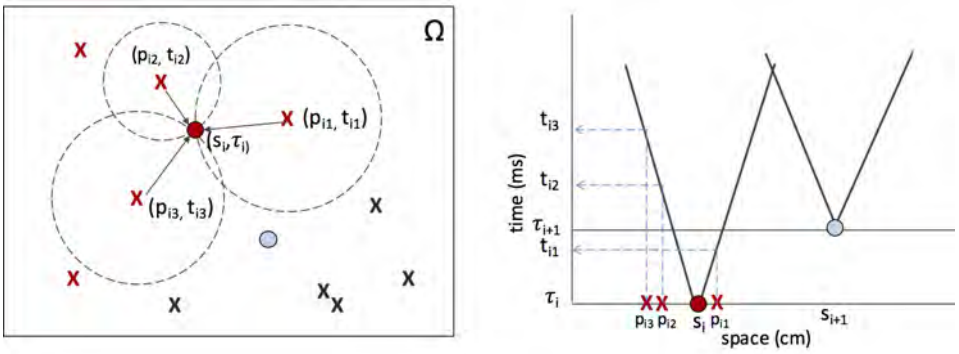

Figure 3.1: The relationship between PMJs and measurement points. Spatial representation in a 2D plane with spatial location of PMJs and measurement points (left) and a space-time representation (right). If a location is activated by a certain PMJ, $\mathbf{s}_i$, then its space-time coordinates $(\mathbf{p}_i, t_i)$ belong to a cone with vertex in the PMJ and with slope defined by the propagation velocity.

minimizes the error function

$$E = \frac{1}{m}\sum_{l=1}^{m}(t_l - \hat{t}_l)^2 \tag{3.2}$$

where $\hat{t}_l$ *is the estimated activation time defined by (3.1), for* $\mathbf{p} = \mathbf{p}_l$ *and the* min *function ranging in* $(\hat{\mathbf{s}}_i, \hat{\tau}_i),\ i = 1, \ldots, r.$

This problem admits a trivial solution consisting on taking $\mathcal{F} = \mathcal{P}$. If we apply a general unconstrained optimization method using (3.2) as cost function we shall find that many of the estimated points are located at positions belonging to $\mathcal{P}$. Moreover, the existence of this alternative solution shows that the problem is not convex, since it has several local minima. Thus we need a method to build $\mathcal{F}$ that avoids this unwanted trivial solution.

Let us consider a PMJ with spatial coordinates $\mathbf{s} \in \Omega$ and activation time τ. And let us consider a point $\mathbf{p}$ that is activated by the propagation of the signal from $\mathbf{s}$. The activation time t of point $\mathbf{p}$ must meet the equation

$$\|\mathbf{p} - \mathbf{s}\| = v(t - \tau). \tag{3.3}$$

Equation (3.3) defines the positive half of a cone (see Figure 3.1, right, for a two dimensional representation of this idea) with its vertex in $(\mathbf{s}, \tau)$; thus, for any point activated by $\mathbf{s}$, the point $(\mathbf{p}, t) \in \mathbb{R}^3$ belongs to that cone.

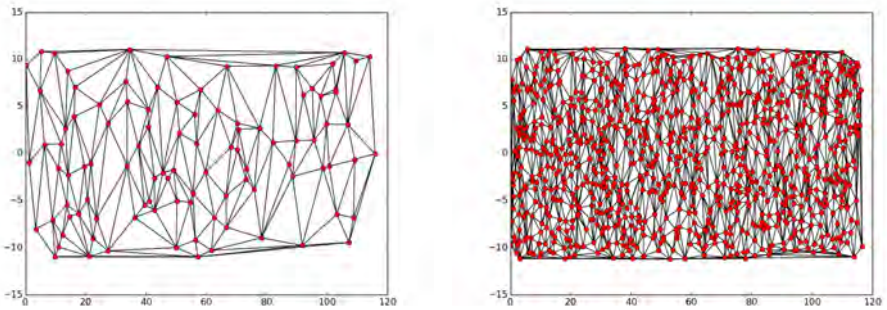

Figure 3.2: Two different measurement point sets, $\mathcal{P}$, and their corresponding Delaunay triangulations. (Left: $|\mathcal{P}| = 100$, right: $|\mathcal{P}| = 1000$).

Given three points activated by the same PMJ, if a cone can be found in $\mathbb{R}^3$ containing their coordinates in the form $(\mathbf{p}_l, t_l)$, then PMJ coordinates $(\mathbf{s}, \tau)$ must be located at the cone's vertex. Moreover, since the activation of the point $\mathbf{p}$ is the result of a signal propagation, then its activation time t will always be greater than the activation of the PMJ that caused it, $\tau \leq t$ (it would be equal only if $\mathbf{p} = \mathbf{s}$).

To construct a set of candidate PMJs, we are going to use these properties. As a first step in our method we build a Delaunay triangulation D for the set of measured points, considering their spatial coordinates. Such a triangulation is the construction of an irregular mesh that takes the points as vertexes and in which all the faces are triangles [83]. Figure 3.2 shows the Delaunay triangulations for the smallest and largest sizes of $\mathcal{P}$, considered in our experiments.

Let T be the set of indices that define the Delaunay triangulation

$$T = \{\{k_1, k_2, k_3\} : \text{ The triangle } \mathbf{p}_{k_1}, \mathbf{p}_{k_2}, \mathbf{p}_{k_3} \text{ belongs to } D\}.$$

Given a triangle $i = \{i_1, i_2, i_3\} \in \mathcal{T}$, formed by the measurement points, $\mathbf{p}_{i_1}$, $\mathbf{p}_{i_2}$ and $\mathbf{p}_{i_3}$, with activation times, t_{i_1}, t_{i_2} and t_{i_3}, we look for a solution $\mathbf{f}_i = (\hat{\mathbf{s}}_i, \hat{\tau}_i) \in \mathbb{R}^3$ of the system of nonlinear equations

$$\begin{aligned} \|\mathbf{p}_{i_1} - \hat{\mathbf{s}}_i\| - v(t_{i_1} - \hat{\tau}_i) &= 0, \\ \|\mathbf{p}_{i_2} - \hat{\mathbf{s}}_i\| - v(t_{i_2} - \hat{\tau}_i) &= 0, \\ \|\mathbf{p}_{i_3} - \hat{\mathbf{s}}_i\| - v(t_{i_3} - \hat{\tau}_i) &= 0. \end{aligned} \tag{3.4}$$

Moreover, since a valid PMJ will have an activation time earlier than the LAT of the three measurements points that are used to find it, namely

$$\tau_i \leq t_{i_j}, \quad j = 1, 2, 3, \tag{3.5}$$

the solution we find must also meet this constraint.

3.2.1 Algorithm description

To extract a set $\hat{\mathcal{S}}$ containing valid PMJs belonging to the hidden tree, we have designed Algorithm 1. For each triangle $i \in T$ included in the Delaunay triangulation D we look for a valid tentative PMJ, $\mathbf{f}_i$. This step, corresponding to line 5 in the algorithm, consists of the solution of the system (3.4). By means of a change in the reference system, and a transformation to polar coordinates, this system can be solved analytically.

Algorithm 1 PMJs estimation

1: **Input** $\rightarrow \mathcal{P}$ {Set of measurement points with activation time}
2: $\hat{\mathcal{S}} \leftarrow \emptyset$ {PMJs}
3: $T \leftarrow delaunay(\mathcal{P})$ {Build a Delaunay triangle mesh}
4: **for all** $tri \in T$ **do**
5: $\quad \mathbf{f}_i \leftarrow find\_source(tri)$ {The solver finds out a local solution from the triangle tri }
6: $\quad$ **if** $is\_valid(\mathbf{f}_i)$ **then**
7: $\quad\quad \hat{\mathcal{S}} \leftarrow \hat{\mathcal{S}} \cup \mathbf{f}_i$
8: $\quad$ **end if**
9: **end for**
10: **Output** $\leftarrow \hat{\mathcal{S}}$ {Set of estimated PMJs }

The previous step can lead to a false PMJ. This will happen when three points that form a triangle in the Delaunay triangulation were not activated by the same real PMJ. Under this situation, a candidate point $\mathbf{f}_i$ assumes that the three points were activated from a single source, while they were actually activated by two or three sources. To reduce the number of spurious PMJs, $\mathbf{f}_i$ needs to be validated. The validation function, called in line 6 of the algorithm, checks four conditions and only accepts the candidate PMJ if all of them are met.

The first condition checked is the verification that the candidate PMJ is consistent with the three measurement points that have generated it, by

means of the inequalities (3.5). The second condition checked is whether the estimated PMJ is inside the Delaunay triangulation T. Otherwise, it is considered to be outside the domain of the problem and is disregarded. The third condition requires that the estimated PMJ is compatible with the backward eikonal problem associated to the triangle where the estimated PMJ is located in. This criterion has already been used by other authors [72] and states that a measurement point cannot activate later than the traveling wavefront produced by the closest PMJ. That is, the activation time of the estimated PMJ must be consistent with the nearby observed activation times. Thus, we request that the vertexes of triangle k containing $\mathbf{f}_i = (\hat{\mathbf{s}}_i, \hat{\tau}_i)$ meet the condition

$$t_{k_j} \leq \frac{\|\hat{\mathbf{s}}_i - \mathbf{p}_{k_j}\|}{v} + \hat{\tau}_i + \epsilon, \quad j = 1, \ldots, 3 \tag{3.6}$$

where ϵ is a tolerance parameter that accounts for possible numerical errors.

The last condition requires to find a new measurement point satisfying equation (3.4). Therefore, the total number of measurement points that must be compatible with a candidate PMJ to validate it is 4: 3 points from the triangle in T that generated the candidate PMJ plus an additional one.

3.2.2 Discussion of the method

The proposed method takes as an input the set $\mathcal{P}$ of measurement points in Ω with their associated activation times, $(\mathbf{p}_k, t_k)$. The detection of a given PMJ, $\mathbf{s}_i \in \mathcal{S}$, depends on the fact that at least one triangle of T is contained in the region

$$V(\mathbf{s}_i) = \{\mathbf{x} \in \Omega : \|\mathbf{s}_i - \mathbf{x}\| + v\tau_i \leq \|\mathbf{s}_k - \mathbf{x}\| + v\tau_k,\ \forall(\mathbf{s}_k, \tau_k) \in \mathcal{S}\}, \tag{3.7}$$

which is the additively weighted Voronoi region associated to $\mathbf{s}_i$ [83]. For the sake of brevity we shall denote it by V_i. In the absence of further assumptions about the data acquisition procedure, we will consider that the spatial locations of measurement points are a random sample of a uniform distribution on Ω. As a consequence, the probability that a point lies on a given region is proportional to its area. The question that arises is whether the probability of not detecting a given PMJ can be made arbitrarily small by increasing the number of measurement points.

Let $\mathbf{s}_i$ be a PMJ with activation time τ_i. The area of V_i depends on the relative position and activation time of $\mathbf{s}_i$ respect to the other PMJs. If there

exists some $\mathbf{s}_j$ with $\tau_j < \tau_i$ such that $\|\mathbf{s}_i - \mathbf{s}_j\| < \tau_i - \tau_j$, then the signal from $\mathbf{s}_j$ will arrive in $\mathbf{s}_i$ before it activates. As a consequence, $V(\mathbf{s}_i) = \emptyset$ and no tissue will be activated from $\mathbf{s}_i$, making it undetectable. A similar condition appears when there exists some PMJ $\mathbf{s}_j$, with $\tau_j < \tau_i$, such that $\|\mathbf{s}_i - \mathbf{s}_j\| = \tau_i - \tau_j$. In this case, the region activated by $\mathbf{s}_i$ is a line segment that starts at $\mathbf{s}_i$ and it spans in the opposite direction from $\mathbf{s}_j$. Since the Voronoi region of $\mathbf{s}_i$ has, in this case, null measure, it is undetectable by our method. Anyway, this PMJ is indistinguishable from $\mathbf{s}_j$ and, it has no effect on tissue activation (if we remove it, the activation time at any location does not change due to $\mathbf{s}_j$).

These layouts are not relevant to our goal, since the activation map is not affected at all by PMJs that fulfill any of these conditions. They are not effective, in the sense that they do not change the activation time at any location of the heart tissue. In what remains, we will call *effective* PMJ to any signal source point that is not in any of the two cases described above. That is, a PMJ with location $\mathbf{s}_i$ and activation time τ_i is said to be *effective* if there is no other PMJ, $\mathbf{s}_j$ with $\tau_j < \tau_i$, such that $\|\mathbf{s}_i - \mathbf{s}_j\| \leq \tau_i - \tau_j$. In this chapter, we focus only on the estimation of effective PMJs.

Let $\mathbf{s}_i$ be an effective PMJ. For $\mathbf{s}_i$ not to be detected, it is necessary that there is no triangle of the Voronoi triangulation $\mathcal{V}$ with its three vertexes in V_i. This would happen either if there is less than three measurement points in v_i or if, having three or more points in V_i, they would not form a triangle in $\mathcal{V}$.

Let us first consider the probability that no three points fall in V_i. Let A_i be the area of V_i and A the area of the whole problem domain Ω, the probability that a single point is in V_i will be $p_i = A_i/A$. If a set $\mathcal{P} \subset \Omega$ with $m \geq 3$ random points is generated, we can consider the random variable $X_i = |\{(\mathbf{p}, t) \in \mathcal{P} : \mathbf{p} \in V_i\}|$, where $|\cdot|$ denotes cardinal, which follows a Binomial distribution $X_i \sim B(m, p_i)$. The probability that less than 3 points are in V_i is, then,

$$P(X_i \leq 2) = (1 - p_i)^m + p_i(1 - p_i)^{m-1} + p_i^2(1 - p_i)^{m-2}, \tag{3.8}$$

which tends to 0 as $m \to \infty$.

Next, we focus in the case when we have three or more points inside V_i and they do not form a triangle in $\mathcal{V}$. An example of a set of measurement points that leads to this situation with three points is shown in Figure 3.3. Let $\mathbf{p}_1^i, \mathbf{p}_2^i, \ldots, \mathbf{p}_k^i$ be a set of $k \geq 3$ measurement points which are inside

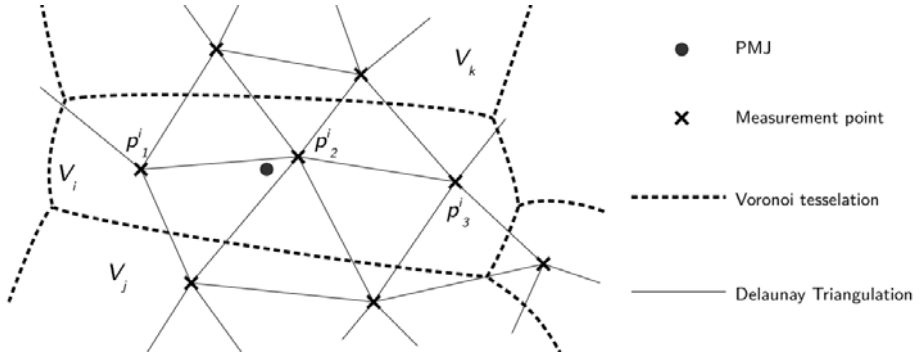

Figure 3.3: A situation with a Voronoi region, V_i, containing three measurement points, $\mathbf{p}_1^i$, $\mathbf{p}_2^i$ and $\mathbf{p}_3^i$, which do not form a triangle of the Delaunay triangulation.

V_i but do not generate any triangle in $\mathcal{V}$, and let H be the area of the convex hull formed by them. If any new measurement point is added which is contained in H, then the new set of points in V_i will form two or more new triangles in $\mathcal{V}$ [83]. Since H is nonzero with probability 1, following the previous reasoning, we can see that the probability of this not happening tends to 0 as m grows.

From previous analysis, it is derived that the probability of not detecting a given PMJ tends to zero if we are capable of increasing the number of measurement points. An additional property that arises from this discussion is that, the bigger the area a given PMJ activates, the higher the probability of being detected by the algorithm. Since in many clinical situations the interest is in knowing the origin of the activation of a given tissue region, this indicates that our method will detect the most relevant PMJs first with higher probability.

Another possible source of error in the algorithm is the estimation of a PMJ that actually is not in $\mathcal{S}$. This can happen if we estimate a PMJ from a triangle with vertexes belonging to different Voronoi regions. However, as discussed in Section 3.2.1, before a tentative PMJ is accepted several validations tests are performed, which reduce the number of spurious estimations.

3.3 Performance Evaluation

To evaluate our approach, we have generated several scenarios consisting of a simulated Purkinje tree structure along with a set of measurement

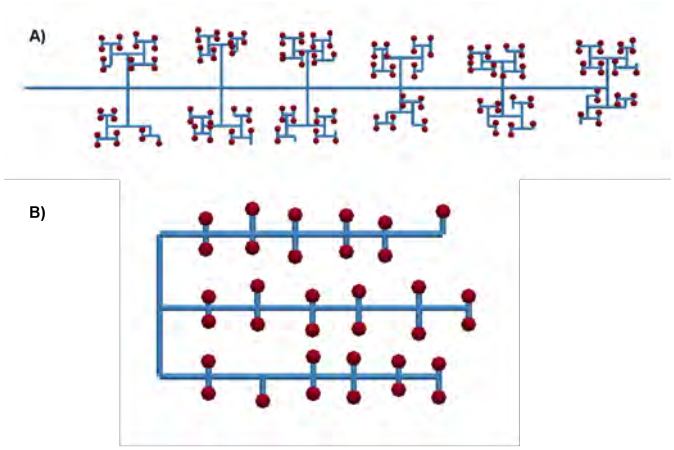

Figure 3.4: Example of generated trees. A) 1 main branch with depth 6 (B1D6), B) 3 main branches with depth 2 (B3D2)

points uniformly distributed. In this section we describe the experimental methodology used and discuss the results. We provide several performance measurements for our method, together with a comparison with the methodology proposed by Cardenes et al. [71].

3.3.1 Methodology

The test trees representing the cardiac conduction system are built procedurally. We use a recursive algorithm that, at every level, creates two new branches at the end of each branch that was built in the previous level. Every new branch is perpendicular to the parent branch. The leaf nodes of the tree are the PMJs, which represent sources of electrical signal in the myocardium. The density of PMJs is indirectly controlled by the depth of the branch recursion. Branch lengths are generated following a normal distribution with parameters obtained from [7]. Figure 3.4 shows two examples of trees used in our experiments.

We generate two types of scenarios: i) trees with a single main branch, and ii) trees with three main branches connected as depicted in Figure 3.4. For each scenario type, we consider 3 different recursion depths for generating tree subbranches: depth 2, depth 4 and depth 6. We will label every configuration with letter B followed by the number of branches plus letter D followed by the depth used to generate it. E.g., a tree with 3

branches and depth 4 will be named B3D4. Figure 3.4 (A) shows a tree with one branch and recursion depth of 6 (B1D6). Figure 3.4 (B) shows a tree with three branches and a recursion depth of 2 (B3D2).

Given a simulated Purkinje tree, we firstly place a set of measurement points in the domain, uniformly distributed, with a number of points varying from 100 to 1000 in steps of 100. Secondly, the LAT at each measurement point is computed, by propagating the electrical signal along the tree. This propagation is done first from the tree root up to the PMJs and then from the PMJs to each sensor through the shortest path, using Equation (3.1). The signal propagates within the tree around three times faster than on the myocardial tissue domain. The experimental process can be summarized as follows: i) Generate an artificial tree with a set of PMJs as source points, $\mathcal{S}$; ii) Generate a set $\mathcal{P}$ of measurement points uniformly distributed; iii) Propagate the signal from $\mathcal{S}$ to $\mathcal{P}$ and set the corresponding activation times for every point in $\mathcal{P}$; iv) Run the algorithm proposed in Section 3.2.1 and obtain an estimation $\hat{\mathcal{S}}$; v) Compare the solution $\mathcal{S}$ with the estimation $\hat{\mathcal{S}}$ and evaluate its quality.

In Figure 3.5, the results of the algorithm can be observed for two dense scenarios (B3D4 and B3D6), with two different measurement points densities. In the figure, measurement points are represented by crosses. The blue dots represent the PMJs that have been found, while the red dots represent PMJs that have not been found in the solution by our algorithm. The set of all measurement points which are activated by a common PMJs is represented by a polygon enclosing them.

To evaluate these results we consider two approaches. First, we compare the generated PMJs $\mathcal{S}$ (considered as the true unknown cardiac conduction system) and the estimation $\hat{\mathcal{S}}$ provided by our algorithm. This will give us information about the ability of the algorithm to find the actual PMJs in the simulated scenarios. This quality measurement is only available because we have the actual (generated) PMJs of the CCS. When the method is applied to clinical data, real PMJs will not be available for comparison. Then, as a second error measure we compare the activation map generated by $\hat{\mathcal{S}}$ to the activation times measured in the locations of $\mathcal{P}$. Following previous works [69, 72], we use the maximum absolute error and the mean absolute error.

To be able to understand the quality of the results, it is important to define what is an acceptable error in our problem. The physiological signal propagation process that motivates this work starts when the electrical signal

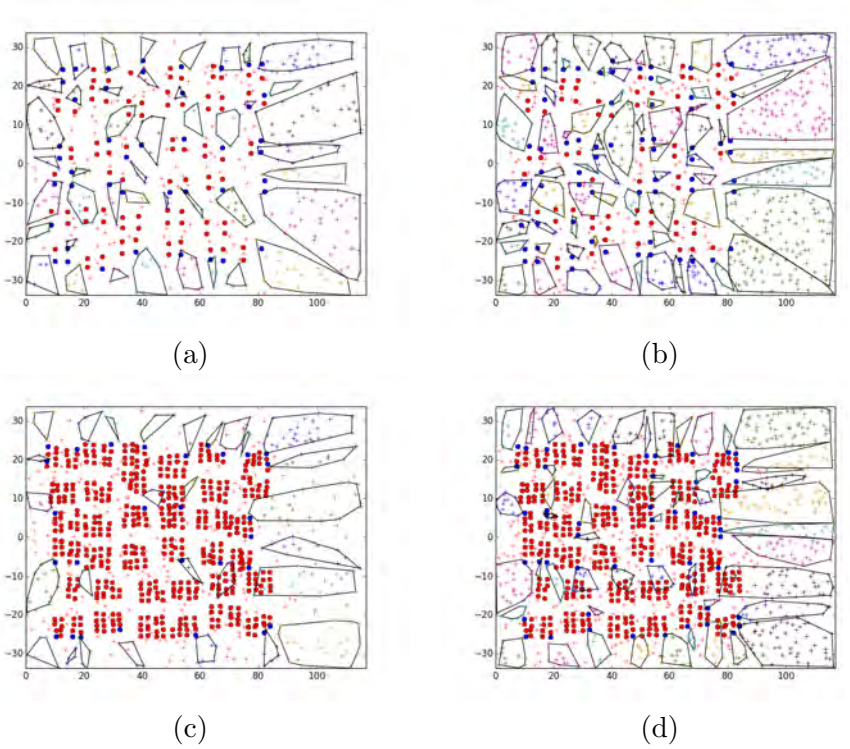

Figure 3.5: Solutions provided for scenario B3D4 (top) and B3D6 (bottom) with (a,c) 500 measurement points and (b,d) 1000 measurement points.

enters the CCS and ends when the whole cardiac tissue has been activated. In our synthetic cardiac tissue, this process cannot last more than $134ms$, which corresponds to the diameter of the domain divided by the propagation velocity of the signal in the tissue. It is also important to know that in the literature an error below $5ms$ is considered a highly accurate LAT [84, 85].

3.4 Results and discussion

The results of the simulation study, including all the scenarios, are summarized in Figure 3.6. The number of sources, i.e. PMJs, estimated for the scenario with a single main branch is displayed in Figure 3.6 (a,c,e), while Figure 3.6 (b,d,f) shows the PMJs estimated using three main branches. Every row represents a different recursion depth, for depths 2, 4 and 6. Each plot shows the number of PMJs in the scenario (F_REAL), the num-

ber of PMJs that can be truly estimated (F_DET) or effective sources, the total number of PMJs estimated by the algorithm (F_EST) and finally, the number of PMJs correctly estimated (F_OK).

In Figure 3.6, there is a small difference between the values of the estimated (F_EST) and correctly estimated (F_OK) number of PMJs which indicates that some false positives are obtained (estimated PMJs in $\hat{\mathcal{S}}$ that were not in $\mathcal{S}$). In configurations where measurement points are not activated by the same PMJ, but produce a feasible candidate we obtained false positives. Although several validation tests are performed during the algorithm, as discussed in Section 3.2, the results show that the validation function does not detect all of them. In scenarios B1D2, B1D4 and B3D2 the algorithm obtains nearly all PMJs when it has enough measurement points. However, when the density of PMJs increases the problem becomes more complex, since these points tend to be clustered, as Figure 3.5 shows.

Figure 3.7 (a) shows the number of PMJs estimated versus the number of real PMJs for a fixed number of 1000 measurement points. Notice that each point in the plot corresponds to one scenario (B1D2, B3D2, B1D4, B3D4, B1D6 and B3D6) with it corresponding number of PMJs. In the first four scenarios, the number of estimated PMJs increases with the total number of PMJs. However, this does not occur in the last two scenarios (B1D6, B3D6) where the number of found PMJs decreases. This behaviour is also amplified because we have set a fixed number of measurement points. As a consequence, the ratio between measurement points and PMJs decreases, making it more difficult to build a complete estimate.

Despite these apparent limitations, Figure 3.7 (b) shows how the mean of the absolute error associated to each scenario decreases rapidly with the measurement points and from 500 measurement points and on, it stays below $2ms$ for all scenarios. This behavior of the error reveals that the correctly estimated PMJs are the most significant ones. As can be seen in Figure 3.5, the PMJs which are properly detected are close to the border of the region occupied by the tree, while the inner PMJs are those missed by the algorithm. The signal emitted by these inner points is quickly masked by the points at the border of the tree and they are mainly non-effective PMJs. From these results, we conclude that our algorithm is capable of finding most of the effective nodes of the Purkinje system.

To compare our method with previous approaches, we have implemented the method described in [71] based on the gradient of the activation time considered as a differentiable function of the location. In Figure 3.8 we present

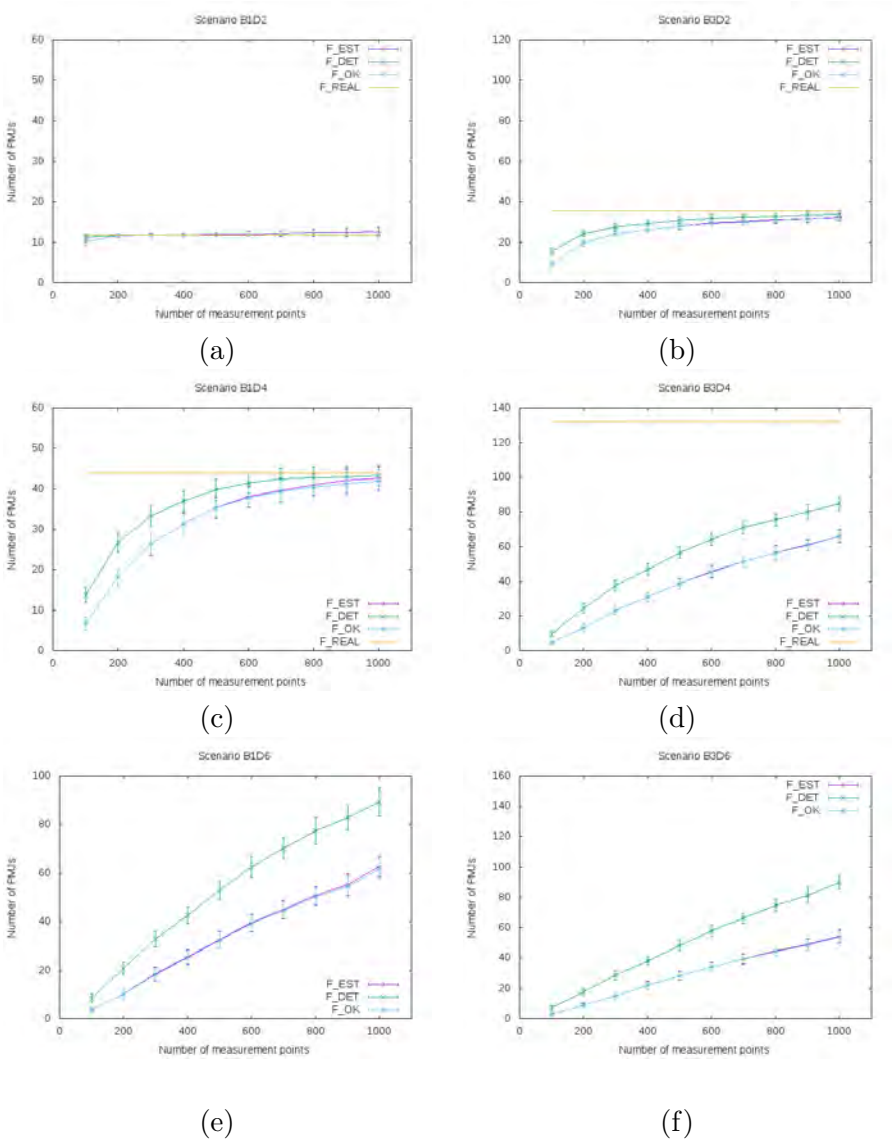

Figure 3.6: Results for (a,c,e) a single main branch, and (b,d,f) for three main branches. Every row corresponds to a different recursion depth. The used recursion depths are (from top to bottom) 2, 4 and 6. The results are averaged for the different instances of each scenario, and plotted with its standard deviation. Figures are not at the same scale, since the number of PMJs varies for the different scenarios. See the text for details on the figure contents.

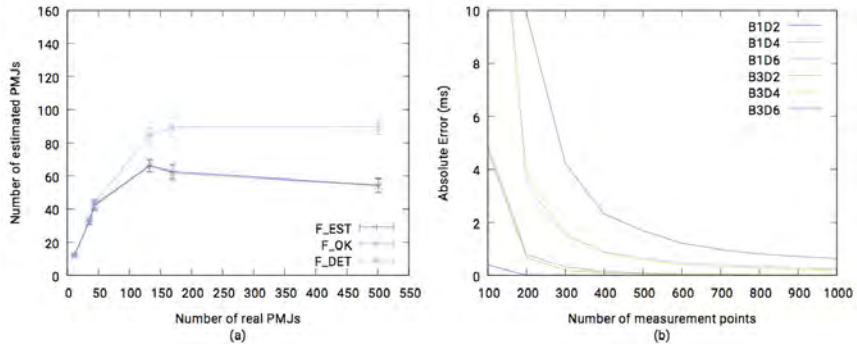

Figure 3.7: (a) Number of PMJs detected with respect to the total number of PMJs with 1000 measurement points. (b) The mean of the absolute error (in milliseconds) for the different scenarios considered.

the two extreme scenarios, B1D2 and B3D6, solved with this method, in Figure 3.9 (a) we show the total number of estimated PMJs and the number of correctly estimated PMJs and in Figure 3.9 (b) we can see the mean of the absolute error for the different scenarios. It is remarkable that in the simplest scenario, B1D2, the method performs poorly, many PMJs are detected but only few are correct, producing a high absolute error. Nevertheless, with the most complex scenario, B3D6, the number of correctly estimated PMJs is similar to that obtained with our method.

In summary, our method has shown a higher accuracy at estimating PMJs and it performs well with low and high densities of PMJs. On the other hand, the gradient method has obtained lower errors for scenarios with high densities of PMJs and low density of measurement points.

3.5 Conclusions

We have developed a method to estimate the sources of electrical activation from a set of random sampled acquired from a 2D tissue sheet. The method is capable of locating most of the triggering points in scenarios with a fair ratio between terminals and measurements. When the ratio is low, the method can locate the terminals with major impact in the overall activation map. Mean absolute errors obtained indicate that solutions provided by the algorithm are useful to accurately simulate a complete patient ventricular activation map.

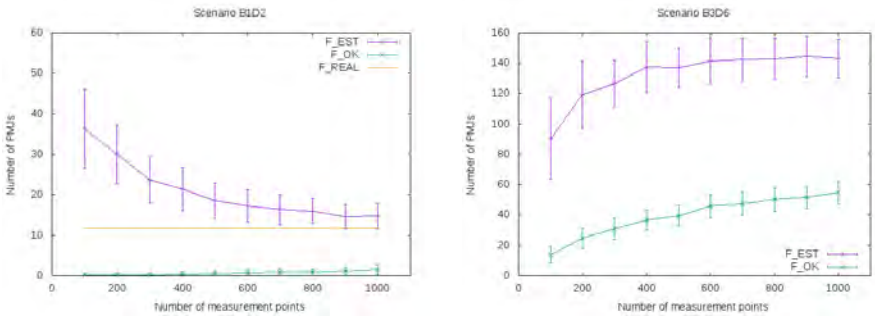

(a) (b)

Figure 3.8: Estimation results for scenarios B1D2 (a) and B3D6 (b) using the gradient method.

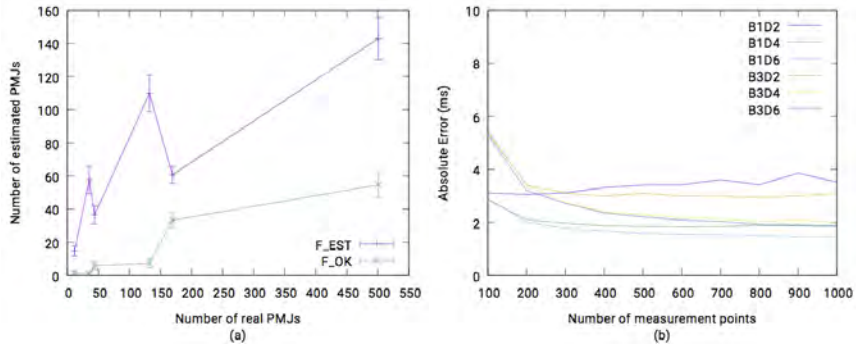

Figure 3.9: Results for the gradient method: (a) Number of PMJs detected with respect to the total number of PMJs with 1000 measurement points. (b) The mean of the absolute error (in milliseconds) for the different scenarios considered.

4

Estimation of Purkinje-Myocardial Junction hot-spots from Noisy Endocardial Samples

Abstract – The reconstruction of the ventricular cardiac conduction system (CCS) from patient-specific data is a challenging problem. High-resolution imaging techniques have allowed only the segmentation of proximal sections of the CCS from images acquired ex-vivo. In this chapter, we present an algorithm to estimate the location of a set of PMJs from synthetic simulated EAMs, as those acquired during radio-frequency ablation procedures. The method requires a mesh representing the myocardium with local activation time measurements on a subset of nodes. We calculate the backwards propagation of the electrical signal from the measurement points to all the points in the mesh to define a set of candidate PMJs, that is iteratively refined. The algorithm has been tested on several PKN configurations, with simulated activation maps, subject to different levels of Gaussian noise. The results show that the method is able to estimate a set of PMJs that explains the observed activation map for different synthetic PKN configurations. In the tests, the average error in the predicted activation time is below the amplitude of the Gaussian noise applied to the data.

This chapter is adapted from: Barber F., Lozano M., Garcia-Fernandez I., Sebastian R. Automatic Estimation of Purkinje-Myocardial Junction hot-spots from Noisy Endocardial Samples: A simulation study. International Journal for Numerical Methods in Biomedical Engineering, Vol. 34(7):e2988, pp. 1 - 17, 2018.

4.1 Introduction

In Chapter 3, we have proposed a method to estimate a set of activation points that are compatible with an observed activation on a simple, flat domain Ω. In order to apply this method to the problem of patient-specific PKN estimation, we need to extend the previous algorithm to a domain that properly represents the surface of the human ventricle. In this Chapter we generalize the ideas presented in Chapter 3 to make them suitable for a ventricle represented by a triangle mesh that can be obtained from Medical Image.

It is worth to mention that a proper estimation of the PMJs is necessary in a computer model of the heart not only to reconstruct the structure that connects them. Besides the simulation of the normal activation, PMJs play a very relevant role in a number of pathologies such as left bundle branch block, or sustained ventricular tachycardia macro-reentries [58, 32, 86, 30] in which the PKN is retrogradely activated and used to transport the electrical impulse [61].

Previous studies in the literature have never tried to estimate the location of PMJs from EAM data. Instead, they look for PMJs that were in-line with local observations in a EAM, such as local minima [71], which does not include all the potential sources of activation. In other studies, random PMJs were placed, and subsequently moved in a limited area to limit the error in the measurements points, but never with the goal of looking for actual PMJ locations [69].

In this chapter, we present a novel method to estimate the location of PMJs from simulated EAMs directly on a 3-dimensional realistic representation of the ventricles extracted from MRI. The algorithm can track back the activation sources on the endocardium and approximate their location and corresponding activation times. The estimation method explicitly considers the uncertainty associated to the samples used to estimate the PMJs. These errors may arise from the positioning error (tip of the recording catheter) of the acquisition system or the error in annotating the local activation times (LATs) from the bipolar and unipolar signals. They are introduced by including Gaussian noise in the sampled LAT maps.

4.2 Material and methods

We will consider synthetic PKN scenarios on 3-dimensional domains, that represent the ventricular-endocardium surface. Note that since the PKN is comprised within the endocardial layer, we do not need to consider the myocardial volume in our analysis. In our method, the inputs are the local tissue activation times at a set of scattered measurement points. The activation time and location of measurement will be altered by some random error with known standard deviation σ. From this information, our goal will be to estimate a set of electrical source points on the mesh (i.e. PMJs) that explains the observed activation times.

For the purpose of our study, the ventricular endocardium can be considered as a surface embedded in $\mathbb{R}^3$ and, in our computational approach, we will use a homogeneous simplicial 2-complex to discretize the surface of the endocardium. This corresponds to the kind of data that can be obtained from medical image in the form of a triangle mesh. In this domain, we will consider the distance defined in Ω as the minimum length of the piecewise linear curves contained in Ω connecting two given points, that will be computed using a Fast Marching algorithm [87]. Under this scenario, the analytical approach that was used in Chapter 3 is not available and, thus, we need to generalize it. In order to do this, we will turn around the approach; in Chapter 3 we took measurement points and sought for the possible source, and now we are going to take potential sources and evaluate their compatibility with the data. We will start with a characterization of the PMJs, and develop the method upon it.

4.2.1 PMJ characterization

We assume that the activation of the ventricular CCS triggers at certain (unknown) source points, i.e. PMJs, the tissue depolarization that spreads through the endocardial surface at a speed v (we neglect the transmural electrical propagation). At a given location $\mathbf{p} \in \Omega$, we define its activation time as

$$t(\mathbf{p}) = \min_{\mathbf{s}\in\mathcal{S}} \left(\tau(\mathbf{s}) + \frac{d(\mathbf{p},\mathbf{s})}{v} \right), \tag{4.1}$$

where $\mathcal{S}$ is the set of source points, $\tau(\mathbf{s})$ the activation time of source $\mathbf{s} \in \mathcal{S}$ and $d : \Omega \times \Omega \to \mathbb{R}$ is the aforementioned distance on Ω. Note that the

activation time for each source is specific. We will say that $\mathbf{s}$ *has activated* a location $\mathbf{p} \in \Omega$ if the minimum in (4.1) is achieved for $\mathbf{s}$.

We consider a finite set $\mathcal{P} \subset \Omega$ representing N measurement points $\mathbf{p}_i$, $i = 1, \ldots, N$. For every measurement point, $\mathbf{p}_i \in \mathcal{P}$, its measured Local Activation Time (LAT) is given by $t_i = t(\mathbf{p}_i) + Z$, where Z is a Gaussian random variable $Z \sim N(0, \sigma^2)$. For a source point, $\mathbf{s}$ we define the set $A(\mathbf{s}) = \{\mathbf{p}_i : \mathbf{p}_i \text{ has been activated by } \mathbf{s}\}$, and the set of indexes $I_A(\mathbf{s}) = \{k : \mathbf{p}_k \in A(\mathbf{s})\}$. Indeed, these sets are defined for any point $\mathbf{x} \in \Omega$, even if $\mathbf{x} \notin \mathcal{S}$, but $A(\mathbf{x}) = I_A(\mathbf{x}) = \emptyset$ if $\mathbf{x}$ has not activated any measurement point.

Let us now consider an arbitrary point $\mathbf{x} \in \Omega$. If $\mathbf{x}$ is actually a source point, and $\mathbf{p}_i \in A(\mathbf{x})$ has activation time t_i, then, by propagating the signal backwards from $\mathbf{p}_i$ to $\mathbf{x}$, the activation time for $\mathbf{x}$ can be estimated as $a_i(\mathbf{x}) = t_i - d(\mathbf{p}_i, \mathbf{x})/v$. This estimation will have a Gaussian error due to Z. If we propagate the signal from every point in $\mathcal{P}$ onto $\mathbf{x}$, we will have the set $\mathcal{T}(\mathbf{x}) = \{a_i(\mathbf{x}) : i \in 1, \ldots, N\}$. This set can be partitioned into the two disjoint subsets $\mathcal{T}(\mathbf{x}) = \mathcal{T}_A(\mathbf{x}) \cup \mathcal{T}_{NA}(\mathbf{x})$, where

$$\mathcal{T}_A(\mathbf{x}) = \{a_i(\mathbf{x}) : i \in I_A(\mathbf{x})\}; \qquad \mathcal{T}_{NA}(\mathbf{x}) = \{a_i(\mathbf{x}) : i \notin I_A(\mathbf{x})\}. \tag{4.2}$$

For all the time estimations $a_i \in \mathcal{T}_A(\mathbf{x})$, coming from points activated by $\mathbf{x}$, we have that

$$a_i(\mathbf{x}) = t_i - \frac{d(\mathbf{p}_i, \mathbf{x})}{v} = \tau(\mathbf{x}) + \frac{d(\mathbf{p}_i, \mathbf{x})}{v} + Z - \frac{d(\mathbf{p}_i, \mathbf{x})}{v} = \tau(\mathbf{x}) + Z, \tag{4.3}$$

where $\tau(\mathbf{x})$ is the actual (unknown) activation time of $\mathbf{x}$. Thus, all these values are samples of the same Gaussian random variable $a_i \sim N(\tau(\mathbf{x}), \sigma^2)$.

On the contrary, for any value $a_i \in \mathcal{T}_{NA}$, the associated value of t_i depends on the source $\mathbf{s}$ that activated $\mathbf{p}_i$ and on the distance from $\mathbf{p}_i$ to $\mathbf{s}$

$$a_i(\mathbf{x}) = t_i - \frac{d(\mathbf{p}_i, \mathbf{x})}{v} = \tau(\mathbf{s}) + \frac{d(\mathbf{p}_i, \mathbf{s})}{v} + Z - \frac{d(\mathbf{p}_i, \mathbf{x})}{v} \tag{4.4}$$

and, as a consequence, the values of these a_i are random variables with mean values μ_i that will not be, in general, equal. The values $a_i \in \mathcal{T}_{NA}$ will have an additional property; since point $\mathbf{p}_i \notin A(\mathbf{x})$, it has not been activated by $\mathbf{x}$, and we have by definition of t_i,

$$t_i \leq \tau(\mathbf{x}) + \frac{d(\mathbf{p}_i, \mathbf{x})}{v}, \tag{4.5}$$

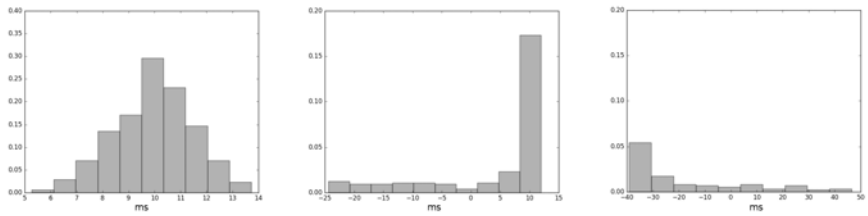

Figure 4.1: Distribution of the values of a_i for a simulated scenario. Left histogram shows all the values of $a_i \in \mathcal{T}(\mathbf{s})$ at a source point $\mathbf{s}$ in a scenario with a single source point. Central histogram shows all the values $a_i \in \mathcal{T}(\mathbf{s})$ at a source point $\mathbf{s}$ in a scenario with two source points. Right histogram shows the values $a_i \in \mathcal{T}(\mathbf{x}')$ at a point $\mathbf{x}'$ that is not a source point. Noise in all scenarios was included using a Gaussian with a standard deviation of 1.5.

and, then, for the value of a_i we have that

$$a_i(\mathbf{x}) = t_i - \frac{d(\mathbf{p}_i, \mathbf{x})}{v} \leq \tau(\mathbf{x}) + \frac{d(\mathbf{p}_i, \mathbf{x})}{v} + Z - \frac{d(\mathbf{p}_i, \mathbf{x})}{v} = \tau(\mathbf{x}) + Z \quad (4.6)$$

and all $a_i \in \mathcal{T}_{NA}(\mathbf{x})$ are Gaussian random variables with mean $\mu_i \leq \tau(\mathbf{x})$.

As stated earlier, this development is valid no matter whether $\mathbf{x}$ is a source point or not. But in the former case, the set $\mathcal{T}_A(\mathbf{x})$ is empty and all the values in $\mathcal{T}(\mathbf{x})$ are variables with mean values given by Equation (4.4). To define our method, we propose a characterization of source points based on this property; our goal is to find those points $\mathbf{s} \in \Omega$ for which the set $\mathcal{T}_A(\mathbf{s})$ is not empty.

In Figure 4.1 we show the distribution of values of $\mathcal{T}(\mathbf{x})$ in different simulated scenarios. The leftmost histogram shows the distribution of $\mathcal{T}(\mathbf{s})$ at the source point $\mathbf{s}$, for a scenario with a single source point, showing a frequency distribution consistent with a normal distribution. In the middle figure, we show the frequency distribution of $\mathcal{T}(\mathbf{s})$ at a source point $\mathbf{s}$, in a scenario with two source points, showing a tail on the left side of the histogram. This tail corresponds to the values in $\mathcal{T}_{NA}(\mathbf{s})$, which in this case are measurement points activated by the second source. The rightmost histogram shows again the distribution of the whole set $\mathcal{T}$ for a non-source point, $\mathbf{x}$, in the scenario with two source points. Since $\mathbf{x}$ has not activated any measurement point $\mathcal{T}_A(\mathbf{x}) = \emptyset$ and the distribution shown actually corresponds to the values of $\mathcal{T}_{NA}(\mathbf{x})$.

This characterization identifies those source points that have activated a minimum number of measurement points so that it is possible to observe

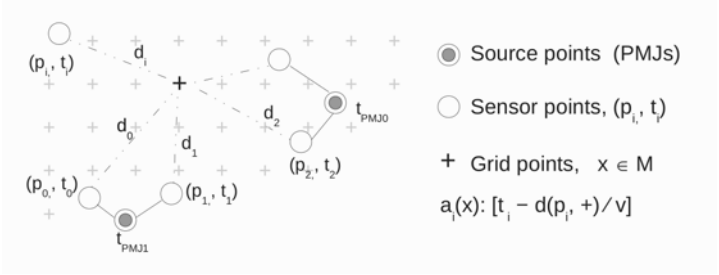

Figure 4.2: Simplified grid scenario. Measurement points are defined by the position p_i and their LAT t_i. Distance between measurements points and any point of the grid, d_i, is obtained by the Fast Marching algorithm.

them as a peak in the histogram, see Figure 4.1 central panel. Indeed, we consider as non-source any point where the set $\mathcal{T}_A$ is not higher than a given threshold. This property makes it possible to identify sources that explain the observation $\mathcal{P}$. But the total number of sources that can be identified depends on the size and distribution of this observation. This issue will be discussed in the results section.

4.2.2 Algorithm description

As we said before, in our numerical approach, the domain Ω is a homogeneous simplicial 2-complex that corresponds to a discretization of the surface of the endocardium. The set of measurement points $\mathcal{P}$ is formed by some of the vertices of this triangular mesh. This constraint is motivated by the fact that in a real clinical setting, the mesh is built from the measurement points $\mathcal{P}$ and therefore these are always nodes of the final mesh. Every measurement point $\mathbf{p}_i \in \mathcal{P}$ has a local activation time, t_i (see Figure 4.2). Our method will result in a set $\mathcal{S}$ of estimated source points that will also be vertices of the mesh.

We propose a method with two main steps, described in Algorithm 2 and Algorithm 3. In the first step (Algorithm 2), we look for a set of PMJ checking if a mesh point $\mathbf{x}$ can be a source point according to the characterization described in Section 4.2.1 and the measured data. In a second step, once a set of estimated sources has been built, we will reduce the number of estimated PMJs by removing points that are in the neighborhood of other estimated PMJ and that have a small influence on the activation map prediction. This step is described in Algorithm 3.

At the beginning of the first step, given the set of all measurement points $\mathbf{p}_i \in \mathcal{P}$, we compute the distance between every point in the triangle mesh M and every point in $\mathcal{P}$. To do so, we simulate the propagation of a signal from every point in $\mathbf{p}_i \in \mathcal{P}$ by solving the isotropic Eikonal equation [88] as in [72] by a fast marching algorithm [87]. This distance computation is performed only once, before we start the estimation of the set $\mathcal{S}$. Note that since we are using the isotropic Eikonal equation, distances and activation times on the mesh nodes are proportional. Figure 4.2 shows a simplified scenario, where the discretization is represented by a regular grid on a flat domain, and the distances d_i are obtained for every pair formed by a measurement point and grid point.

Algorithm 2 Estimation of candidate electrical sources from measurement points

1: **for all** $\mathbf{x} \in M$ **do**
2: $\quad \mathcal{T} \leftarrow [a_i(\mathbf{x}) : a_i(\mathbf{x}) = t_i - d(p_i, x)/v \quad \forall (p_i, t_i) \in MeasurePoints]$
3: $\quad \mathcal{T} \leftarrow sort(\mathcal{T}, decreasing)$
4: $\quad \mathcal{T}_{ok} \leftarrow \mathcal{T}[1:n] : Test(\mathcal{T}[1:n])$
5: $\quad$ **if** $(n \geq 3)$ **then** {Focus candidate}
6: $\quad\quad$ Add $(\mathbf{x}, \mathcal{T}_{ok})$ to $listCSP$
7: $\quad$ **end if**
8: **end for**
9: **Output** $\leftarrow listCSP$

Using the t_i of all the measurement points $\mathbf{p}_i \in \mathcal{P}$ and the computed distances, we estimate the backwards activation time for each point $\mathbf{x}$ in the mesh, $a_i(\mathbf{x})$ (lines 2 and 3 in Algorithm 2). As a result, we have the set $\mathcal{T}(\mathbf{x})$ for every point in the discretized domain. Next, the method will examine this set for every point $\mathbf{x} \in M$, to decide whether it can be considered a source point, i.e. if we have a nonempty set $\mathcal{T}_A(\mathbf{x})$ for each point $\mathbf{x} \in M$ (line 4 of the pseudocode). We know, from equation (4.6), that the variables in $\mathcal{T}_A(\mathbf{x})$ have a common mean that is higher than any mean values of the variables in $\mathcal{T}_{NA}(\mathbf{x})$. Thus, we will take the n largest values of $\mathcal{T}(\mathbf{x})$. Let $\mathcal{T}_n$ be the subset of $\mathcal{T}(\mathbf{x})$ with the n largest values. If the values in $\mathcal{T}_n$ have been generated by a common Gaussian distribution, with standard deviation σ and unknown mean value $\tau(\mathbf{x})$, we can assume that $\mathcal{T}_n \subseteq \mathcal{T}_A$.

This test will be performed for increasing values of n, until we reach the one for which the times in $\mathcal{T}_n$ set are not consistent with a Gaussian distribution. If the test indicates that $\mathcal{T}_n \subset \mathcal{T}_A(\mathbf{x})$ for at least, $n = 1, 2, 3$, then we

will consider that $\mathcal{T}_A(\mathbf{x}) \neq \emptyset$ and as a consequence, $\mathbf{x} \in (S)$ (lines 5-7 of Algorithm2). The reason why three positive tests are requested is that at least three measurement points are required to exactly compute a source in absence of noise in the data as shown in Chapter 3 [73]. This value could be increased, to require a higher value of n before a point is considered to be a source, reducing the number of estimated points.

The main decision in Algorithm 2 relies on the test to decide whether a set of values $\mathcal{T}_n$ is a sample of a Gaussian distribution (line 4). The natural approach to perform this test would be a hypothesis contrast, or a normality test. However, in our problem, the size of the sample will be, in general, small ($n < 10$) since the total number of measurement points will be of hundreds or, in the best cases, of a few thousands. Depending on the number of PMJs in the scenario, the value of $|\mathcal{T}_A|$ will be rather small for most of the source points. Taking into account these considerations, we find that most tests will not meet the requirements to perform a significant hypothesis contrast. In turn, we will focus on the fact that we know the standard deviation, σ, of the values in $|\mathcal{T}_A|$ and we set the following criterion to test if $\mathcal{T}_n \subset \mathcal{T}_A$. Given a point $\mathbf{x} \subset M$ and an $n \geq 3$, we compute the mean of the $a_i(\mathbf{x})$, denoted as $\bar{t}_n$, and we consider that the point $\mathbf{x}$ is a candidate source point, $\mathbf{x} \in \mathcal{S}$, if

$$\max_{a_i \in \mathcal{T}_n} (|a_i - \bar{t}_n|) \leq \alpha\sigma,$$

with α a parameter to determine the sensitivity of the decision and σ the standard deviation of the measurements, defined in Section 4.2.1. If the point $\mathbf{x}$ meets this criterion, it is stored in the list $listCSP$ and it is assigned the activation time $\tau(\mathbf{x}) = \bar{t}_n$. Along with each possible source point, we store the largest value of n for which we obtain a positive result and the set of points $\mathbf{p}_i$ associated to the values in $\mathcal{T}_n$.

As a result of Algorithm 2, we have a list of Candidate Source Points (CSP) which represents a first estimation of $\mathcal{S}$. This first estimate will be denoted as $\mathcal{S}^0$. Figure 4.3 shows two outputs of Algorithm 2. In both examples two PMJs, represented by stars, are shown. The set of red circles corresponds to the estimated CSPs, generated from the measurement points (small crosses). The figures show that Algorithm 2 gives a resulting list with many false positives. From Eq. (4.4), it can be seen that for a point $\mathbf{x}$ that is near a source point $\mathbf{s}$, the terms involving distance are similar in magnitude and will almost cancel each other. As a consequence, points that are near to source points are also likely to be detected as such.

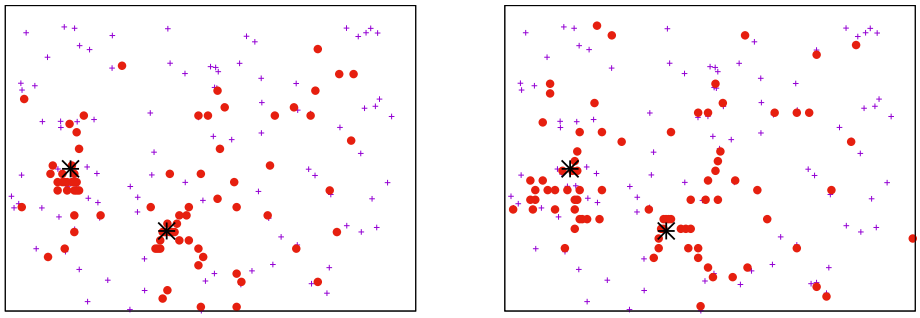

Figure 4.3: Candidate Source Points (red circles) after the application of Algorithm 2 for two real sources (stars) with a deviation in the error of 0.5ms (Left) and 1.5ms (Right). Measurement points are represented with small crosses. The signal propagates from the lower left corner of the image to the upper right corner. It can be observed that spurious candidate sources appear, specially near the actual source points.

To reduce the number of false positives, we apply a second step, described in Algorithm 3. Starting from $listCSP$, we process the points again to remove spurious points and obtain a more accurate set of PMJs. In this second step, every CSP in $\mathcal{S}^0$ is given a score that is intended to assign high values to actual PMJs and low values to spurious ones. The function we use to score the candidates is $-\tau(\mathbf{x})$. The motivation for this function is that PMJs are activated through the Purkinje network, where propagation speed is faster than in working myocardium and, as a consequence, CSPs with a later activation time are more likely to be false estimates. Therefore, the set of CSPs is ordered according to this score so that we first assess the elimination of those points with lower score value (higher activation time). For each point, we evaluate if the resulting set $\mathcal{S}$ still explains the observed activation properly, that is with similar or lower error.

We start the second step of the method by computing the estimated t_i of every measurement point $\mathbf{p} \in \mathcal{P}$ using equation (4.1). This t_i is computed using the estimated sources, and allows us to assign to every CSP the list of the measurement points it has activated. The value of the score is also computed for every CSP (line 1 of Algorithm 3, in $CalculateScore$). Then, we take the CSP, $\mathbf{x} \in \mathcal{S}^0$, with the lowest score value, we remove $\mathbf{x}$ from the set $\mathcal{S}^0$ and try to reassign the set of points it activated, $A(\mathbf{x})$, as follows. Given a point $\mathbf{p}_i \in A(\mathbf{x})$, we consider $\hat{\mathbf{s}} \in \mathcal{S}^0$, with $\hat{\mathbf{s}} \neq \mathbf{x}$, and we take the backwards electrical propagation $a_i(\hat{\mathbf{s}})$ that was computed in the first step of the method. We compute the distance from $a_i(\hat{\mathbf{s}})$ to the estimated activation

time $\delta_{i,\hat{\mathbf{s}}} = |\tau(\hat{\mathbf{s}}) - a_i(\hat{\mathbf{s}})|$. For every point $\mathbf{p}_i \in A(\mathbf{x})$, we will say that it *can be reassigned* to source $\hat{\mathbf{s}}$ if $\delta_{i,\hat{\mathbf{s}}} \leq \beta\sigma$, where $\beta > 0$ is a parameter that determines how restrictive we are to allow a point to be reassigned. Once this information has been computed for all the measurement points, we will establish that the candidate $\mathbf{x}$ can be removed if all the points in $A(\mathbf{x})$ can be reassigned to another source in $\mathcal{S}^0 - \{\mathbf{x}\}$. This evaluation is performed by procedure *CanBeReassigned* in line 5 of Algorithm 3, returning true only if all the points in $A(\mathbf{x})$ can be reassigned within the tolerance defined by parameter β. The method *Reassign* in line 6 takes the measurement points in $A(\mathbf{x})$ and reassigns them to the best remaining candidate sources in the list. If the point $\mathbf{x}$ cannot be removed, then it is inserted again in $\mathcal{S}^0$. This process is repeated for all the CSPs, in increasing order of the score. Once this process is completed for all the points $\mathbf{x} \in \mathcal{S}$, we will have a new set of estimated source points, $\mathcal{S}^1 \subseteq \mathcal{S}^0$. The complete process is repeated to build a sequence of estimations $\mathcal{S}^0 \supseteq \mathcal{S}^1 \supseteq \cdots \supseteq \mathcal{S}^k$ until we reach an iteration in which $\mathcal{S}^k = \mathcal{S}^{k+1}$, which means that no point in $\mathcal{S}^k$ can be removed. The set of source points resulting from this process, $\hat{\mathcal{S}} = \mathcal{S}^k$, is taken as the final estimation of $\mathcal{S}$. This process can also be stopped after a fixed number of iterations. Indeed, according to our experiments, most of the CSP removal is done in the first iteration.

Algorithm 3 CSP reduction

```
1: listCSP2 ← CalculateScore(listCSP)
2: listCSP2 ← sort(listCSP2, key = score)
3: repeat
4:    changed ← False
5:    for all (x, A(x)) ∈ listCSP2 do
6:       if (CanBeReassigned(A(x), listCSP2 − {x}) then
7:          Reassign(A(x), listCSP2)
8:          listCSP2 ← CalculateScore(listCSP2)
9:          changed ← True
10:      end if
11:   end for
12: until not(changed)
13: Output ← listCSP2
```

4.2.3 Experiments

We have set up a series of experiments to test the proposed methodology. Since the new PMJ estimation method intends to generalize the method of Chapter 3, we start our evaluation on an Euclidean 2-dimensional domain where we can compare them. Then, to test the methodology in a realistic scenario, we use a 3-dimensional model of the left ventricular endocardium that includes different complex computer generated Purkinje networks. The ventricular mesh has been obtained from a virtual population of segmented hearts built from medical imaging of real patients [89]. The human ventricular model has the following dimensions: 8.65 cm (long axis) x 5.22 cm (short axis). The endocardial mesh, where the Purkinje networks are deployed, is made of 42144 triangular elements and 21189 nodes.

4.2.3.1 Experiments on Euclidean, 2-dimensional scenarios

The set of 2-dimensional planar scenarios reproduce those described in Chapter 3 and in [73] to test the algorithm presented therein to estimate a set of PMJ from measured data. In that work, LATs were free of error. The main goal of this test is to evaluate the performance of the new method proposed here, compared to the algorithm described in Chapter 3 applied to noise free data.

In these tests, the scenarios are rectangular regions with an area similar to that of a human left ventricle, and we use simplified versions of a PKN in the ventricle, based on a binary tree. The trees are built randomly by creating a number of main branches, and building ramifications of this branch up to a given depth d. A higher value of d leads to more PMJs distributed around the main branch. The trees have been built using four different configurations, with ten random trees of each type. Two of the configurations have a single main branch, and use depth $d = 2$ and $d = 4$ in the sub-branch generation. The other two configurations consider three main branches, spanning parallel to each other, and with the same values for d. In Figure 4.4 two of the scenarios are shown: B3D2 with 34 PMJs and B3D4 with 130 PMJs. For further details on the procedure to build the different tree models see 3 and [73].

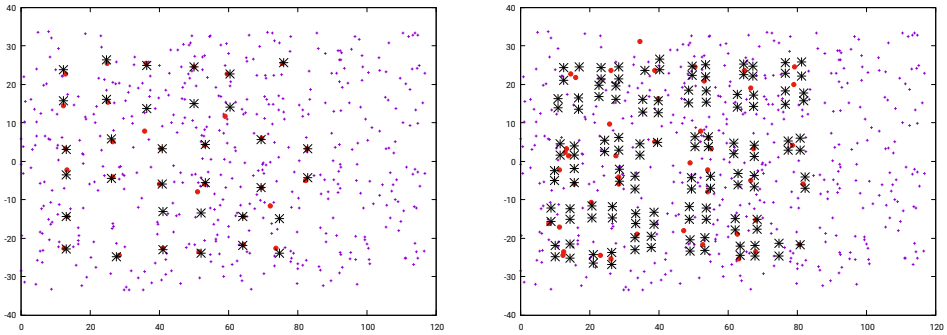

Figure 4.4: 2-dimensional scenarios with random set of measurement points (small crosses), real sources (stars) and location of estimated source points (red circles). Standard deviation in the measurement error of 0.5ms. Left: Example of B3D2 scenario with 34 PMJs. Right: Example of B3D4 scenario with 130 PMJs. Units are in mm.

4.2.3.2 Experiments on 3-dimensional human ventricles

The second set of tests is performed on a left ventricular mesh generated from a virtual population constructed from a set of segmented medical images. On these 3-dimensional models we built synthetic PKNs using the stochastic method described by [7]. A total of 20 different scenarios with diverse PKN morphology, number of PMJ (varying from 213 to 1228), and heterogeneity in PMJ density were built. These scenarios will be referred to as PK1,..., PK20. The activation maps generated by Purkinje trees built with this method were already validated in [7], by analyzing the activation sequence and the total activation times. Figure 4.5 shows the structure and location of PMJs for three different PKNs with low, medium and large amount of PMJs. The real LAT for the PMJs was calculated considering the activation of atrio-ventricular node at $t = 0ms$ and a constant conduction velocity in the PKN of $3m/s$.

For each scenario we studied the effect of the number of measurement points by placing different sets with an increasing density (100, 250, 500, 1000, 1500 and 2000) uniformly distributed as in a real EAM acquisition. To make the results independent of the measurement point locations, for each set size we randomly sampled (Mersenne twister random engine) the endocardium 10 different times. Results are provided for the average of the 10 different sampling sets. The correct LATs for these measurement points are calculated propagating a signal from the PMJs to all the computational nodes in the domain, by solving the isotropic Eikonal equation using a fast marching

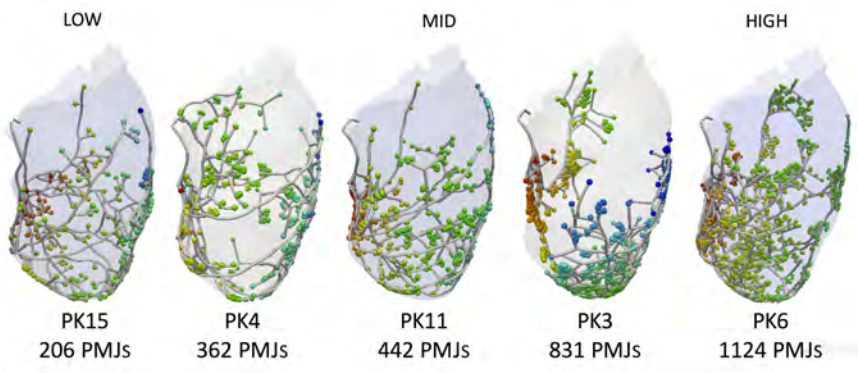

Figure 4.5: Purkinje tree models developed with an increasing number of PMJs and PMJ density. As can be observed the distance between PMJs is lower in PK3 and PK6.

algorithm [87]. Once the actual LAT for each measurement point is known, we add Gaussian noise to the LAT as described in section 4.2.1, with a mean of 0 and a standard deviation ranging from 0 ms to 5.0 ms (in particular: 0ms, 0.5ms, 1.5ms, 2.5ms and 5.0ms).

In order to measure the quality of estimated PMJ sets we use two main indicators. First, we compare the activation map generated by propagating the electrical signal from the estimated PMJs to the real activation map, at all the nodes of the computational mesh (21189 nodes). We take the absolute value of the difference in the activation time at every mesh node as the error at that point, and measure the error of the activation map as the mean absolute error over all the points in the mesh. As a second quality indicator, we consider the distance from each estimated PMJ to the closest real PMJ. This distance indicates if the method has located a false estimated PMJ far from the actual Purkinje tree. This situation is indicated by the appearance of large values of this error measure.

4.3 Results and discussion

The method proposed has been applied to the synthetic 2-dimensional scenarios described in Section 4.2.3.1. A set of 1000 measurement points have been generated with a uniform random distribution on the simulation region, and Gaussian noise has been added to the computed LATs. The tests have been repeated for different values of standard deviation σ^2.

Scenario		Gaussian Error 0.5		
Num.	PMJ	Est. PMJ	Abs. Error(ms)	D. Fe-F(mm)
B1D2	11.7 ± 0.5	18 ± 3	0.22 ± 0.07	0.34 ± 0.05
B1D4	43.9 ± 2.5	42 ± 4	0.33 ± 0.05	1.11 ± 0.16
B3D2	35.4 ± 0.9	40 ± 3	0.28 ± 0.03	1.52 ± 0.24
B3D4	132.2 ± 3.6	68 ± 5	0.46 ± 0.04	2.71 ± 0.16
Scenario		Gaussian Error 2.5		
Num.	PMJ	Est. PMJ	Abs. Error(ms)	D. Fe-F(mm)
B1D2	11.7 ± 0.5	16 ± 3	1.02 ± 0.48	1.72 ± 0.32
B1D4	43.9 ± 2.5	17 ± 3	1.12 ± 0.33	3.31 ± 0.31
B3D2	35.4 ± 0.9	25 ± 3	1.21 ± 0.18	4.49 ± 0.39
B3D4	132.2 ± 3.6	25 ± 3	1.29 ± 0.14	5.25 ± 0.32

Table 4.1: Results for 2-dimensional scenarios with 1000 measurement points and Gaussian noise with a standard deviation of $\sigma = 0.5$ms and $\sigma = 2.5$ms. Column *Num* identifies the scenario, *PMJs* represents the number of PMJs in the scenario, *Est. PMJs* is the number of estimated PMJs by the algorithm, *Abs. Error* is the mean of the absolute error in all the points of the mesh and *D. Fe-F* is the distance from an estimated PMJs to the nearest real PMJ.

Table 4.1 shows the results obtained for the different types of trees, considering the number of main branches and bifurcation depth. The table shows the average results for the 10 synthetic Purkinje trees built using the same parameters. The first column indicates the tree configuration. In the labels, the number alongside label B indicates the number of main branches and the number following label D the depth of the ramification. The second column indicates the average number of PMJs in that configuration. The following columns show the results for two magnitudes of the measurement error; $\sigma = 0.5$ and $\sigma = 2.5$. For each value of σ, the first column indicates the average number of estimated PMJs that are found by the algorithm, the second column indicates the average absolute error of the resulting activation map and the third column shows the maximum distance from the estimated PMJs to the real ones.

Figure 4.6 shows the evolution of the mean absolute error for the scenarios B3D2 and B3D4 when changing the number of measurement points (size of input data). From the results we can see that errors are kept low independently of the number of measurement points. Moreover, although the error grows as σ increases, observed errors are always lower than the standard error introduced in the samples, even for just 100 measurement points in some cases. It is noteworthy that the number of measurements

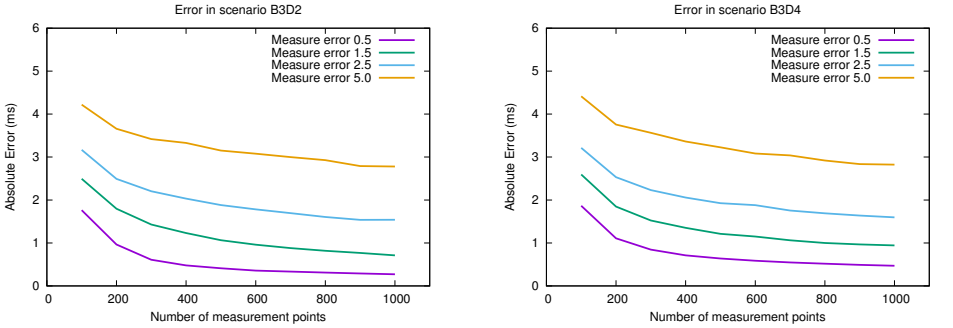

Figure 4.6: Absolute error for scenarios B3D2 and B3D4 with different number of measurement points and a standard deviation error in the measurement of 0.5, 1.5, 2.5 and 5.0 milliseconds.

is often over 500 in real acquisitions during catheter ablation interventions. These results improve the errors obtained in Chapter 3 and in our previous work [73] which, despite the absence of error, were larger for all the number of measurement points analyzed. The results for $\sigma > 0$ cannot be compared, since the method in the previous work was not able to handle error in the measurement data, and the errors grew as σ was increased. However, results shown in Chapter 3 show absolute errors larger than $10ms$ for sets with less than 200 measurement points, while the new method can obtain absolute errors below $4ms$ even in presence of errors of $0.5ms$ in the samples. In addition, it converges to values below $0.5ms$ in absolute error when the number of samples increases.

The study in 3-dimensional ventricles focused on the estimation of PMJs from 20 distinct synthetic PKN. A summary of the different PKN properties, including number of PMJs, and mean density and standard deviation of PMJs per segment (17 AHA segment division), can be seen in Table 4.2, and tables in Appendix A.1. For each PKN configuration, the corresponding LAT map was generated by firstly simulating the signal propagation on the tissue, and secondly randomly sampling (as in a real EAM) the endocardium using an increasing amount of measurement points to study the effect of the sampling density on the results accuracy. Since the endocardial sampling was random, each sampling size was repeated 10 times for each configuration, and results were averaged. Finally, we introduced Gaussian noise in all the samples with different standard deviations. As a result of all the combinations we obtained 6000 different scenarios for which PMJs were estimated. Table 4.3 (the full set of results is summarized in the tables of Appendix A.1) summarizes the average results for six selected PKN us-

ing 1000 measurement points, which is a feasible amount for an EAM, and two different levels of Gaussian noise ($\sigma = 0.5ms$ and $\sigma = 2.5ms$). Note that clinical studies that use contact-mapping catheter systems such as [90] (CARTO3, Webster BioSense Inc.), or non-contact-mapping catheters [35] (Rhythmia mapping, Boston Scientific) have reported that they could collect 1000 measurement points (3-5 minutes), and 4227 measurement points (6.1 minutes), respectively.

When we introduced Gaussian noise with a standard deviation of $0.5ms$ in the measurements, the absolute LAT error obtained in the estimated PMJs for the whole mesh ranged between $0.5ms$ and $0.9ms$. The average distance from the estimated PMJs to the real PMJs (D. Fe-F) ranged from 1.1mm to 1.5mm. This means that the algorithm finds the more influential PMJs and only a small number of estimations do not correspond to real ones. Figure 4.7 shows the estimation results for PK15, which includes 206 PMJs. Real PMJs are represented by circles, while estimated PMJs are displayed as squares. When PMJs are not clustered, the algorithm matches their location with high accuracy. In regions with clustered PMJs, some representative PMJs are detected, that summarize the whole activity in the area. In Figure 4.7 detail, it can be observed that incorrectly estimated non-existent PMJs produce an early activation in the region (label '1', bluish colours), while missing the detection of a PMJs produces a late activation in the region (label '2', redish colours). However, most of the PMJs are correctly estimated, and therefore when activation is triggered from estimated PMJs the error in the mesh is close to 0. For Gaussian noise with a standard deviation of $2.5ms$ the absolute errors obtained in the mesh were still low, around 1.7ms in average, specially when compared with the deviation in the measurement introduced. However, the distance error clearly increased with values ranging from 1.9mm to 4.0mm. As we increased errors in the measurements, there was an increasing possibility of estimating erroneous PMJs.

In Figure 4.8 we have a representative selection of the scenarios visualized in 3D where the surface meshes are colour-coded with the absolute LAT error on the mesh, that is the difference between the real LAT and the new LAT calculated from the estimated PMJs. As can be observed in the first row (measurement error of 0.5ms) almost all meshes show a local error in the range of -2ms to 2ms. In the second row (measurement error of 2.5ms) local errors increased in several areas, where both false and underestimated PMJs occurred. In blue colour we have regions that were activated too early by the estimated PMJs, and in red colour areas that were activated later

than ground truth. Among the reasons that produced the underestimation there is the lack of measurement points in certain areas due to the random mapping, or the summarization in groups of PMJs detected by the algorithm. On the other hand, false PMJs were added because several CSPs belonging to the same source were not correctly merged in the second step of the method due to an excessive error in the measurement points. The creation of an excessive number of false PMJs can be controlled increasing the parameter β commented in section 4.2.2, but then more PMJs will be clustered together.

The plots in Figure 4.9 show the variation of the absolute LAT error as we increase the number of measurement points with different levels of Gaussian noise. We can observe that in general, the absolute error decreases with more measurement points except when the Gaussian noise introduced in the measurements is too high. With Gaussian noise with a standard deviation of 5.0ms, the absolute error increases with the number of measurement points, due to the inclusion of spurious PMJs in the estimated set. This clearly represents a limit in the error admitted by the actual algorithm. We can also see in the plots that in the scenarios with a low density of PMJs and with small deviations in the error, the absolute LAT error tends to zero. The plots in Figure 4.10 show the variation in the distance from estimated PMJs to real PMJs for the same scenarios. In these plots we observe that for small standard deviations (0.0ms and 0.5ms) in the measurement error, the mean distance between real and estimated PMJs decreases as we increase the number of measurement points. However, when higher errors in the measurement points ($> 1.5mm$) are introduced, the number of measurement points do not always improve the results. That means that with more error, we estimate PMJs in erroneous positions. We can also notice that the density of PMJs does not have a clear effect in these plots. The distance from estimated PMJs to real PMJs seems to depend more on the geometry of the Purkinje tree than on the number of PMJs.

Other authors have presented in the past algorithms to set the activation sequence of the ventricles using different techniques, but only a few of them are based on clinical data or other types of ground truth data to compare with. The two most common non-personalized approaches are the manual inclusion of endocardial activation triggers in accordance with descriptions in the literature [26], or the generation of synthetic Purkinje trees without a specific patient reference. The latter approach has been performed with different mathematical techniques that range from simple fractal trees [59] to complex and dense network structures based on L-systems [7]. Another

Scenario				
Num.	PMJ	Density	TAT pkj (ms)	TAT (ms)
PK1	1128	94.1 ± 0.7	10.0	51.5
PK3	831	51.9 ± 1.1	15.6	47.4
PK4	362	22.6 ± 0.7	12.7	35.1
PK6	1224	76.5 ± 0.7	11.3	33.0
PK11	442	27.6 ± 0.6	12.8	34.5
PK15	206	14.7 ± 0.6	13.5	35.5

Table 4.2: Information about six representative 3-dimensional scenarios. Column *Num* identifies the scenario, *PMJ* represents the number of PMJs in the scenario, *Density* is the density and standard deviation of PMJs per segment (17 AHA segment division), *TAT pkj* is the Total Activation Time of the Purkinje Network, *TAT* is the Total Activation Time for the whole surface/ventricle.

Scenario		Gaussian Error 0.5		
Num.	PMJ	Est. PMJ (%)	Abs. Error(ms)	D. Fe-F(mm)
PK1	1128	91 ± 4 (8.0)	0.69 ± 0.03	1.19 ± 0.19
PK3	831	95 ± 3 (11.4)	0.67 ± 0.03	1.16 ± 0.11
PK4	362	103 ± 4 (28.3)	0.68 ± 0.04	1.34 ± 0.15
PK6	1224	116 ± 2 (9.5)	0.82 ± 0.03	1.08 ± 0.03
PK11	442	108 ± 3 (24.5)	0.75 ± 0.04	1.41 ± 0.13
PK15	206	86 ± 4 (41.6)	0.60 ± 0.04	1.34 ± 0.15
Scenario		Gaussian Error 2.5		
Num.	PMJ	Est. PMJ (%)	Abs. Error(ms)	D. Fe-F(mm)
PK1	1128	53 ± 3 (4.7)	1.64 ± 0.16	3.37 ± 0.76
PK3	831	56 ± 5 (6.8)	1.63 ± 0.14	2.71 ± 0.41
PK4	362	62 ± 3 (17.0)	1.74 ± 0.13	2.84 ± 0.18
PK6	1224	62 ± 5 (5.0)	1.74 ± 0.10	1.92 ± 0.27
PK11	442	63 ± 3 (14.2)	1.74 ± 0.11	2.58 ± 0.33
PK15	206	53 ± 4 (25.8)	1.67 ± 0.10	3.21 ± 0.33

Table 4.3: Results for six representative 3-dimensional scenarios with 1000 measurement points and Gaussian noise with standard deviation of 0.5 and 2.5. Column *Num* identifies the scenario, *PMJs* represents the number of PMJs in the scenario, *Est. PMJs* is the number of estimated PMJs by the algorithm, *Abs. Error* is the mean of the absolute error in all the points of the mesh and *D. Fe-F* is the distance from an estimated PMJs to the nearest real PMJ.

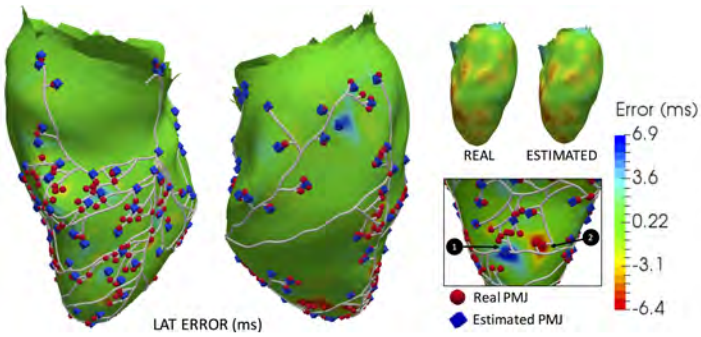

Figure 4.7: Estimation in low PMJ density model. Left panel shows two views of the endocardium where colour correspond to the error in ms between the real LAT and the estimated LAT. LATs obtained with real PMJs and estimated PMJs is depicted in the upper row. A detail of an endocardial region is provided, including real (circles) and estimated (squares) PMJs. Red areas (label 2) correspond to errors where PMJs have not been detected and activation is delayed, while blue areas (label 1) correspond to wrongly estimated PMJs, which activate tissue too early.

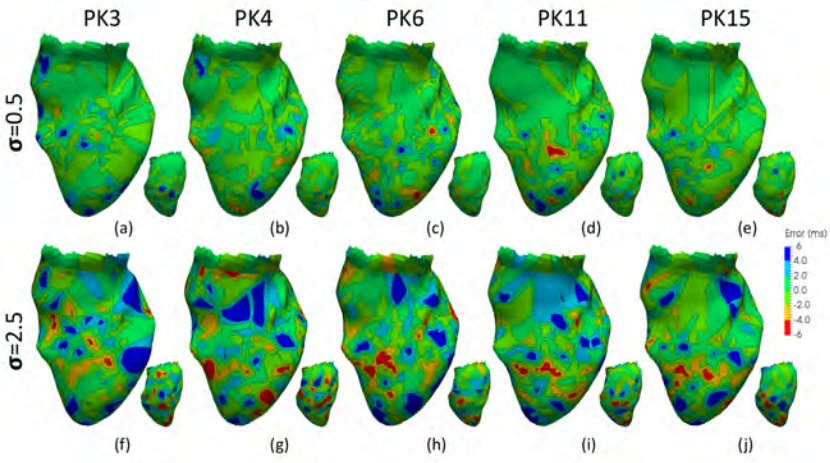

Figure 4.8: Spatial distribution of LAT errors. Local differences in activation times between simulations triggered from real and estimated PMJs. Five different Purkinje tree configuration with differences in PMJ density (see Table 4.3) for which Gaussian noise with standard deviation $\sigma = \{0.5, 2.5\}$ were included in the samples. Errors are colour coded using a scale bar between -6.0ms and 6.0ms. Red colours mean that estimated map activated later than real, and blue colours that estimated map activated earlier.

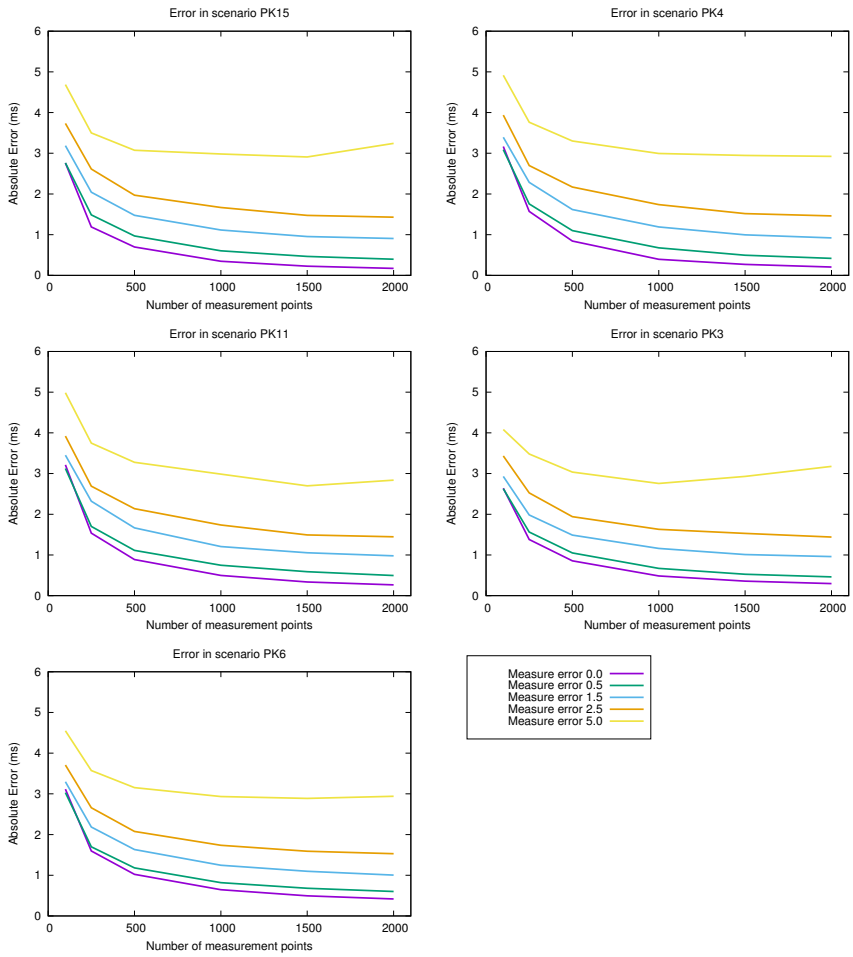

Figure 4.9: Plots of the absolute error for 5 different scenarios in increasing order of PMJs density: PK15, PK4, PK11, PK3 and PK16.

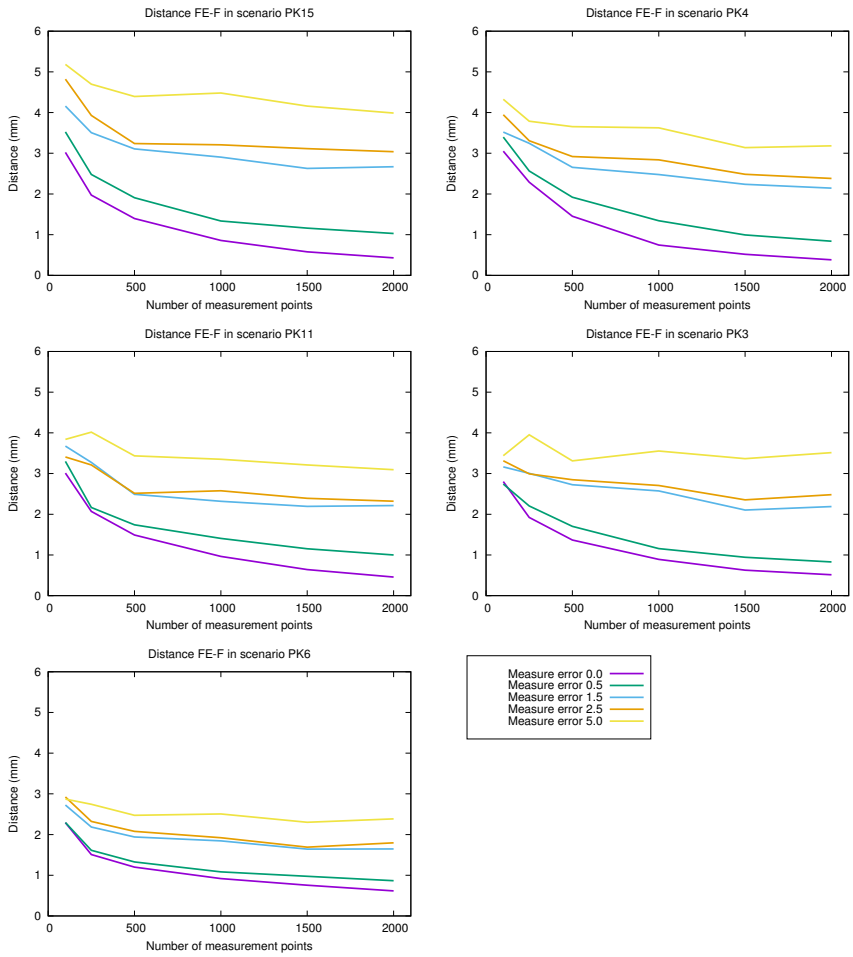

Figure 4.10: Plots of the distance from estimated PMJs to real PMJs for 5 different scenarios in increasing order of PMJs density: PK15, PK4, PK11, PK3 and PK16.

method is based on segmentation of the proximal section of the PKN from ex-vivo biological [82, 11, 63, 23], but PMJs cannot be obtained, except at a few specific locations [22]. However, all those strategies are valid for mechanistic studies, and do not allow to generate patient-specific activation sequences or ECGs, such as those presented in our work. EAM data have been used in different ways to estimate the PKN to subsequently perform simulations of cardiac electrophysiology. In [71] PMJs were obtained from EAMs, previously fit to a reference endocardial model, by calculating sources and sinks from the patient LAT maps. The method used not only the data at the measurement points but all the interpolated information on the mesh, which probably introduced errors in the estimation since the interpolation does not reflect the real activation sequence. LAT errors reported ranged from 5.12 ms to 8 ms. In [69, 72], during the validation analysis, the estimation of PMJs was performed considering previously a synthetic PKN structure, and following moving, adding or deleting PMJs to decrease the error with respect to measurements. The main similarity of our method with the one presented in [72] is that both use the solution of the backward Eikonal equation (from the measurement points to the points in the mesh) to search for (or move/add/delete) candidate PMJs. However, the criterion we define to decide the final PMJs is different to that in [72]. In addition, in our methodology we consider that the samples include Gaussian noise due to the annotation of the measurement points. Finally, in [72] the optimization of the PMJ locations is done per *region of interest* while the method presented here uses a global ranking of the candidate PMJs. In [69], the authors reported mean absolute errors ranged from 4.9 ± 4.1 ms to 9.9 ± 7.5 ms, depending on the subject and the initial PKN, whereas in [72], results were improved significantly. It is important to remark that in both studies patient-specific EAM data were used. For synthetic PKN without noise in the samples, the mean absolute error for 300 measurement points ranged from 1.92 ± 2.00ms to 2.94 ± 2.82 ms depending on the number of test points used for the cross-validation. For an equivalent number of measurement points without noise, we obtained mean absolute errors of around $1ms$ using a cross-validation with 21189 points (i.e. all the endocardial points). With regard to the results including noise, the comparison is difficult since the noise was included in a different way, and we cannot determine which is the equivalent noise between both studies. Finally, in [72] EAMs were used to test the methodology, and results show mean absolute errors of 5.84 ± 4.45 ms for the patient-specific network. Although we do not have results yet for acquired EAMs, these results serve as a reference to indicate that our errors with synthetic EAMs are below these values.

One of the drawbacks of using a previously defined PKN structure, as in [69, 72], is that this imposes a constraint for the location and amount of the PMJs. Thus starting with an inaccurate PKN can affect the quality of the final estimation of the set of PMJs. On the contrary, our approach works directly with the estimation of PMJs locations, which are completely free from any predefined PKN structure. It is also important to remark than only a few studies such as [72] have explicitly considered errors in the clinical measurements. That is relevant, since mapping systems have been reported to introduce errors in the catheter tip position of about 0.7 ± 1.5 mm [34], which have to be added to the errors due to the LAT annotation from the monopolar and bipolar catheter recordings.

So far, there has not been a thorough analysis of the density of Purkinje myocardial junctions in the human heart. There have been a few attempts to describe PMJs in selected regions of the heart such the base of the papillary muscles, or random locations, in a few hearts. Most of the studies that analyze the PK system and PMJs have been carried out in animals, which present a different configuration than in humans. Therefore, applying techniques to estimate the density of PMJs to a large number of human cases can shed some light in the distribution and density of them, allowing to build atlases.

4.4 Conclusions

We have developed a method that is able to estimate the location and activation times (LATs) of PMJs from a 3D representation of the endocardium. From a set of 20 synthetic complex PKN, we have been able to estimate the sources of activation with an average LAT error between 0.5 ms and 0.9 ms in cases where Gaussian noise with an amplitude of $\sigma = 0.5$ was introduced. For higher noise ($\sigma = 2.5$), LAT error increased to 1.7 ms in average.

In conclusion, the method can be used to estimate the PMJs from complex scenarios, similar to those that are expected on real patients. Therefore, it could be applied to real data, that is, patient EAM in sinus rhythm. However, the PKN structure, which is fundamental still needs to be estimated.

5

Estimation of Personalized Minimal Purkinje Systems from Human Electroanatomical Maps

Abstract – The Purkinje system is a heart structure responsible for transmitting electrical impulses through the ventricles in a fast and coordinated way to trigger mechanical contraction. Reconstructing a patient-compatible PKN structure from an EAM is a challenging task, that could help improve models for electrophysiology simulations or provide aid in therapy planning for radiofrequency ablation. In this study, we present a method to build a PKN structure that is inversely estimated from a patient's EAM. First, we carry out a simulation study to show the accuracy of the estimation method for different Purkinje myocardial junction densities and Purkinje morphologies. Second, we estimate the PKN from a set of 28 EAMs from patients with idiopathic ventricular fibrillation, obtaining an optimal conduction velocity in the PKN of 1.95 ± 0.25 m/s, the location of PMJs, the PKN structure, and an average local activation time error of 6.1 ± 2.2 ms. Finally, using the patient-specific Purkinje network, we show good agreement between simulated and real ECG in an exemplary case.

This chapter is adapted from: Barber F., Langfield P., Lozano M., García-Fernández I., Duchateua J., Hocini M., Haissaguerre M., Vigmond E., Sebastian R Estimation of personalised minimal Purkinje systems from human electroanatomical maps. Medical Image Analysis. Under revision.

5.1 Introduction

As it has been previously discussed, it is fundamental to be able to incorporate a PKN in patient-specific biophysical models aimed to simulate and reproduce several types of arrhythmia. However, the construction of a realistic computational PKN for humans is complex, and in general does not provide a patient-specific activation sequence [7]. Therefore, generic PKN models are usually included in 3D ventricles for mechanistic studies [43, 91]. Some methods have already been presented to estimate the PKN from EAMs, by building an initial random network and following reducing the error by moving, adding or pruning branches [72] or looking for local minima from EAMs [71]. However, the goal of those methods was to generate random PKNs compatible with the observed EAM, and not estimating the PKN from the data, or other parameters such as the optimal conduction velocities (CVs) for each patient's PKN.

As we have seen in Chapter 4 using synthetic scenarios and simulations, we can inversely estimate parts of the PKN, such as the set of PMJs, from virtual EAMs. Therefore, the structure can be estimated not from images but from the electrical sequence that produces when it activates.

Since clinical EAMs can be acquired *in vivo* using catheters, we could potentially estimate the PMJs of a patient, but we still need to estimate the structure of the PKN that connects those EAMs. The first step, is to process the EAMs to obtain the spatio-temporal activation map, or LAT map, by annotating the activation time of each of the samples recorded from the patient's endocardium. Following, we have to estimate the location and activation time of the PMJs, and finally the PKN compatible with the activation times of the PMJs, provided a conduction velocity within the PKN.

In this chapter, we present an algorithm to first estimate the location of a set of PMJs from EAMs based on an adapted version of the algorithm presented in Chapter 4 [92] that is able to process real EAMs, and second, build a simplified PKN based on the location and activation time of the PMJs, with an estimated CV for the PKN. The algorithm has been tested on several PKN synthetic configurations, with simulated activation maps, subject to different error amplitudes. The results show that the method is able to estimate a set of PMJs and PKNs that explains the observed activation maps for different synthetic CCS configurations. In the synthetic tests, the average error in the predicted activation time is below the amplitude of the error applied to the data. Moreover, the algorithm has also been ap-

plied to a clinical dataset obtained from EAMs of patients in sinus rhythm without structural heart disease. In real EAMs, errors are subject to the estimated (annotated) LAT error, and geometrical localization of the sample points. We could estimate 28 PKN, and obtain the optimal conduction velocity (CV) in the PKN, and an average LAT error. The simulated activation sequence using the estimated PKN together with estimated CVs for tissue and Purkinje in a exemplary patient, provided a good match between simulated and real ECG, validating the PKN sequence of activation.

5.2 Material and methods

The study has been conducted with data from a cohort of 13 patients. In addition, a series of synthetic cases have also been generated to be able to extract quantitative error measurements. Following, we describe the characteristics of the population and the algorithms proposed to estimate the PKN from EAMs.

5.2.1 Patient Data

A set of 11 anonymized EAMs (10 men and 1 women, between 16 and 63 years old) was provided by Bordeaux University Hospital using CARTO 3 system (Biosense Webster, Inc., Diamond Bar, CA, USA), and different catheters, namely NaviStar ThermoCool ablation catheter and PentAray. Patients had an indication of idiopathic VF or syncope, and different types of substrate. Two additional EAM studies were included from a previous study [93], where MRI data was also available so the detailed anatomy of the endocardium could be reconstructed, and the EAM data fitted to it (see Figure 5.1 (c)). For every patient three studies were acquired in sinus rhythm: a map of the LV endocardium, a map of the RV endocardium and a map of the epicardium. Five patients benefited from high density endocardial mapping with a decapolar catheter to map the endocardium of both the RV and the LV.

Table 5.1 summarizes the electrophysiological studies acquired. Columns labeled as 'LV Pts' and 'RV Pts' show the final number of EAM points available after analyzing and filtering the data with respect to the total number of EAM points acquired in each case. The duration of the QRS complex is also provided in ms (QRSd). Patients P2 and P6 showed a nonspecific

intraventricular conduction delay (NICD). Patient P13 was mapped twice in the same intervention, thus for that patient we have the studies P13A and P13B.

Study	Catheter	LV Pts	RV Pts	Age	Sex	Substrate	QRSd
P1	Pentaray	229/860	276/810	50	M	HCM	110
P2	Pentaray	230/1460	371/1523	57	M	Laminopathy	102
P3	Navistar	174/691	165/744	34	M	Idiopathic VF	91
P4	Navistar	115/491	161/539	58	M	Idiopathic VF	120
P5	Navistar	177/514	190/532	18	M	Idiopathic VF	90
P6	Pentaray	191/1224	313/1494	63	M	Idiopathic VF	138
P7	Navistar	75/100	115/189	16	M	Idiopathic VF	102
P8	Pentaray	284/1044	345/792	23	F	Idiopathic VF	102
P9	Pentaray	320/874	387/1064	26	M	Idiopathic VF	102
P10	Navistar	92/174	78/169	51	M	Idiopathic VF	96
P11	Navistar	179/372	92/215	41	M	Brugada	120
P12	Navistar	219/315	73/78	58	M	Scar-related VT	105
P13A	Navistar	118/140	159/179	53	M	Idiopathic VT	104
P13B	Navistar	151/198	177/188	53	M	Idiopathic VT	104

Table 5.1: Description of EAM data acquired. QRSd stands for QRS duration in ECG.

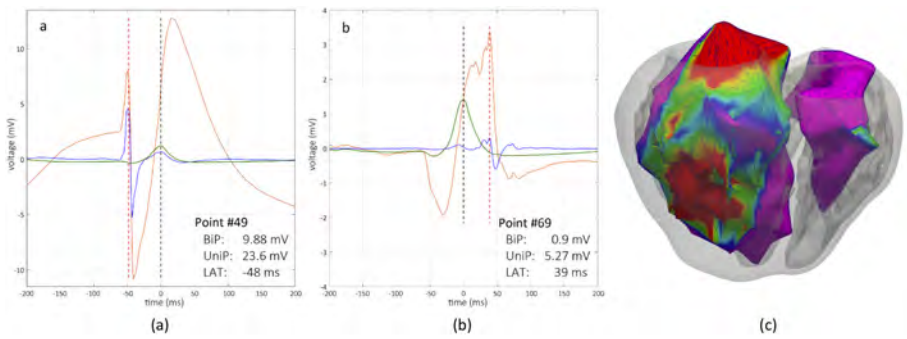

Figure 5.1: Example of EAM data for patient P12. (a)-(b) Electrograms recorded at points on the endocardium. Plots correspond to the ECG precordial lead V5 (green), distal unipolar EGM (M1) (orange) and distal bipolar EGM (M1-M2) (blue), showing 200 ms prior and after the R-wave peak in V5 lead (reference point for LAT measurement). Dashed vertical lines represent the R-wave peak automatically detected by EAM system (black) and the estimated time for tissue activation (red). (c) Fitting of LV and RV endocardial EAM to the corresponding patient MRI segmentation.

5.2.2 EAM processing

For each EAM, first, we filtered some of the points acquired based on voltage, local activation time (LAT) and distance to the EAM mesh. In particular, sample points with a bipolar peak-to-peak amplitude below 1.5 mV or with a LAT outside the range [-200, 200] ms, or more than 7 mm away from the endocardial wall were discarded. Note that, since the Pentaray catheter consists of five soft, flexible branches some of the leads can be away from the endocardial wall during the recording, which can be detected and removed using the filters described.

After the EP study, LAT annotations of the EAMs were automatically determined by the Confidense module of CARTO 3 System. However, a visual inspection of the EAMs showed spatio-temporal discrepancies among LATs in many sampled points. Figure 5.2 (top row) show the original LAT maps obtained from several LV EAMs, projected to a 2D unitary disk. Large time gradients can be observed in most patients, without a clear sequence of activation, and large delays between close areas, where there is no underlying substrate that can explain them.

Therefore, we carried out a re-annotation of the LATs, using a tailor-made Matlab code that, for each acquired point, searches the deflection on the distal bipolar signal (M1-M2) closest to the point of maximum negative slope on the distal unipolar signal (M1). Figure 5.1 (a) and (b) show an example of two electrograms recorded from patient P12. Green line corresponds to the ECG precordial lead V5 signal, which is used as a time reference (dashed black line on R-wave peak) to obtain the relative LAT. Dashed red line corresponds to the final LAT annotation. Note that after the re-annotation, those samples that do not show a good spatio-temporal correspondence with its closest neighbours will be discarded or not considered by the PMJ estimation algorithm, although they will still be used to calculate activation errors. The final numbers of curated samples for each patient are summarized in Table 5.1.

Figure 5.2 (second row) shows the resulting LV EAMs in 5 patients after data was filtered and re-annotated. After the re-annotation of the samples, a linear interpolation was performed to obtain the LAT on every point of the 3D mesh. For visualization purposes, the original EAM and the re-annotated EAM (Re-EAM) LAT maps were projected into a unitary 2D disk using a quasi-conformal projection (QCM) as in [94]. In particular, we used the conformal energy minimization (CEM) algorithm [95], based on

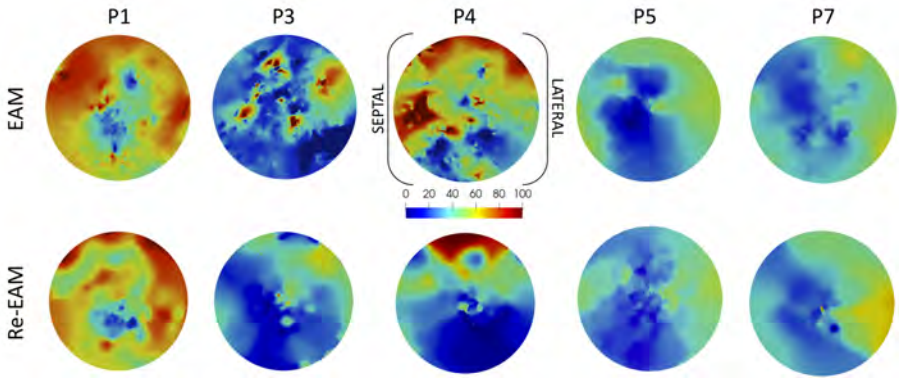

Figure 5.2: LV original EAMs and re-annotated EAM, projected into a 2D unitary disk. A set of 5 EAMs, (top) as they are obtained from the system, and (below) after applying filters, and re-annotating the local activation maps. After the re-annotation, the data was linearly interpolated on the 3D mesh, and projected using a quasi-conformal transformation, into a disk. Colorbar shows the local activation time from blue (t=0ms), to red (t=100ms).

discrete Laplace-Beltrami operator. This representation is very convenient to compare data from different LV geometries in a common reference space. As can be observed, the sequence of activation (early to late regions) is preserved, however there are large differences between the LAT maps locally due to previous errors in annotation. In all cases the postero-basal and lateral regions (orange to red area) were the last to activate, whereas the antero-apical region was the earliest (bluish areas).

5.2.3 Synthetic data

To evaluate the PKN estimation algorithm, we need scenarios in which ground truth data is known, i.e., on which the actual location of the PMJs, PKN and the associated activation pattern are known. Therefore, we built a set of synthetic PKNs on a generic LV endocardium, reconstructed from a MRI sequence, using the stochastic method described in [7]. The properties of the PKNs are summarized in Table 5.2.

The proposed PKN estimation algorithm is divided into two stages, the estimation of the PMJs and the estimation of the PKN from those estimated PMJs. Thus, we set up two different types of experiments to evaluate the performance of the PKN estimation. Based on the set of synthetic EAMs, first we evaluated the PKN estimation alone. To do this, we used the actual

Scenario				TAT (ms)	
Name	# PMJ	# PMJ/Seg	# Br	PKN	ENDO
PK1	1224	76.5 ± 0.7	2650	56.3	78.3
PK2	831	51.9 ± 1.1	1908	78.2	110.4
PK3	442	27.6 ± 0.6	948	64.2	86.5
PK4	362	22.6 ± 0.7	830	63.5	86.1
PK5	206	14.7 ± 0.6	298	67.7	89.7

Table 5.2: Information about five synthetic PKN. Column *Name* identifies the scenario, *PMJ* represents the number of PMJs in the scenario, *Density* is the average and standard deviation of the number of PMJs per segment (17 AHA segment division), *TAT PKN* is the total activation time of the Purkinje Network, *TAT ENDO* is the total activation time for the whole surface/ventricle.

PMJ locations and LATs, and estimated the corresponding PKNs, which were subsequently compared with the original conduction system. In the second set of experiments, for each PKN we simulated the corresponding His-Purkinje activation sequence for the endocardium, and following we sampled the endocardial tissue randomly at a number of locations (1000 samples), mimicking a virtual EAM. Once we had the actual LAT on the measurement points, we added a Gaussian error to the LAT values to emulate measurement errors, or wrongly annotated samples. This set of synthetic LATs was used as the input of our algorithm that first estimates a set of PMJs and, then, the PKN associated to these estimated PMJs.

Since we have all the information for these synthetic cases, we can conduct a quantitative assessment of the estimated PKNs. We have considered several measures of quality, summarized in Tables 5.3 and 5.4: the number of PMJs that have been successfully connected to the synthetic tree (error $\epsilon_{max} <$ threshold); Δ_{PMJ}, the mean absolute error of the LAT at PMJs $\mathbf{s}_i$, i.e., difference between estimated LAT at PMJ and the PKN LAT resulting from the propagation from the His Bundle to the PMJs through the estimated PKN, given a CV, in ms; the average distance from the estimated branches to the real branches per branch subsegment; Δ_{EAM}, the mean absolute error at EAM obtained as the difference between sampled value and value calculated from a simulation triggered from the estimated PKN.

5.2.4 Estimation of the PMJs

The proposed method starts with the estimation of the PMJs from an EAM. This step is done using an adapted version of the algorithm proposed in [92],

and described in Chapter 4. Basically, the new version requires certain filters to adjust the EAM data before it is processed. In that method, the endocardial domain is discretized by means of an homogeneous simplicial 2-complex in a three-dimensional space, Ω. The EAM either synthetic or acquired during an intervention is defined by a set $\mathcal{P}$ of measurement points. All these points belong to the set $\mathcal{V}$ of the vertices of Ω.

The procedure takes the location and LAT, $(\mathbf{p}_i, t_i)$ of the points in $\mathcal{P}$, to generate a set of points $\hat{\mathcal{S}}$ that are compatible with the observed activation times. The set $\mathcal{V}$ is traversed to evaluate if each vertex is a feasible activation point. By means of a hypothesis contrast, if a given vertex can be considered a PMJ, then a new candidate $\hat{\mathbf{s}}_i$ is added to $\hat{\mathcal{S}}$. After the generation of the set $\hat{\mathcal{S}}$ of candidate PMJs, all the $\hat{\mathbf{s}}_i$ are evaluated to determine their quality. By means of a new hypothesis contrast, we assess if the observed error in the points, $\mathcal{P}$, activated by $\hat{\mathbf{s}}_i$ is compatible with the distribution of the measurement error. This distribution can be that of the measurement process in clinical data or the injected Gaussian error in the synthetic cases. In the cases that lead to a very unlikely set of observed LAT, the associated points in $\mathcal{P}$ are removed, and the LAT of the measurement points is re-estimated. In general, we have observed that the cases that correspond to activation sequences with heterogeneous or non-smooth electrical propagation require a more aggressive refinement process, although errors below the measurement error values have been achieved in all cases. Note that, the set of PMJs is estimated for a range of predefined tissue conduction velocities (CVs), from 0.4 to 0.9 m/s. Finally, after testing all the CVs, the estimated set of PMJs with less average error at the sampling points, Δ_{EAM}, is the one kept for the next stage.

5.2.5 Estimation of PKN

The goal of the PKNs estimation algorithm is to find a PKN branching configuration that is able to reach all the estimated PMJs at the estimated LATs, with the minimum number of branches. We start by considering the set of estimated PMJs that were obtained in the previous step, $\hat{\mathcal{S}} = \{\hat{\mathbf{s}}_1, ..., \hat{\mathbf{s}}_n\} \subset \mathcal{V} \times \mathcal{R}^+$. As in the previous chapters, for each PMJ $\hat{\mathbf{s}}_i = (\mathbf{x}_i, \tau_i)$, the point $\mathbf{x}_i \in \Omega$ will be called the location and $\tau \in \mathcal{R}^+$ the estimated LAT at the PMJ. Without loss of generality, we will assume that PMJs are in ascending order of LAT, that is, $i \leq j \Rightarrow \tau_i \leq \tau_j$. We will also consider, Ξ, a connected simplicial 1-complex to represent the branches that form the PKN. Each vertex or node in Ξ will have an associated LAT, that

corresponds to its activation time according to the PKN generated and the CV through the PKN. The estimated PKN, will have the constraint that all the vertices of Ξ will be in a vertex or an edge of Ω, and all the edges of Ξ will coincide with an edge of Ω or will be contained in one of its faces. Moreover, the terminal vertices of Ξ have to be locations of the estimated PMJs.

We build the estimated PKN in an iterative fashion. An initial branch Ξ^0, corresponding to the His bundle and left bundle branch (LBB), is built before the algorithm generates any further branch. The initial branch starts always from a location determined by the user and expands to the apex through the septal wall following the shortest path, which is obtained by calculating the geodesic path between both points. Then, we process the PMJs in order of LAT, starting by the earliest one. Therefore, we start building the PKN from the region closer to the LBB, which is expected to show smaller LAT errors due to the shorter path from the Atrioventricular Node (AVN).

After step i, we have processed $i-1$ PMJs in $\hat{\mathcal{S}}$ and have built an estimated tree Ξ^{i-1} that connects them. We pick $\hat{\mathbf{s}}_i$ and solve the Eikonal problem on Ω starting from $\hat{\mathbf{s}}_i$ to obtain the distance from the estimated PMJ to all the vertices on Ξ^{i-1}. Then, we try to connect the PMJ $\hat{\mathbf{s}}_i$ with Ξ^i using a geodesic that ends at a point $\xi_i \in \Xi^{i-1}$. The connection point is chosen as the solution of the optimization problem

$$\xi_i = \underset{\xi_i \in \Xi^{i-1}}{\operatorname{argmin}} \left\{ t_i - \left(t(\xi_i) + \frac{|\xi_i - \mathbf{x}_i|_\Omega}{v} \right) \right\}, \tag{5.1}$$

$$s.t. \;\; \operatorname{path}_\Omega(\xi_i, \mathbf{x}_i) \cap \Xi^{i-1} = \emptyset, \tag{5.2}$$

where $|\cdot|_\Omega$ is the distance on Ω defined in Chapter 4, $\operatorname{path}_\Omega(\xi_i, \mathbf{x}_i)$ is the piece-wise linear curve that connects x_i with ξ_i built with the Fast Marching algorithm to compute the distance, and v is the CV in the PKN. With the constraint on the path, we exclude new branches that intersect the PKN created so far. In summary, we are trying to connect the estimated PMJ to the current PKN at a location so that the LAT at the PMJ matches the estimated one, provided a CV, v, inside the PKN. Only solutions with an error value, $\Delta_{PMJ} < \epsilon_n$ (user-defined threshold at iteration 'n'), will generate a new branch for the PKN in each iteration. In cases in which the residual in Eq. 5.1 is above the threshold, the candidate $\hat{\mathbf{s}}_i$ is not connected. Once the iteration ends with the last $\hat{\mathbf{s}}_i$, the process is restarted trying to connect the disregarded PMJs to the estimated PKN, using a larger

threshold. The algorithm stops when all the PMJs have been connected to Ξ or when the error threshold in the unconnected PMJs reaches a predefined bound.

5.2.6 Biophysical Simulations

For patient P12, where the heart and torso MRI, as well as EAMs were available, a detailed computational model for biophysical simulations was built as described in [93] (see Figure 5.1 (c)). Therefore, for this case, we estimated the PKN directly on the segmented 3D mesh, which included trabeculae, instead of using the coarse EAM mesh. In summary, the volumetric mesh was composed of 4 million nodes, and 3.7 million hexahedral elements (resolution of 0.4 mm). The model includes a detailed endocardium, since the most important trabeculations and papillary muscles were segmented. The resulting finite element model was labeled to differentiate, LV and RV, as well as endocardium (17% wall thickness), mid-myocardium (41% wall thickness) and epicardium (42% wall thickness) to take into account cell heterogeneity. Fiber orientation was included in the model by using a rule-based model [96] adapted to Streeter's descriptions [56]. The heart model was fit to a full torso model, that included the most important organs, and was meshed with tetrahedral elements. Electrical propagation through the torso model was considered isotropic. The different conductivity values assigned to each organ were, lungs (0.039 S/m), blood (0.700 S/m), liver (0.028 S/m), bones (0.020 S/m) and the rest of the torso, conformed mainly by flesh and fat (0.239 S/m) [97]. To register the three available EAMs (LV, RV and epicardium) to our 3D ventricular model, we apply a rigid transformation, using the ICP (iterative closest point) algorithm.

Cellular electrophysiology was modelled using the human ventricular ionic model by ten Tusscher et al. [98] for the myocardium and Stewart et al. model for Purkinje [99]. Electrical propagation in tissue was modelled by solving the monodomain formulation with ELVIRA software [100]. Time step was set to 0.02 ms.

CVs were adjusted to each ventricle by tuning the longitudinal and traversal conductivities, considering axi-symmetric anisotropy, and the CVs estimated for tissue and the PKN during the PKN estimation procedure.

5.3 Results

5.3.1 Estimation of PKN from synthetic data

For the five PK synthetic scenarios, we obtained the set of estimated PMJs, and the set of estimated PKNs. For the estimation of PKNs, we compared the results using actual (Table 5.3) and estimated PMJs (Table 5.4) as input to the algorithm.

As it can be observed, when using the actual PMJs (location and LAT taken directly from the model) the errors, Δ_{PMJs} and Δ_{EAM}, are smaller, and the PKN structure is reproduced more accurately (see Figures 5.3 and 5.4 first row). When all the PMJs are available, the resulting PKN can easily follow the branching pattern of the original underlying PKN, with the estimated branches overlapping the actual branches in most cases (distances between actual and estimated PKN around 0 mm, blue branches in Figure 5.3 (d)). In Figure 5.4 it is shown, using single headed arrows, the location of the main PKN branches that almost match between actual (yellow branches) and estimated PKN (red branches). As expected, when Gaussian errors were introduced in the samples, the LAT times changed and the corresponding estimated PKN started to diverge from the original PKN. The effect is clear in Figure 5.4, where estimated branches are further from the original than same cases with less LAT error. The effect of the sample error it is not linear with respect to the distance, as can be seen in Table 5.4, since the morphology and complexity of the PKN also plays an important role. A complete view of real and estimate PKN using actual PMJs is displayed in Appendix A.2, Figure A.7.

When using the actual PMJs as input, Δ_{PMJs}, i.e. the difference in LAT at PMJs (between real and obtained through the PKN) is, on average, below 0.85 ms for all scenarios, as it is Δ_{EAM}, the average errors after propagating the signal to all mesh points. The average distance between tree segments is smaller than 1 mm (Table 5.3), due to the close match between real and estimated PKNs in most tree sections. In addition, around 95% of the PMJs could be connected to the tree with an error below $\epsilon_{max} < 4.0ms$. Not all PMJs could be connected due to a restriction imposed on the PKN with respect to overlapping branches. It is noteworthy, that the number of PMJs in the model affected both errors Δ_{PMJs} and Δ_{EAM}. When models show a large density of PMJs (PK1, 1224 PMJs), Δ_{PMJs} and Δ_{EAM} where slightly smaller than less crowded models (PK5, 206 PMJs).

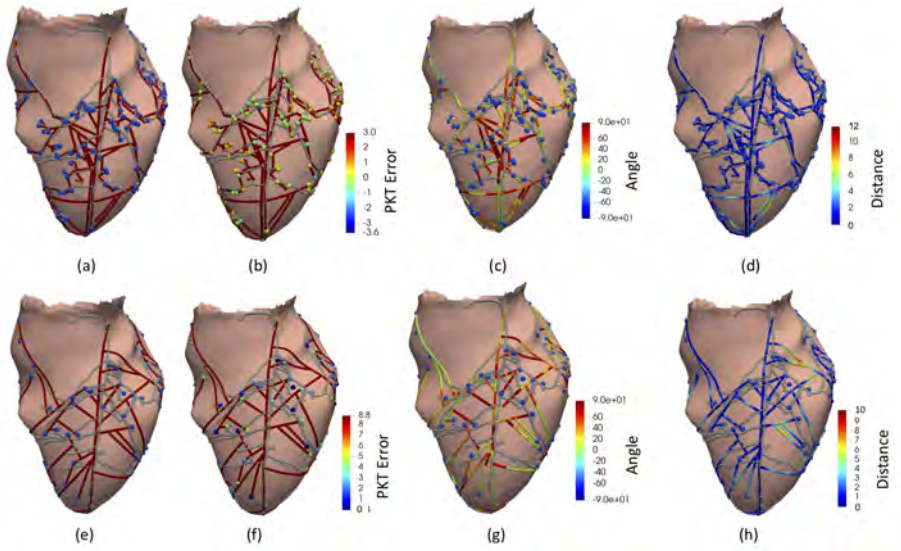

Figure 5.3: Graphical results for estimation of synthetic model PK3 with Gaussian error $\sigma = 0.5$. The original PKN is depicted as a tubular structure in grey color, while PMJs are represented with spheres. First row corresponds to estimated PKNs using the real PMJs, while second row are the PKN estimated from estimated PMJs (also included). (a) and (e) show the real (gray) and estimated (red) PKN structure, together with and the location of the (a) real PMJs, and (e) estimated PMJs. PMJs in (b) and (f) are color coded to show the error at PMJs, when the estimated PKN is used. PKN in (c) and (g) show the differences in angle (degrees) between the real and the estimated PKN branches, while (d) and (h) show the distance (mm) between the elements of the real and the estimated PKN.

When the estimated PMJs were used to build the PKN (see Figure 5.3 second row, and Figure 5.4 second and third rows, and Table 5.4), the CV in the PKN had to be estimated. Note that, for simplicity, in the simulations we used a reference CV of 1.0 m/s in the PKN. In scenarios with estimated PMJs, the percentage of PMJs available to build the PKN decreased considerably. We used 1000 EAM samples to estimate the PMJs. In dense scenarios such as PK1 (1224 PMJs), we estimated 9.3% of PMJs when the Gaussian error introduced was $\sigma = 0.5$, and 5.4% when $\sigma = 2.5$, while in coarser models such as PK5, we estimated 40.3% when the error was $\sigma = 0.5$, and 27.7% when $\sigma = 2.5$. Since we only could estimate a subset of the actual PMJs, the algorithm tends to overestimate the CV, as can be seen in Table 5.4 (CV), where most cases have an optimal value above 1.0 m/s. Having less PMJs estimated, the resulting PKN is simpler (less branches), and the estimated CV is larger. In Table 5.4 the number of

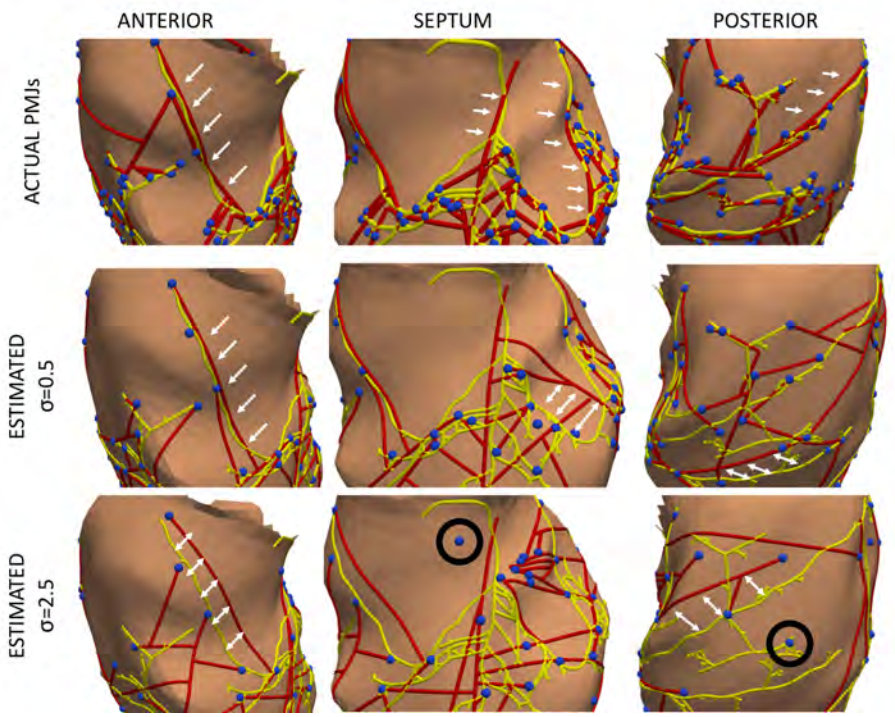

Figure 5.4: Detailed comparison of PK3 with different Gausian errors in the samples. PKNs are rendered with tubes, yellow for the original, and red for the estimated. Blue spheres are the PMJs, either actual ones or estimated (for error $\sigma = 0.5$ and $\sigma = 2.5$). Single headed white arrows show perfect fit between original and estimated PKN, while double headed arrows show the displacement between them. Black circles point out PMJs not connected to the tree due to temporal errors.

branches of each estimated PKN is summarized in column labeled '# Br'. Using the proposed methodology the number of branches in an estimated PKN is always the number of PMJs plus one branch (bundle branch).

The percentage of estimated PMJs that can be successfully connected to the PKN decreases as we increase σ from 0.5 to 2.5, due to errors in location and LAT of estimated PMJs (note that Gaussian error was inserted in the samples as described in [92] and Chapter 4). Figure 5.4 shows, as an example, PMJs (within a black circle) that could not be connected to the tree. The PMJ showed in the septal view was correctly discarded, since in that region there were no PMJs, and the PMJ position was not compatible with its estimated LAT. However, the PMJ shown in the posterior view was properly estimated and overlapped an area of 5 real PMJs, but due to the

complex branching pattern in the original PKN necessary to reach that area, the simplified estimated PKN could not reach that region at the estimated LAT, and could not connect the PMJ with a LAT error $\epsilon_{max} < 4.0ms$. In general, the percentage of estimated PMJs that are connected to the PKN with $\epsilon_{max} < 4ms$ is around 75%. Errors at PMJs, Δ_{PMJs}, are still below $1ms$ in all scenarios, however, the average error across the mesh, Δ_{EAM}, (measured at the 1000 sampled EAM points) increases due to two main reasons: i) the underestimation in the overall number of PMJs, which is around 10% of the real ones; and ii) the error in the LAT of the estimated PMJs. The same explanation applies to the increase in distance error, since due to the low number of PMJs and branches in the estimated PKN, the distance to the real PKN is larger. In summary, Δ_{EAM} is below $3ms$, even when $\sigma = 2.5$, in all scenarios except PK1, which has a very large number of PMJs.

Name	PMJs	ϵ <5ms	ϵ <1ms	Δ_{PMJs}	# Br	Distance error	Δ_{EAM}
PK1	1224	96.32%	84.23%	0.69 ± 0.6 ms	968	0.87 ± 1.32 mm	0.52 ± 0.3 ms
PK2	831	94.83%	79.42%	0.72 ± 0.6 ms	591	1.76 ± 2.61 mm	0.63 ± 0.5 ms
PK3	442	96.83%	88.20%	0.65 ± 0.6 ms	369	1.19 ± 1.39 mm	0.63 ± 0.5 ms
PK4	362	95.86%	78.45%	0.70 ± 0.6 ms	300	1.53 ± 1.58 mm	0.65 ± 0.5 ms
PK5	206	95.63%	80.58%	0.81 ± 0.7 ms	186	1.89 ± 2.06 mm	0.72 ± 0.8 ms

Table 5.3: Estimation of the PKN directly from the real PMJs without error.

Name	σ	#PMJs	CV	ϵ <4ms	ϵ <1ms	Δ_{PMJs}	# Br	Distance error	Δ_{EAM}
PK1	0.5	114	1.1	76.32%	62.28%	0.79 ± 0.9ms	86	2.20 ± 2.7mm	1.67 ± 1.8ms
PK1	2.5	67	1.2	50.75%	41.79%	0.96 ± 0.9ms	35	2.46 ± 3.1mm	4.48 ± 4.5ms
PK2	0.5	95	1.2	77.89%	60.00%	0.66 ± 0.7ms	74	2.11 ± 2.4mm	1.20 ± 1.4ms
PK2	2.5	66	1.2	63.64%	46.97%	0.88 ± 0.9ms	43	4.94 ± 5.1mm	3.24 ± 2.6ms
PK3	0.5	111	1.0	81.98%	63.96%	0.76 ± 0.8ms	90	1.92 ± 1.8mm	1.40 ± 1.4ms
PK3	2.5	68	1.3	69.12%	58.82%	0.72 ± 0.8ms	46	2.81 ± 1.3mm	2.70 ± 2.9ms
PK4	0.5	99	1.0	85.86%	69.70%	0.72 ± 0.6ms	86	2.17 ± 2.1mm	1.18 ± 1.2ms
PK4	2.5	68	1.1	75.00%	60.29%	0.71 ± 0.7ms	52	2.35 ± 2.0mm	2.54 ± 2.6ms
PK5	0.5	83	1.1	79.52%	57.83%	0.72 ± 0.5ms	67	3.09 ± 3.6mm	1.38 ± 1.6ms
PK5	2.5	57	1.3	78.95%	57.89%	0.83 ± 0.9ms	46	2.40 ± 2.2mm	2.37 ± 1.9ms

Table 5.4: Estimation of the PKN from estimated PMJs and error $\sigma = 0.5ms$. CVs (conduction velocities) in m/s. # Br stands for number of branches in the PKN. ϵ_{max} < threshold, percentage of estimated PMJs connected to the PKN below a threshold error; Δ_{PMJs}: Average time error between estimated time at PMJs and time at which the wavefront arrives through the PKN; Δ_{EAM}: Average time error between LAT at endocardial samples and time at which activation wavefront arrives using the estimated PKN.

EAM		PMJ Estimation						PKN Estimation		
Study	#Pts	Link	CV_T	CV_{PK}	TAT_{PMJs}	#PMJs	Δ_{EAM}	ϵ <5ms	Δ_{PMJs}	Δ_{EAM}
P1 LV	229	79%	0.5	1.7	56.7 ms	31	7.66 ms	30 (97%)	0.69 ± 0.7 ms	8.0 ms
P1 RV	276	69%	0.4	2.1	54.4 ms	34	15.96 ms	32 (94%)	1.30 ± 1.3 ms	16.0 ms
P2 LV	230	85%	0.6	1.7	59.2 ms	37	5.70 ms	32 (86%)	0.73 ± 0.9 ms	7.2 ms
P2 RV	371	88%	0.6	1.9	48.7 ms	38	6.65 ms	35 (92%)	0.70 ± 1.0 ms	6.9 ms
P3 LV	174	79%	0.8	1.7	38.0 ms	23	6.25 ms	20 (88%)	1.18 ± 1.4 ms	6.9 ms
P3 RV	165	92%	0.9	2.3	37.1 ms	16	4.76 ms	13 (81%)	0.79 ± 1.2 ms	5.2 ms
P4 LV	115	76%	0.8	1.7	57.6 ms	11	8.05 ms	9 (82%)	0.99 ± 1.3 ms	8.3 ms
P4 RV	161	76%	0.6	1.9	44.1 ms	19	11.02 ms	15 (79%)	0.63 ± 0.5 ms	13.6 ms
P5 LV	177	84%	0.9	1.7	28.0 ms	19	4.10 ms	18 (95%)	0.69 ± 0.6 ms	4.4 ms
P5 RV	190	93%	0.8	2.1	48.8 ms	20	5.60 ms	17 (85%)	0.67 ± 0.8 ms	5.8 ms
P6 LV	191	76%	0.4	1.7	93.4 ms	28	8.34 ms	23 (82%)	0.93 ± 1.2 ms	9.5 ms
P6 RV	313	63%	0.4	1.7	66.4 ms	39	20.20 ms	31 (79%)	0.68 ± 0.7 ms	21.0 ms
P7 LV	75	87%	0.8	2.1	36.48 ms	12	5.43 ms	12 (100%)	1.06 ± 1.5 ms	5.9 ms
P7 RV	115	64%	0.7	2.1	60.7 ms	17	10.90 ms	13 (76%)	1.06 ± 1.5 ms	12.1 ms
P8 LV	284	89%	0.6	1.9	42.8 ms	38	5.63 ms	32 (84%)	1.00 ± 1.1 ms	6.1 ms
P8 RV	345	89%	0.6	2.5	44.4 ms	51	3.96 ms	47 (92%)	1.02 ± 1.0 ms	4.4 ms
P9 LV	320	86%	0.7	2.1	32.1 ms	39	3.91 ms	34 (87%)	1.06 ± 1.1 ms	4.5 ms
P9 RV	387	91%	0.7	1.7	36.5 ms	43	3.61 ms	38 (88%)	0.87 ± 1.1 ms	4.7 ms
P10 LV	92	66%	0.8	1.7	24.2 ms	13	13.83 ms	11 (85%)	0.89 ± 1.0 ms	15.2 ms
P10 RV	78	88%	0.6	1.9	50.6 ms	13	7.56 ms	11 (85%)	0.68 ± 1.0 ms	9.4 ms

EAM		PMJ Estimation						PKN Estimation		
Study	#Pts	Link	CV_T	CV_{PK}	TAT_{PMJs}	#PMJs	Δ_{EAM}	ϵ <5ms	Δ_{PMJs}	Δ_{EAM}
P11 LV	179	69%	0.4	1.9	91.7 ms	27	14.97 ms	25 (93%)	0.87 ± 1.1 ms	16.1 ms
P11 RV	92	66%	0.7	1.9	80.9 ms	12	7.92 ms	10 (83%)	0.69 ± 0.6 ms	9.9 ms
P12 LV	219	72%	0.5	1.9	108.8 ms	37	6.42 ms	33 (89%)	0.25 ± 0.5 ms	6.7 ms
P12 RV	73	81%	0.4	1.9	25.2 ms	17	5.29 ms	16 (94%)	0.39 ± 0.8 ms	5.5 ms
P13A LV	118	75%	0.9	2.3	20.5 ms	17	5.61 ms	16 (94%)	0.26 ± 0.3 ms	5.9 ms
P13A RV	159	69%	0.6	2.3	32.4 ms	22	9.32 ms	19 (86%)	0.57 ± 1.0 ms	10.9 ms
P13B LV	151	72%	0.8	2.3	29.9 ms	21	6.39 ms	19 (90%)	0.36 ± 0.7 ms	6.4 ms
P13B RV	177	62%	0.7	2.3	32.8 ms	14	12.51 ms	13 (93%)	0.33 ± 0.6 ms	13.2 ms
AVG	195	78%	0.7	1.96	47.8 ms	25	8.13 ms	22 (88%)	0.76 ± 0.9 ms	8.9 ms
AVG>70	203	83%	0.7	1.95	46.9 ms	27	6.10 ms	24 (89%)	0.75 ± 0.9 ms	6.8 ms

Table 5.5: Estimation of the PKN from EAMs. #Pts: Points of EAM after filtering; Link: Percentage of Pts consistent with estimated PMJs ; CVs (conduction velocities) in m/s for tissue (T) and Purkinje (PK). TAT: Total activation time of the PMJs; #PMJs: Estimated PMJs; and ϵ_{max} < threshold, number of estimated PMJs connected to the PKN below a threshold error; AVG: Average results; AVG>70: Average for cases with Link over 70%.

5.3.2 Estimation of PKN from EAMs

A set of EAMs acquired from patients (summarized in Table 5.1) was used to estimate the corresponding PKNs. First, the EAMs were analyzed to detect problems with the LAT maps. It can be clearly seen in Figure 5.2 (top row) the existence of large gradients in the patient's LAT maps, which are mainly due to wrongly annotated LATs in the EAM. After the re-annotation (Figure 5.2 bottom row), the LAT maps showed much smoother transitions, and more physiological patterns of activation. Once the data was filtered and re-annotated, we could estimate the PMJs, using more reliable data at the cost of loosing many samples. Table 5.5, column '#Pts' indicates the final number of points available in each EAM after filtering, which was on average 195.

For the estimation of PMJs, an optimal CV for tissue (CV_T) has to be estimated for each case. Therefore, the estimation was carried out considering a range of CV_T between 0.4 m/s and 0.9 m/s, which is within a physiological range. For each CV_T, we obtained an estimation of the total number of PMJs, the number of EAM samples that support each of those PMJs (and their correlation), and the error Δ_{EAM} after propagating from the estimated PMJs to the endocardial samples. The best results were used as an input to estimate the PKN.

The number of PMJs obtained from the real cases ranged from 11 to 51, which was expected mainly due to the low number of endocardial samples finally used to estimate them (between 73 and 387 samples), the errors in the LAT maps and the sample location errors (a detailed geometry was not used in almost any case). The error Δ_{EAM} when directly activating from the PMJs (PKN structure not considered) ranged from $3.61ms$ to $20.20ms$, with an average of $8.13ms \pm 4.12$ ms. This error can be explained looking at the number of EAM samples that were compatible with any of the PMJs estimated, which is included in Table 5.5, column labeled as 'Link'. It is important to remark that during the estimation of the PMJs only a subset of the EAM samples actually produced PMJs for a given CV_T. i.e., the 'link' factor. In general, when less than 70% of the samples generates PMJs, LAT errors are large ($>$ 10 ms). This is explained by the fact that, once the propagation from PMJs is carried to the whole mesh, non-contributing EAM samples are not in agreement with the LATs, increasing the error. Therefore, the 'Link' is a measure of confidence in the PKN estimation, that can help assessing the accuracy together with the error Δ_{EAM}. There might be several reasons that explain small 'Link' numbers such as, wrongly

annotated samples, that make the map spatio-temporally incoherent, or tissue inhomogeneities that produce local changes in CV that affect the convergence of the inverse estimation. Attending only to estimated PMJs with a Link over 70%, the average error Δ_{PMJs} decreases to 6.10 ± 1.8 ms (Table 5.5 last row).

As with the synthetic PKNs, the CV in the PKN (CV_{PK}) had also to be estimated. The algorithm estimated PKNs for velocities in the range between 1.5 and 2.5 m/s on the best PMJ estimation solution, based on final average error Δ_{PMJs}. The final anatomy of the estimated PKN changes as a function of the CV_{PK}, since the sum of branch lengths has to shorten as we increase CV_{PK} for a given PMJ with a specific LAT. As can be observed in Figure 5.5, for a given set of estimated PMJs, using a $CV_{PK} = 1.7m/s$, branches in the septum branch out earlier than the case of $CV_{PK} = 2.3$ m/s. The arrival time at PMJs also changes, and therefore the LAT of the PMJs differs (within the allowed threshold), resulting in different errors and number of PMJs connected. For most of the cases, summarized in Table 5.5, the optimal CV_{PK} was between $1.7m/s$ and $2.1m/s$, with an average of 1.95 m/s, which resulted in more than 80% of PMJs connected and average errors Δ_{PMJs} under 1.3 ms (Table 5.5, column 'Δ_{PMJs}'). In Appendix A.2, Figures A.8, A.9, A.10, show the estimated PKN for patients P1 LV, P1 RV, and P2 RV, respectively.

For the PKN estimation, the maximum error allowed at a PMJ to connect a branch to it, was set to $\epsilon_{max} < 5ms$, to keep average errors under a reasonable threshold. The number of estimated PMJs connected to the PKNs was in average 88%. Since in most scenarios estimated PMJs included PMJs incorrectly estimated, we expected that the PKN algorithm filtered some of them, and therefore a 100% connection was not desirable. In fact, when more PMJs were connected to a PKN the average LAT error Δ_{PMJs} increased, which required a trade-off between PMJs connected and average LAT error. We choose to get the maximum number of PMJs connected, with a maximum average LAT error Δ_{PMJs} below 1.3 ms. As can be observed in Table 5.5, Δ_{PMJs} was in average 0.76 ± 0.9 ms.

Figure 5.6 shows a comparison of LV LAT maps for five patients, including the re-annotated EAMs used to estimate the PKN (first row), the PMJs (spheres) estimated and the LAT map obtained when simulating from the PMJs (second row), and the LAT map obtained when the activation was triggered from the estimated PKN (third row). As can be observed, the PMJ and PKN LAT maps are very similar, since most PMJs were connected

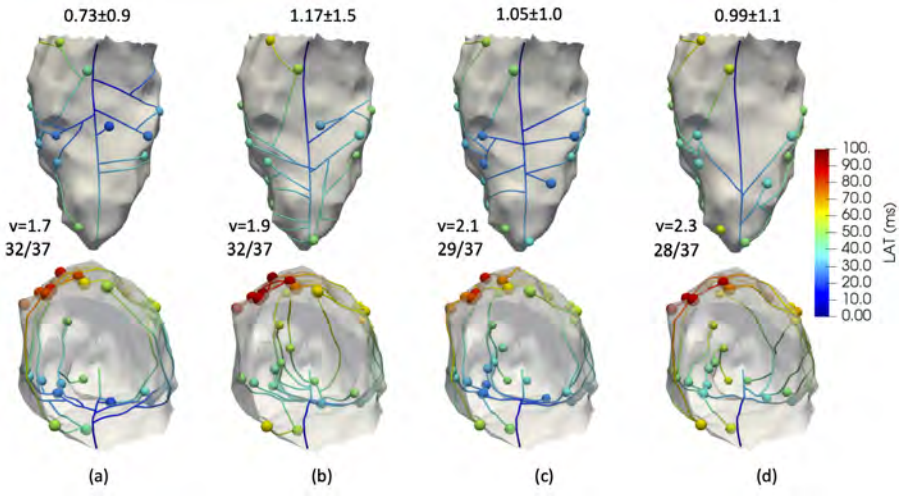

Figure 5.5: PKN Estimated from patient P2 LV EAM using different conduction velocities (CVs), from (a) 1.7 m/s to (d) 2.3 m/s. Colors correspond to the LATs. PMJs (spheres) together with Δ_{PMJs} and standard deviations (in ms) are included for each velocity, together with the PMJs connected ($\epsilon_{max} < 5ms$) out of 37 PMJs estimated.

to the corresponding PKN and the LAT errors Δ_{PMJs} were small (see Table 5.5, column 'Δ_{PMJs}'). However, there are differences with respect to the EAM, specially for the case of patient P1. EAM maps showed in the first row are obtained after re-annotating the LAT of the endocardial samples and interpolating the data. Therefore, it is important to take into account that the resulting interpolated LAT map is not exactly the real activation sequence of the patient, since the activation time range is bounded by the earliest and latest sample acquired. Moreover, a Gaussian kernel is used to interpolate the LATs, which introduces a smoothing effect that reduces the range of the LATs. Overall, the best results were obtained for P5 LV, P8 RV, and P9 (see see Table 5.5, column 'Δ_{EAMs}'). The reason for those improved results was a larger number of EAM samples (above 300 in most of them) together with a high Link factor ($> 84\%$). On the contrary, worst cases showed Link values around 63% and large errors. The number of PMJs estimated did not correlate with the error, although the best cases included more than 30 PMJs estimated, which is above the average (22 PMJs) in our study. There was an outlier, patient P6, that showed an error Δ_{EAMs} of 21.0 ms, which was really high compared with the rest of cases. That particular case corresponded to a case with NICD (QRSd 138 ms), which probably had some problems at the level of the PKN, or the

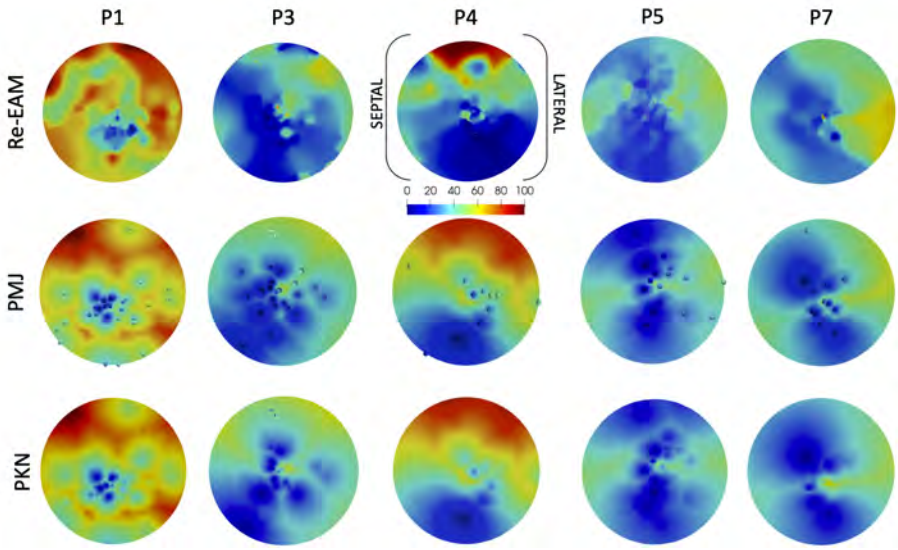

Figure 5.6: Comparison between projected LV LAT maps. Comparison for five patients of the LAT maps corresponding to i) EAM re-annotated and interpolated (first row), ii) Simulated LAT map from estimated PMJs (second row), iii) Simulated LAT map from estimated PKN (third row). Maps are color-coded from t=0 ms (bluish regions) to t=100 ms (redish regions).

myocardial tissue, which hamper the estimation that assumes homogeneous propagation on both media.

For the particular case of patient P12, the LATs annotated for each point in the EAM were manually corrected by an expert, and inconsistent samples removed. In addition, the endocardial anatomy was obtained from MRI, and the EAM was mapped on it. As a result, we observed that a larger proportion of PMJs could be estimated, compared to other cases with more samples. In addition, both the number of PMJs connected and the average errors were smaller.

For patient P13, we had two different EAM studies (P13A and P13B), which were used to obtain two different estimations of the PMJ set. As can be observed in Table 5.5 and Figure 5.7, the optimal CVs (2.3 m/s) in the PKN matched for both ventricles in both cases. The estimated PMJs for each study differs in the number of PMJs (e.g. LV (a) 17 vs (b) 21) and the location of some of them. When the PKN was estimated, the final number of PMJs was almost the same (LV (a) 16 vs (b) 19), and the sequence of activation show a similar pattern with respect to early a late activated

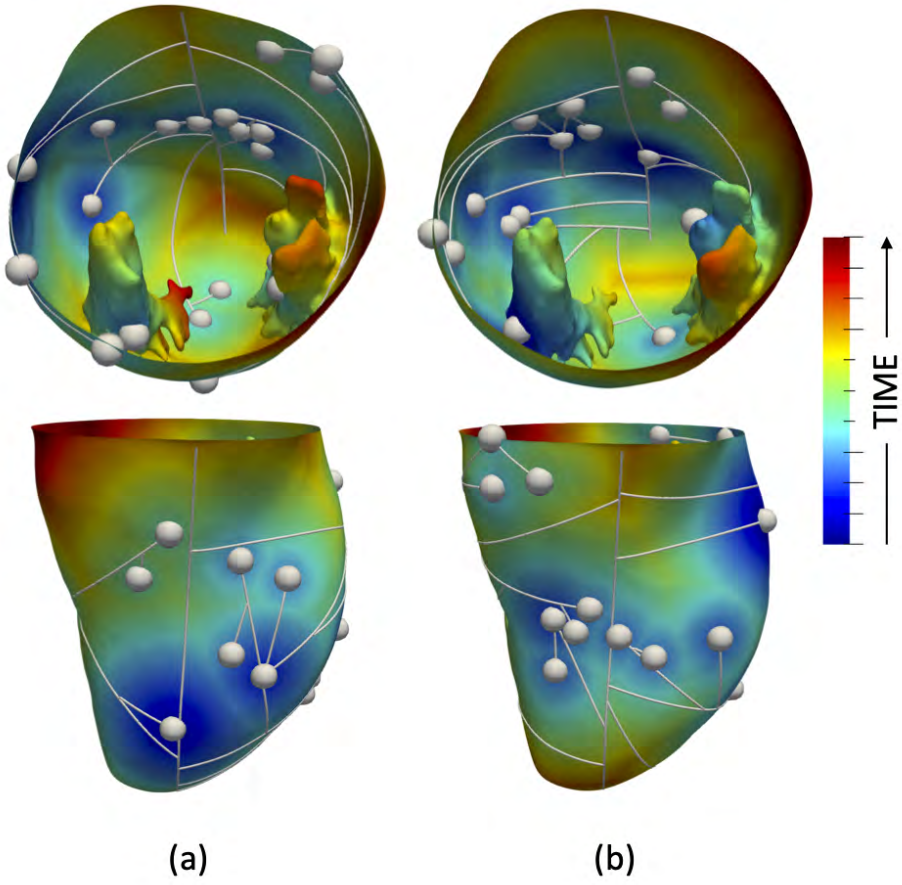

Figure 5.7: Comparison of PKNs estimated from two different EAM studies on the same patient. LATs (first row) and Error at PMJs (second row) for (a) study 1 (P13A), and (b) study 2 (P13B).

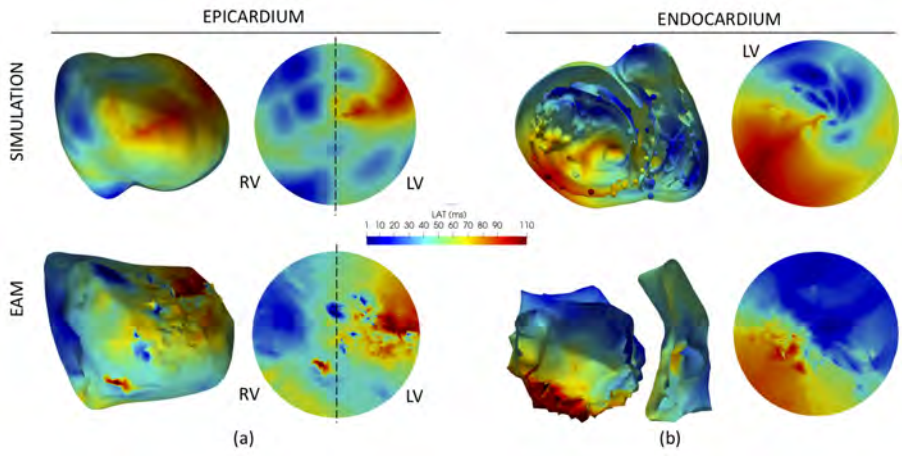

Figure 5.8: Comparison between Simulated LAT and EAM for P12. LATs obtained by simulating the patient P12, using the estimated PKN (upper-row), compared to patient EAM (bottom-row). (a) Epicardial LATs on the 3D mesh (left) and equivalent projected into a disk (right). (b) Endocardial LATs on the 3D mesh and projection of the LV into a disk.

regions. Nonetheless, we did not observe a perfect coincidence between the LAT maps, since the EAMs were not identical among them, despite they were recorded from the same patient.

5.3.3 ECG simulation

To further validate the PKN method, we performed full biventricular biophysical simulation for patient P12, were the volumetric finite element mesh was constructed. As can be observed in Figure 5.8, the EAM activation sequences in the epicardium (a) and the endocardium (b), were properly reproduced by the simulation, following the main patterns. The total activation times of EAM and simulation matched each other.

Finally, the extracellular potentials generated in the heart were propagated to the torso surface to obtain the ECG. Figure 5.9 (a) shows the clinical ECG recorded from the patient, while (b)-(d) correspond to simulations. Figure 5.9 (b) is the result of the activation triggered from the estimated PKN, in which can be appreciated that the polarity of all precordial leads is in agreement with the clinical data, as well as the timing and the evolution of the amplitude from V1 (the most negative) to V5 (the most positive). Figure

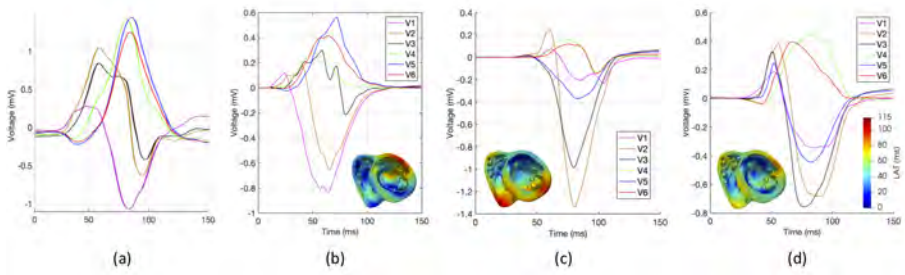

Figure 5.9: Comparison between real and simulated ECG of patient P12. (a) Clinical patient ECG recorded at precordial leads in sinus rhythm. (b) Simulated ECG using the estimated PKN. (c) Simulated ECG using discrete endocardial points to match Durrer's [26] activation sequence. (d) Simulated ECG using an stochastic PKN generated using L-systems [7].

5.9 (c) corresponds to a sequence of activation that mimicked Durrer's descriptions [26], and is commonly used in modelling papers, while Figure 5.9 (d) corresponds to a sequence of activation triggered from a stochastic PKN generated using the methodology described in [7, 60]. Both cases produce non-physiological ECGs, which differ from the patient's clinical recordings.

5.4 Discussion

In this chapter, we have presented a novel methodology to estimate a PKN for a given patient by estimating its PMJs and branching structure from an EAM. From the estimated model, it is possible to obtain information about the PMJ locations (early activated regions) as well as to reproduce the patient electrical sequence of activation using computer simulations. This result is important since it has been demonstrated the role of the Purkinje system in several types of cardiac arrhythmia, such as VT or idiopathic VF [30]. The PKN cannot be directly observed invivo and it is very complex to map with current clinical technology [23, 101]. That is one of the main reasons why having accurate computer models of the PKN to carry out biophysical simulations is so important. Clinically, a better knowledge of the PKN structure of a patient showing VT triggered from the PKN could help in the identification of ablation sites. Recently, it has been proposed the use of ablation for "De-Networking" of the Purkinje system in cases in which it has been implicated as a source of initiation of VF [102]. In those cases, having information about PKN structure is fundamental to plan the

ablation.

In the modeling literature the most common approach to build a PKN is either manually [61, 62] or by developing random networks based on fractals (L-systems) or following optimization criteria [60, 58, 91, 103, 104]. Some authors have chosen to segment the proximal sections of the PKN in animals such as dog [105] using Lugol's solution or calf ([7]) using Indian ink. Many computational studies simply neglect the PKN and focus on pathologies, where there is little involvement of the ventricular conduction system, such as scar-related VT [46, 75, 106, 93]. Having a more faithful PKN, able to reproduce the sequence of activation of a specific patient with an error of a few milliseconds, can help in virtual therapy planning and optimization of RFA or cardiac resynchronyzation therapy (CRT) [5].

By means of a simulation study, we have verified that the methodology presented is able to estimate the most relevant PMJs or early activated areas with small spatio-temporal errors. In addition, the main bundles of the PKN (anterior and posterior) could be properly reconstructed, and most of the PMJs (>80%) successfully connected to the estimated PKN considering physiological CVs in both tissue and PKN. In distal areas, where the branching pattern is complex, the morphology could not be reproduced, but only simplified representations of the PKN. It is important to remark that since branch intersections are not allowed by design, the resulting PKN is a tree instead of a closed network. Nonetheless, the estimated PKN can reproduce the sequence of activation observed in the EAM of the patient, avoiding the use of a random PKN with an arbitrary number of PMJs.

A few computational studies have also focused on the invivo estimation of a compatible PKN from EAMs [69, 70, 71]. For instance, in [69], a complex fractal-based PKN is built on the endocardium as a background network, and following PMJs are either moved, removed or added to the network to reduce the error Δ_{EAM}. Our minimal PKNs, estimated from the data, had less than 100 branches and 50 PMJs (see Table 5.5), while the fractal models in [69] had between 1500 and 2500 branches, and 200 to 250 PMJs, similar to our synthetic PKNs (see Table 5.2). Still, there is a remarkable difference in the optimal CV_{PK} obtained in our study that ranged between 1.7 and 2.1 m/s, compared to the 3.9 m/s obtained in [69], or 2.25 m/s used in [105]. It is important to point out that the average conduction velocity of $1.95 m/s$ estimated in the PKN was very stable between cases, and can be considered as a physiological parameter for the human PKN. We avoid to perform a CV over-fitting, that is, adapting locally the CV in different

regions so that our simulation match exactly the clinical data. Instead, we opt for a global optimization of the CV within physiological ranges, which is what would be expected in a real PKN.

One of the main advantages of the method proposed is that the PKN is built estimating the optimal branches for the estimated PMJs, while other methods build first a generic PKN, and then place the PMJs which cannot have an optimal LAT since the CV is fixed. In such approach, one could place the PMJs exactly on each of the endocardial EAM samples, and use the measured LAT, obtaining an error Δ_{EAMs} of 0 ms. However, that will not correspond with the PKN of the patient. In our approach, each of the PMJs that is placed in our model can explain the activation of many endocardial samples, i.e., it is compatible with their spatio-temporal location given a global CV. Hence, we do not have a PMJ associated to each endocardial sample, which in general should not have any spatial relationship.

It is important to point out that sparse EAMs or wrongly annotated ones will cause a reduction in the number of estimated PMJs, which in turn could generate poor PKNs with larger errors in the activation maps. In this study, after filtering the patient EAMs, the number of endocardial samples was always under 400 points, which makes it difficult to obtain a large number of estimated PMJs. Four of the PKN models, namely P8 and P9 (LV and RV), which showed smaller errors, correspond to high density EAMs. That is why it is key the use of high-dense maps such a those provided by multipolar catheters. However, we did not observe a direct relationship between the number of PMJs estimated for a given model and the final error at the EAM samples. One of the most relevant measures of quality is the Link percentage. Therefore, estimated PKN with a 'Link' factor (percentage of EAM samples that gave rise to PMJs) under 70% should be considered carefully or discarded, since the PKN will not be able to reproduce the sequence of activation in at least 30% of the samples. This turns out in average errors above 10 ms, which cannot be considered a patient-specific activation. We had this problem in 8 out of 28 PKN models estimated. Those studies will require a careful revision of EAM LATs, and analysis of local inhomogeneities.

Other studies have reported mean absolute errors at the endocardial mesh, using an estimated PKN, between 4.9 ± 4.1 ms and 7.4 ± 6.6 ms [69], and 5.8 ± 4.5 ms in [72], but using EAMs provided by EnSite NavX system with a number of endocardial samples between 172290 to 571382, and patient geometry segmented from MRI. It is difficult to compare those errors with

the ones reported in Table 5.5, since our EAMs had in average 195 samples. Errors obtained in our models fitted to a segmented LV endocardium were 6.42 ms (219 EAM samples) for patient P12, and 5.61 ms (118 EAM samples), and 6.39 ms (151 EAM samples) for the two maps of P13. Including all cases, if we attend to PKNs with Link higher than 70% (Table 5.5, AVG>70), the average error at EAM from the PKN was 6.10 ± 1.8 ms.

Finally, we showed by means of biophysical simulations that the sequence of activation generated by the patient-specific PKN in patient P12 produced as a result a virtual ECG comparable to the patient one. In addition, virtual ECGs on the same geometrical model generated by stochastic procedures or following descriptions from the literature resulted in non-physiological ECGs. To our knowledge, other studies that try to estimate the PKN have never obtained the corresponding ECGs by simulation. Although, previous studies on synthetic PKN such as [103, 45] obtained simulated ECGs to compare the effect of model parameters or simulate His-Bundle pacing in different scenarios [107].

5.5 Conclusions

We have estimated the PKN from a set of 28 EAMs from patients with idiopathic ventricular fibrillation, obtaining an optimal conduction velocity in the PKN of 1.95 ± 0.25 m/s, the location of PMJs, the PKN structure, and an average local activation time error of 6.1 ± 2.2 ms. Using the patient-specific Purkinje network, we show good agreement between simulated and real ECG in an exemplary case.

In conclusion, I believe that incorporating more personalized information to the biophysical models of the heart, or even into the EAM systems, could help in therapy planning and optimization. The use of computer models to optimized therapies require not only the personalization of the anatomy of the heart but also their electrical properties. In that sense, having a more personalize PKN model and sequence of activation that help to understand patient particularities or enable to study the effect of different treatments on the ECG would be fundamental.

On the other hand, if the estimation method developed would be integrated into an EAM navigation system, the sources of activation could be estimated during an intervention, and the mapping could be guided, acquiring

samples on areas with higher uncertainty, and improving the robustness of the results.

6

Conclusions and Future Work

6.1 Summary

The PKN is a network responsible for the fast transmission of the electrical impulses that trigger the ventricular depolarization [108, 109]. Clinically, the PKN structure is very relevant since it is responsible for the initiation and maintenance of life-threatening arrhythmias [28, 29]. For instance, it is known that some His-Purkinje system-related macro re-entry ventricular tachycardia (VT) are triggered or supported by the PKN, and that the ablation of specific Purkinje-myocardial junctions (PMJs) or bundles can stop the arrhythmia [30, 31].

From a geometrical point of view, it can be seen as a set of interconnected 1D cables, that branch and anastomose, connecting to the underlying endocardial tissue at discrete locations, known as PMJs. The tubular structures are so thin that can not be differentiated with clinical imaging acquisition techniques such as magnetic resonance imaging (MRI) or computed tomography (CT). Therefore, the characterization or reconstruction of the PKN from patient-specific human data is a challenging problem ([91]). In humans, high-resolution imaging techniques have allowed only the segmentation of proximal sections of the PKN from images acquired ex-vivo in combination with specific markers [110, 23, 11]. In animals, several studies have analyzed and modeled either the proximal sections macroscopically [105, 63, 7], or random sections observed with the combination of confocal microscopy and specific inks [18, 19].

A potential way to reconstruct the PKN is to estimate it inversely from electrical activation sequences from the endocardium by means of EAMs. EAMs can be acquired invivo, using catheters that map the electrical activity of a patient in real-time, producing a spatio-temporal map of the activation sequence. Therefore, the structure can be estimated not from images but from the electrical sequence that produces when it activates.

Some methods have already being presented to estimate the PKN from EAMs, by building an initial random network and following reducing the error by moving, adding or pruning branches ([72]) or looking for local minima from EAMs ([71]). However, the goal of those methods was to generate random PKNs compatible with the observed EAM, and not estimating the PKN from the data, or other parameters such as conduction velocities (CVs).

The main goal of this thesis was to develop a methodology that allowed the estimation of the ventricular PKN from EAMs, including the PMJ lo-

cation and PKN structure, that can reproduce patient-specific activation sequence. To accomplish the goal, several methods have been developed so that estimation can be obtained from continuous 2D domains, as well as from discrete 3D domains provided by clinical EAM systems. As a result, patient specific PKN can be estimated from clinical EAMs, to personalize biophysical simulations of cardiac electrophysiology, aiming to help in therapy delivery planning and optimization.

In this thesis, I have evaluated the different methods using synthetic scenarios in which results could be quantitatively evaluated, and the accuracy of the estimated PMJs and PKN could be analyzed under different conditions. The developments have been carried out by increasing the level of complexity of the data to be analyzed, starting from simple 2D tissue sheets, to a 3D endocardial domain that included Gaussian noise in the samples, and ending with real EAM data. Therefore, I could analyze the performance of the estimation algorithm.

6.2 Main findings

In Chapter 3, I have presented a novel methodology to estimate, from virtual EAMs, the location and activation time of the sources of electrical activation, known as PMJs, in a 2D simplified model of cardiac tissue. Therefore, using the location and the corresponding LATs of these estimated PMJs, I can obtain the activation map (simulating a diffusion from these PMJs to the tissue considered).

The following conclusions can be dragged from the numerical results shown in Chapter 3. The proposed method can detect any PMJ if enough measurement points are available, that is, when the scenario has an appropriate ratio between the number of PMJs and samples acquired. It must be observed that in order to detect all PMJs, it is needed to sample, at least, with a density three times higher than the highest density of PMJs. When clustered PMJs appear, many of them are virtually impossible to be detected with the current setup. However, in those scenarios the method still shows a good performance, since many clustered PMJs are non-effective or have a very local impact in the overall activation map. This is confirmed by the mean absolute errors obtained when using estimated PMJs, which are low in all the scenarios (including clustered) for EAMs with more than 600 samples acquired. With low density EAMs (< 250 samples) the method

might perform poorly in dense PMJ scenarios. Compared to previous methods [71], our method outperforms in all scenarios tested when the number of measurement points is greater than 250.

In Chapter 4, I have presented a methodology to estimate the sources of electrical activation in the ventricles, that in normal conditions will correspond to PMJs hotspots. From the electrical information recorded with an EAM system at discrete locations, the method could provide the location and activation times of the electrical triggers with an error bounded by the measurement system error. The errors in location and activation times obtained are small enough to permit the accurate simulation of sequences of activation in biophysical models of cardiac electrophysiology. In areas where a large number of PMJs exist, the system would recover a representative set of source points that can predict the combined effect of all the real PMJs with a low absolute error. Non-clustered PMJs can be located with high precision, even when Gaussian noise is incorporated in the samples.

Finally, the number of endocardial electrical samples required by the method is well within standard clinical EAM procedures, which makes it more applicable. I consider that widely used EAM systems such as CARTO3 (Biosense Webster, Inc), Ensite NavX (St. Jude Medical), or the new Rhythmia system (Boston Scientific), can acquire more than 1000 samples in times that are compatible with an intervention in the EP lab. The location of the PMJs could be useful to reproduce the activation sequence of a given patient in the model, or to plan RFA therapies that target the PMJs to stop a macro-reentrant tachycardia.

Finally, in Chapter 5, I have developed a methodology to build the structure of the PKN that is compatible with the PMJs previously estimated with the minimum number of branches. I have analyzed by means of a simulation study the errors in the activation sequence using estimated PKNs, and I have obtained a very high accuracy (average LAT errors < 1 ms) on synthetic PKNs.

I have also applied successfully the methodology to a cohort of 28 real EAMs (from LV and RV) acquired in sinus rhythm from patients suffering from VT and VF. Results were consistent among cases, showing an optimal CV in the PKN of 1.95 ± 0.25 m/s, and an average number of estimated PMJs of 25. Average errors in the sequence of activation using the personalized PKN were 6.10 ± 2.2 ms for cases where EAMs had a good spatio-temporal consistence. The number and distribution of EAM points on the endocardial surface, as well as the proper annotation of LATs, are critical for a correct

estimation of the PKN model. Otherwise, the number of EAM points that generated PMJs decreases, making it harder to have an overall accurate estimation of the sequence of activation by the estimated PKN. The resulting estimated PKN structure used in a patient-specific biophysical model of the heart allows the personalization of the sequence of activation, and as results showed for an exemplary patient, permit to obtain an accurate in-silico ECG for the patient. Therefore, the model can be used to analyze the patient status, and to plan different types of interventions in cases where the PKN is target for RFA interventions.

In conclusion, the methods and pipeline developed in this thesis have shown the potential to go one step beyond towards personalization of the biophysical models of the heart. In addition, the information about the PMJ distribution and PKN structure, can be used to gain knowledge about patient particularities before an intervention planning.

One of the major advantages of using the developed methodology is the possibility to study different scenarios such as the implantation of a pacemaker that interacts with the PKN, or the most probable locations where PMJs are located when they are targets for RFA.

The translation into the clinical environment does not require experts in the field of modeling and simulations, or time consuming tasks such as segmentation, modeling and biophysical simulations, since the only requirement is the patient's EAM. Therefore, the most important limitation is the quality of the EAMs, which should be dense and well annotated.

The methodology could be easily integrated into already available clinical tools for planning interventions without a big effort, since the methods used in the thesis are standard and available in open-source scientific software packages.

6.3 Contributions

The thesis presents the following contributions, related to the main goals:

- **Estimation of electrical sources of activation on a tissue sheet**. A method to estimate the location and activation time of a set of discrete points that have triggered the activation on a sheet of tissue is developed. The methodology works on an infinite and continuous

2D tissue sheet, and solves an inverse problem to locate the origin of the activation. The accuracy of the method is presented for several distributions of triggering points and sample points.

- **Estimation of PMJs from ventricular endocardium on synthetic 3D models.** The methodology developed previously is extended to work on 3D discrete meshes of the ventricles, such as those obtained from EAM systems. The methodology is analyzed on a series of synthetic 3D PKN models created with different parameters, and for several noise levels.

- **Estimation of PKNs from endocardial EAMs acquired in real patients.** A method to estimate the most plausible simplified PKN structure of a patient based on his EAM is presented. The method is based on the estimation of PMJs, and minimizes the activation error with respect to the patient EAMs considering physiological conduction velocities. The methodology has been successfully applied to a set of real EAMs showing small errors in the LAT maps. In addition, the use of a personalized PKN on a patient model, combined with biophysical simulations, has shown a good match between simulated and real ECGs.

- **Clinical contributions** The methodology presented could estimate the PKN of several patients, showing the most probable location of PMJs and main PKN branches, to plan RFA interventions that target the PKN as a source of arrhythmias. In addition, I have developed software to annotate automatically the samples of EAMs, and obtain the LAT. Finally, I have made use of a quasi-conformal mapping technique to simplify the visualization of LAT maps, and to be able to compare data between patients that can be very useful in clinical environments.

6.4 Limitations

There are several limitations of the work presented that are summarized in the following paragraphs.

One of the drawbacks of the methodology presented is that it requires a few parameters such as the system measurement error, which is the sum of the error location and the automatic LAT annotation. This information,

however, can often be retrieved from the manufacturer of the EAM device used. In addition, the method has to be applied to a large cohort of patient specific EAMs in order to analyze the distribution of PMJs in real cases, and not only in simulated data, to draw meaningful clinical conclusions.

On the other hand, our estimated PKNs are trees, and not networks with closed loops as the ones observed in real Purkinje networks at both proximal ([110, 23]) and terminal sections ([21]). That feature provides the network with resiliency in case of local conduction blocks, or damage of part of the tissue. A complete looped PKN could be required to model pathologies such as bundle branch block, macro-reentries that involve the Purkinje system, or treatments such as cardiac resynchronization therapy. Since I cannot estimate the location of those loops, I choose not to add them synthetically. However, if desired, loops could be created in the required density, without altering the LATs at the PMJs.

The location of the estimated PMJs depends indirectly on the location of the endocardial samples acquired in the cathlab, and therefore, non-homogeneous maps will give rise to unbalanced PMJ distributions and PKN morphologies. An homogeneous sampling is therefore required to obtain meaningful PKNs that can be compared among patients.

It is important to remark that I could not validate the morphology of the PKN, or the location of the estimated PMJs in real patients, since all the studies are performed in vivo. However, the results obtained in synthetic PKN showed that the estimated PKNs were similar to the original ones (comparing distance and angles), and the location of estimated PMJs was close to original one. Nonetheless, to obtain accurate results, the number of endocardial samples, and their LAT error should be bounded.

Finally, I observed that in patients with pathologies that affect conduction velocities, such as patient P6 (NICD), the error Δ_{EAMs} increases with respect to other cases. That inhomogenous activation which might affect the PKN should be specially treated, and probably consider several CVs on the PKN to account on local delays.

6.5 Future Work

Although the methodology presented has fulfilled the goals of the thesis, and has shown good accuracy on both, synthetic and real data, there are still some improvements that could be developed in the future.

The first and most direct improvement is the extension of the PKN to include loops. Since it is reported that the PKN forms closed loops [15, 7], it would be interesting to add them once the PKN is estimated. In that sense, the loops synthetically generated should not alter the estimated LAT at the PMJs. A potential way to personalize a PKN with loops would be to obtain EAMs under pace mapping, so that the activation of the ventricle, when the PKN is retrogradely activated, can be used as an additional source of information.

A second extension should involve the direct validation of the estimated PKN. The validation could be carried out on animal models, where a EAM could be acquired and subsequently analyzed histologically to search for the location of PMJs and PKN branches. In such a case, the species selected should be similar to humans with respect to the Purkinje system. For instance, pigs are known to have an intramural Purkinje system [22], and therefore would not be useful as an animal model.

A third important improvement would be to consider variable conduction velocities within the PKN for cases in which the conduction is impaired inside the PKN due to specific pathologies. This is important to be able to estimate the PKN in specific pathological scenarios, where having information about its morphology would be key.

7

Publications

Journal papers

1. **Barber F.**, Romero P., Langfield P., Lozano M., García-Fernández I., Duchateua J., Hocini M., Haissaguerre M., Vigmond E., Sebastian R. Estimation of personalised minimal Purkinje systems from human electro-anatomical maps. Medical Image Analysis, 2019. [Under revision]

2. **Barber F.**, Lozano M., García-Fernández I., Sebastian R. Automatic Estimation of Purkinje-Myocardial Junction hot-spots from Noisy Endocardial Samples: A simulation study. International Journal for Numerical Methods in Biomedical Engineering, Vol. 34(7):e2988, pp. 1–17, 2018. doi: 10.1002/cnm.2988.

3. **Barber F.**, Lozano M., García-Fernández. I., Sebastian R. Inverse Estimation of Terminal Connections in the Cardiac Conduction System. Mathematical Methods in Applied Sciences, Vol. 41(6):, pp. 2340–2349, 2018. doi: 10.1002/mma.4280.

Conference papers

1. **Barber F.**, Romero P., Langfield P., Lozano M., García-Fernández I., Duchateua J., Hocini M., Haissaguerre M., Vigmond E., Sebastian R. Estimation of a Compatible Cardiac Conduction System From Discrete Endocardial Time Samples. Proceedings Computational and Mathematical Biomedical Engineering, pp. 244–247. Sendai, Japan, 10–12 June, 2019

2. **Barber F.**, M. Lozano, I. García-Fernández, R. Sebastian. Estimation of Location and Activation Time of Purkinje Myocardial Junctions from Sparse and Noisy Endocardial Electrical Samples. Computing in Cardiology, Vol. 44, pp. 1–4. Rennes, France, 2017

3. **Barber F.**, M. Lozano, I. García-Fernández, R. Sebastian. Inverse estimation of terminal connections in the cardiac conduction system. Proceedings of the 16th International Conference on Computational and Mathematical Methods in Science and Engineering, (CMMSE), Cadiz, Spain. 2016

4. **Barber F.**, M. Lozano, I. García-Fernández, R. Sebastian. Automatic location of sources of electrical activation from electrophysiology maps. Computing in Cardiology, Vol. 43, pp. 445–448. Vancouver, Canada, 2016

A

Appendix

A.1 Complete catalogue of PMJ estimation results from synthetic PKNs

In Appendix A.1 we can find all the information and results for the 20 PKN models described in Chapter 4. Tables A.1 and A.2 contain the information and results for all scenarios with 1000 measurement points and Gaussian noise with standard deviation of 0.5 and 2.5 respectively. Figures A.1, A.2 and A.3 contain the plots of the absolute error for all scenarios and figures A.4, A.5 and A.6 contain the plots of the distance from the estimated PMJs to the nearest real PMJ for all scenarios.

Scenario					Gaussian Error 0.5		
Num.	PMJ	Density	TAT pkj(ms)	TAT(ms)	Est. PMJ (%)	Abs. Error(ms)	D. Fe-F(mm)
PK1	1128	94.1 ± 0.7	10.0	51.5	91 ± 4 (8.0)	0.69 ± 0.03	1.19 ± 0.19
PK2	1184	79.6 ± 0.9	14.8	49.9	105 ± 4 (8.9)	0.78 ± 0.05	1.18 ± 0.12
PK3	831	51.9 ± 1.1	15.6	47.4	95 ± 3 (11.4)	0.67 ± 0.03	1.16 ± 0.11
PK4	362	22.6 ± 0.7	12.7	35.1	103 ± 4 (28.3)	0.68 ± 0.04	1.34 ± 0.15
PK5	785	56.1 ± 0.9	14.8	49.8	83 ± 4 (10.6)	0.61 ± 0.03	1.05 ± 0.10
PK6	1224	76.5 ± 0.7	11.3	33.0	116 ± 2 (9.5)	0.82 ± 0.03	1.08 ± 0.03
PK7	212	13.3 ± 0.7	11.3	34.1	86 ± 3 (40.7)	0.59 ± 0.02	1.36 ± 0.08
PK8	647	40.4 ± 0.6	14.8	32.4	124 ± 3 (19.2)	0.87 ± 0.03	1.38 ± 0.09
PK9	203	14.5 ± 0.7	11.6	39.9	70 ± 3 (34.4)	0.52 ± 0.02	1.37 ± 0.14
PK10	663	44.2 ± 0.6	12.7	31.9	124 ± 5 (18.8)	0.87 ± 0.03	1.33 ± 0.09
PK11	442	27.6 ± 0.6	12.8	34.5	108 ± 3 (24.5)	0.75 ± 0.04	1.41 ± 0.13
PK12	434	28.9 ± 0.7	13.2	33.4	98 ± 6 (22.5)	0.67 ± 0.03	1.22 ± 0.09
PK13	435	29.0 ± 0.7	11.2	37.4	90 ± 4 (20.7)	0.64 ± 0.02	1.29 ± 0.07
PK14	213	13.3 ± 0.7	12.3	34.7	89 ± 5 (41.8)	0.61 ± 0.03	1.45 ± 0.12
PK15	206	14.7 ± 0.6	13.5	35.5	86 ± 4 (41.6)	0.60 ± 0.04	1.34 ± 0.15
PK16	217	13.6 ± 0.6	15.3	38.5	93 ± 3 (42.8)	0.64 ± 0.03	1.39 ± 0.11
PK17	208	13.9 ± 0.6	12.2	32.2	88 ± 3 (42.2)	0.60 ± 0.03	1.33 ± 0.08
PK18	215	12.9 ± 0.8	15.4	35.3	95 ± 3 (44.0)	0.66 ± 0.04	1.50 ± 0.11
PK19	376	23.5 ± 0.7	18.1	36.0	107 ± 2 (28.4)	0.73 ± 0.02	1.42 ± 0.10
PK20	389	24.3 ± 0.6	13.3	33.0	119 ± 5 (30.5)	0.83 ± 0.03	1.44 ± 0.09

Table A.1: Information and results for all 3-dimensional scenarios with 1000 measurement points and Gaussian noise with standard deviation of 0.5. *PMJs* represents the number of PMJs in the scenario, *Density* is the density and standard deviation of PMJs per segment (17 AHA segment division), *TAT pkj* is the Total Activation Time of the Purkinje Network, *TAT* is the Total Activation Time for the whole surface/ventricle, *Est. PMJs* is the number of estimated PMJs by the algorithm, *Abs. Error* is the mean of the absolute error in all the points of the mesh and *D. Fe-F* is the distance from an estimated PMJs to the nearest real PMJ.

Scenario					Gaussian Error 2.5			
Num.	PMJ	Density	TAT pkj(ms)	TAT(ms)	Est. PMJ (%)		Abs. Error(ms)	D. Fe-F(mm)
PK1	1128	94.1 ± 0.7	10.0	51.5	53 ± 3	(4.7)	1.64 ± 0.16	3.37 ± 0.76
PK2	1184	79.6 ± 0.9	14.8	49.9	55 ± 2	(4.6)	1.66 ± 0.12	2.45 ± 0.38
PK3	831	51.9 ± 1.1	15.6	47.4	56 ± 5	(6.8)	1.63 ± 0.14	2.71 ± 0.41
PK4	362	22.6 ± 0.7	12.7	35.1	62 ± 3	(17.0)	1.74 ± 0.13	2.84 ± 0.18
PK5	785	56.1 ± 0.9	14.8	49.8	51 ± 3	(6.5)	1.56 ± 0.23	2.62 ± 0.48
PK6	1224	76.5 ± 0.7	11.3	33.0	62 ± 5	(5.0)	1.74 ± 0.10	1.92 ± 0.27
PK7	212	13.3 ± 0.7	11.3	34.1	59 ± 4	(27.7)	1.60 ± 0.10	2.91 ± 0.24
PK8	647	40.4 ± 0.6	14.8	32.4	62 ± 5	(9.6)	1.79 ± 0.10	2.18 ± 0.21
PK9	203	14.5 ± 0.7	11.6	39.9	46 ± 4	(22.8)	1.42 ± 0.18	4.04 ± 0.88
PK10	663	44.2 ± 0.6	12.7	31.9	66 ± 8	(9.9)	1.85 ± 0.10	2.39 ± 0.31
PK11	442	27.6 ± 0.6	12.8	34.5	63 ± 3	(14.2)	1.74 ± 0.11	2.58 ± 0.33
PK12	434	28.9 ± 0.7	13.2	33.4	56 ± 5	(12.9)	1.64 ± 0.08	2.63 ± 0.25
PK13	435	29.0 ± 0.7	11.2	37.4	55 ± 5	(12.6)	1.63 ± 0.12	3.03 ± 0.66
PK14	213	13.3 ± 0.7	12.3	34.7	56 ± 3	(26.3)	1.56 ± 0.14	2.73 ± 0.26
PK15	206	14.7 ± 0.6	13.5	35.5	53 ± 4	(25.8)	1.67 ± 0.10	3.21 ± 0.33
PK16	217	13.6 ± 0.6	15.3	38.5	56 ± 3	(26.0)	1.57 ± 0.08	2.88 ± 0.32
PK17	208	13.9 ± 0.6	12.2	32.2	56 ± 4	(26.8)	1.59 ± 0.11	3.16 ± 0.34
PK18	215	12.9 ± 0.8	15.4	35.3	57 ± 3	(26.7)	1.62 ± 0.10	3.20 ± 0.27
PK19	376	23.5 ± 0.7	18.1	36.0	60 ± 3	(15.9)	1.69 ± 0.10	2.59 ± 0.25
PK20	389	24.3 ± 0.6	13.3	33.0	63 ± 4	(16.2)	1.75 ± 0.06	2.47 ± 0.19

Table A.2: Information and results for all 3-dimensional scenarios with 1000 measurement points and Gaussian noise with standard deviation of 2.5. *PMJs* represents the number of PMJs in the scenario, *Density* is the density and standard deviation of PMJs per segment (17 AHA segment division), *TAT pkj* is the Total Activation Time of the Purkinje Network, *TAT* is the Total Activation Time for the whole surface/ventricle, *Est. PMJs* is the number of estimated PMJs by the algorithm, *Abs. Error* is the mean of the absolute error in all the points of the mesh and *D. Fe-F* is the distance from an estimated PMJs to the nearest real PMJ.

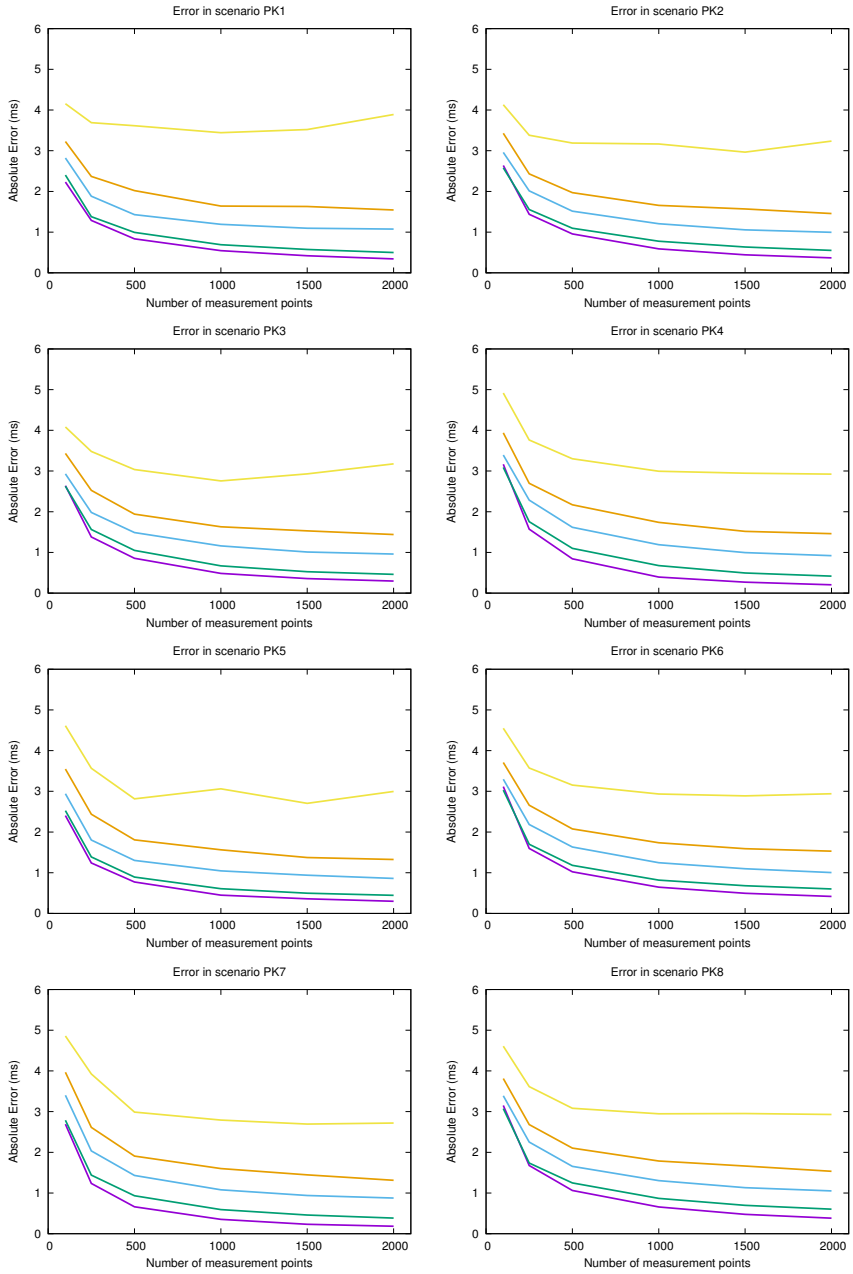

Figure A.1: Plots of the absolute error for scenarios PK1 to PK8.

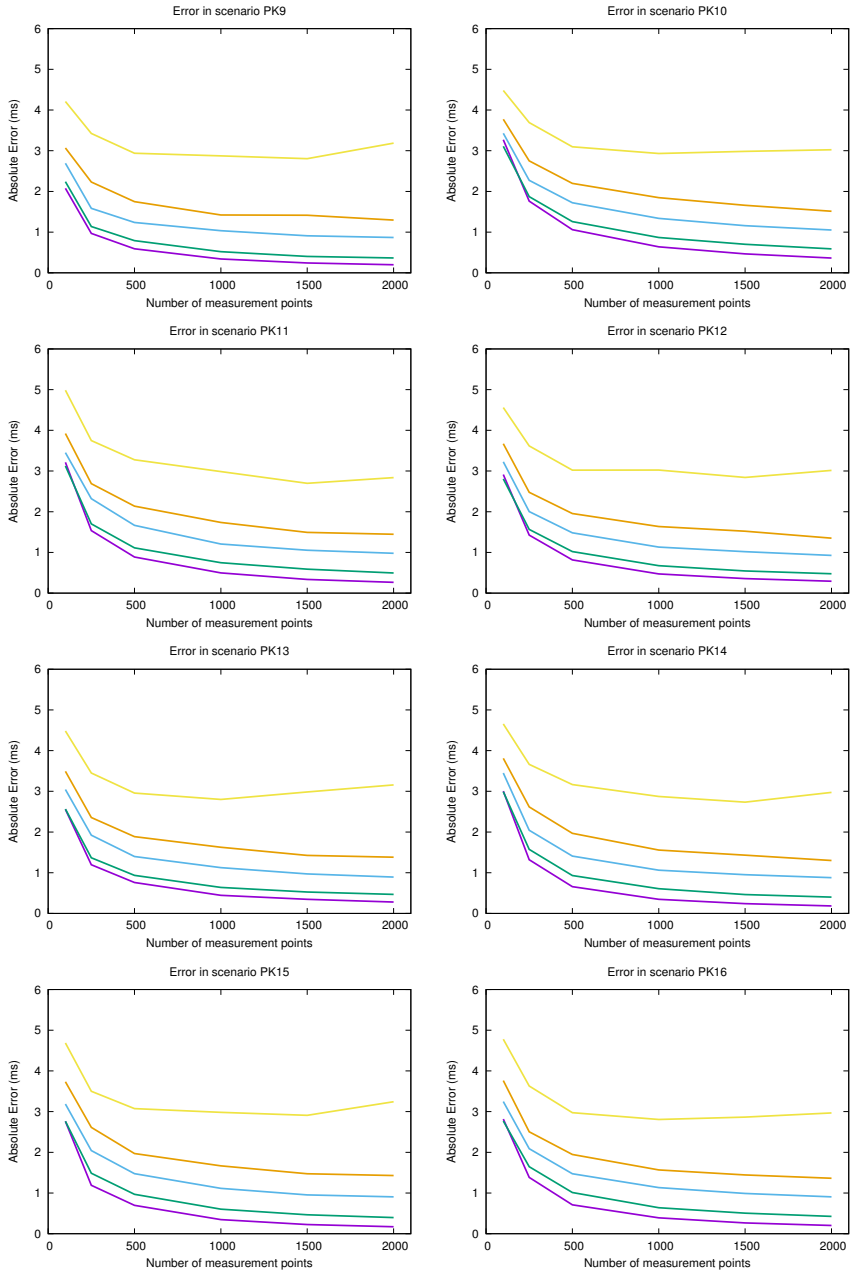

Figure A.2: Plots of the absolute error for scenarios PK9 to PK16.

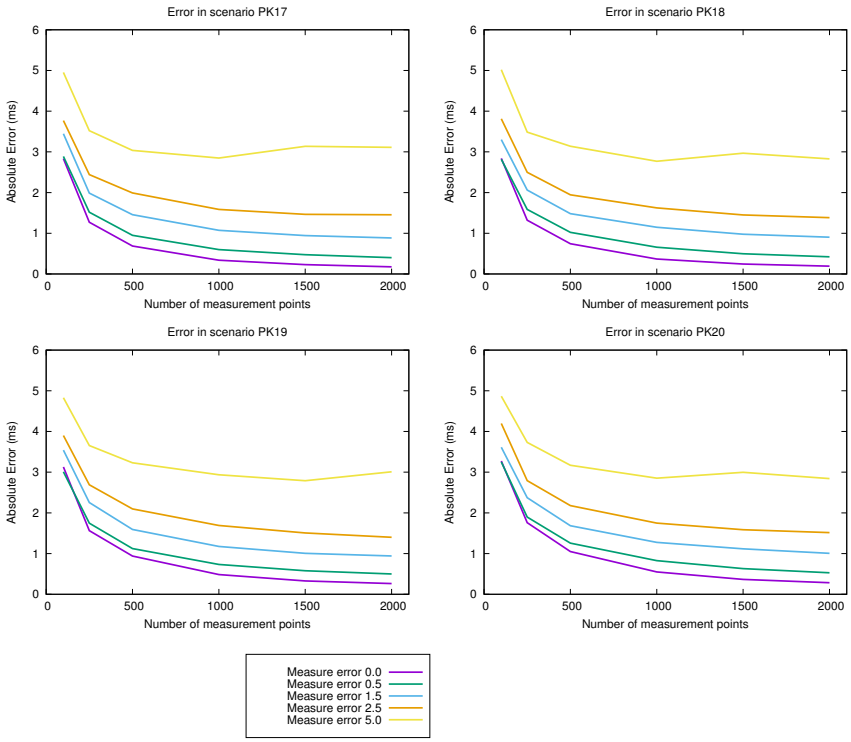

Figure A.3: Plots of the absolute error for scenarios PK17 to PK20.

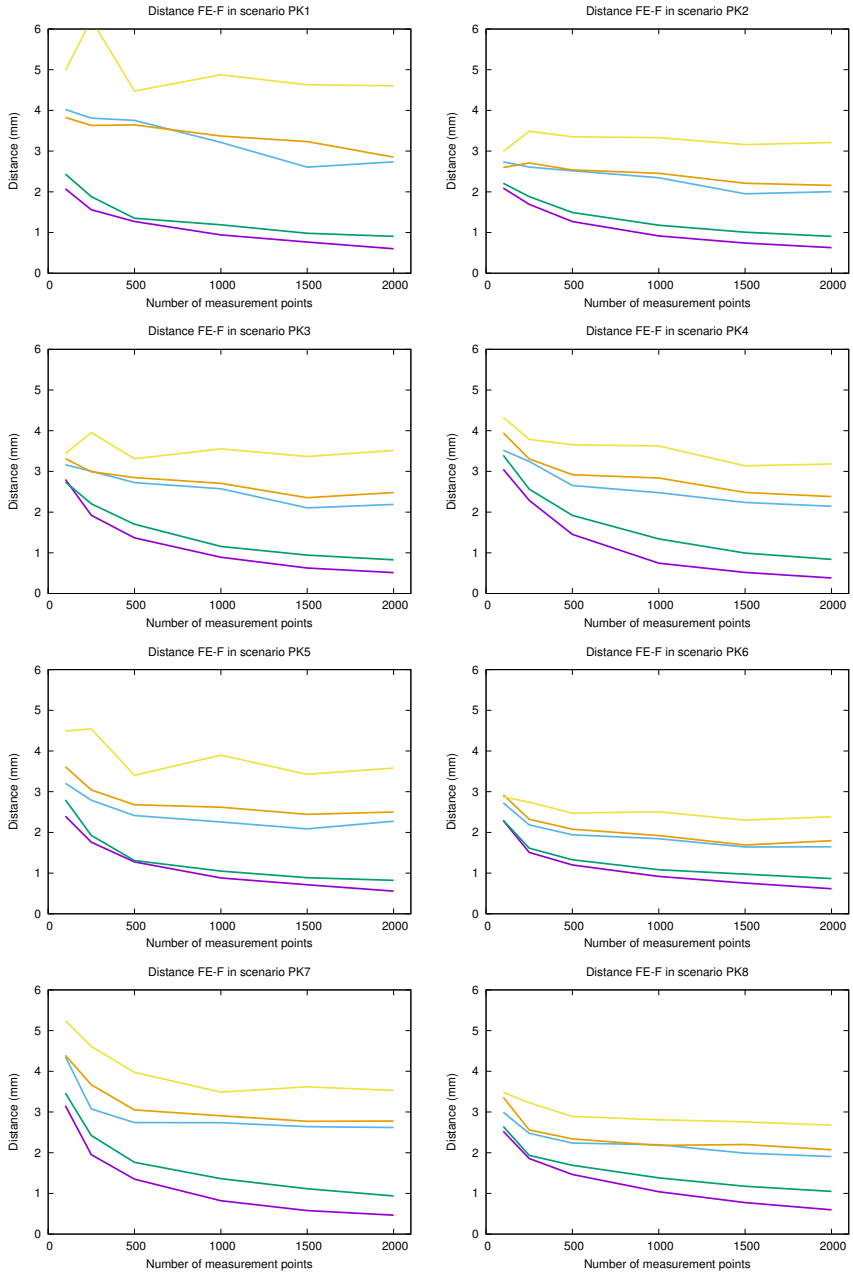

Figure A.4: Plots of the distance from estimated PMJs to real PMJs for scenarios PK1 to PK8.

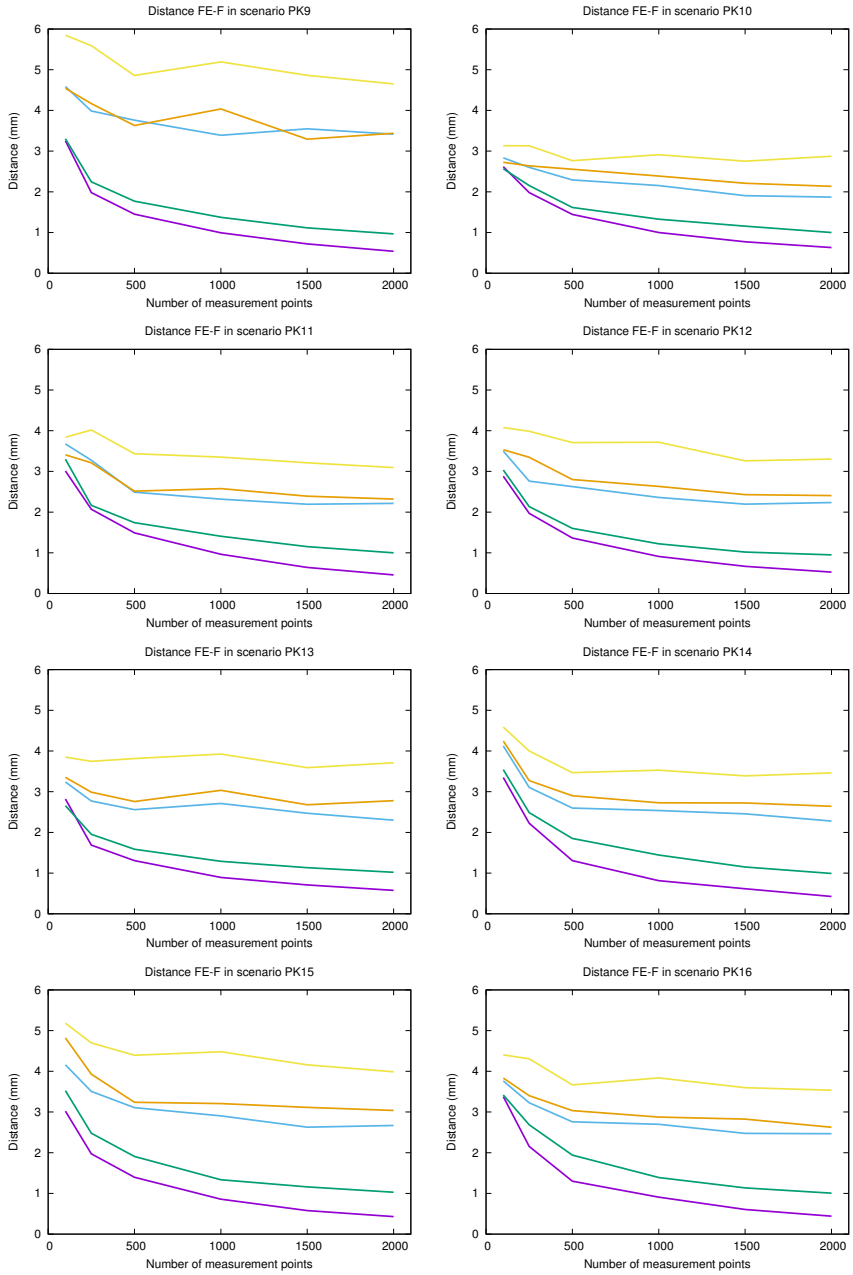

Figure A.5: Plots of the distance from estimated PMJs to real PMJs for scenarios PK9 to PK16.

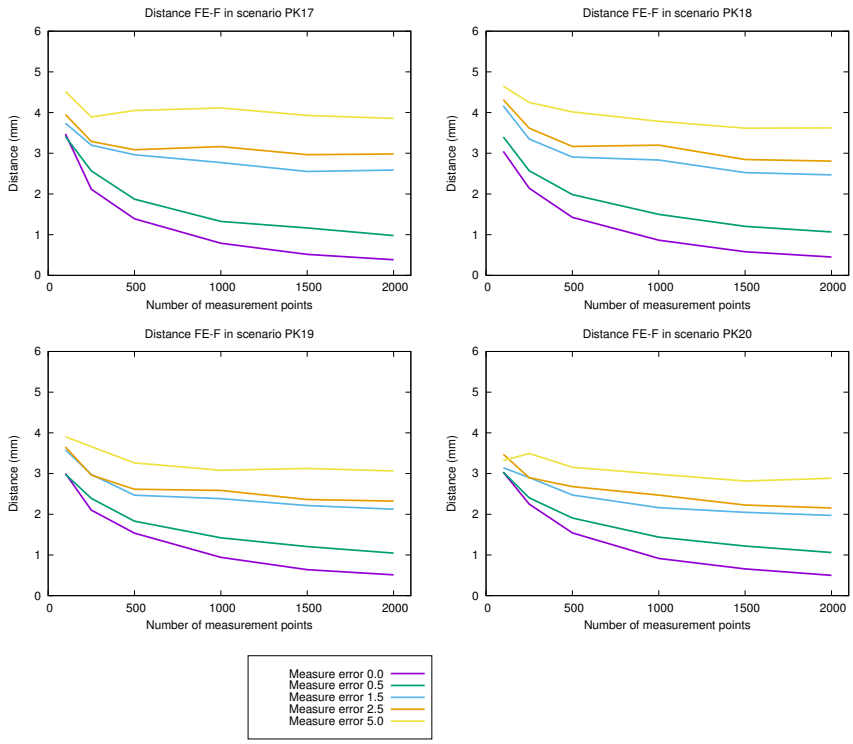

Figure A.6: Plots of the distance from estimated PMJs to real PMJs for scenarios PK17 to PK20.

A.2 Additional PKN models estimated from synthetic data and patient EAMs

In Appendix A.2 we include additional figures about estimated PKN structures for cases not included in Chapter 5.

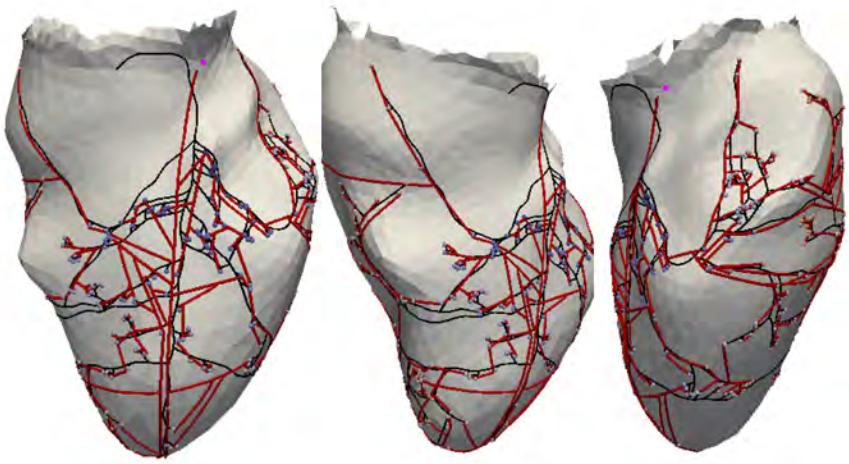

Figure A.7: Complete views for estimated and real synthetic PK3.

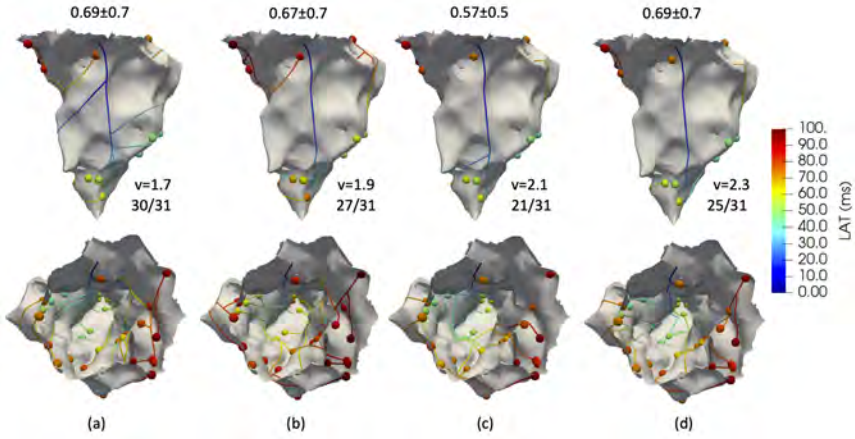

Figure A.8: Estimated PKN for P1 LV EAM for different CVs. Colors correspond to the LATs. PMJs (spheres) together with Δ_{PMJs} and standard deviations (in ms) are included for each velocity, together with the PMJs connected ($\epsilon_{max} < 5ms$).

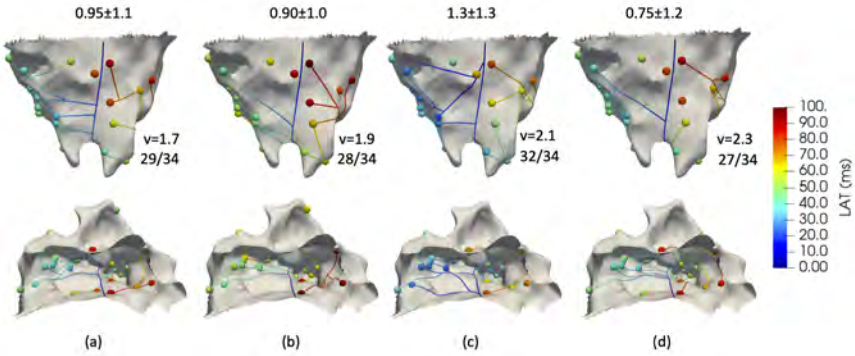

Figure A.9: Estimated PKN for P1 RV EAM for different CVs. Colors correspond to the LATs. PMJs (spheres) together with Δ_{PMJs} and standard deviations (in ms) are included for each velocity, together with the PMJs connected ($\epsilon_{max} < 5ms$).

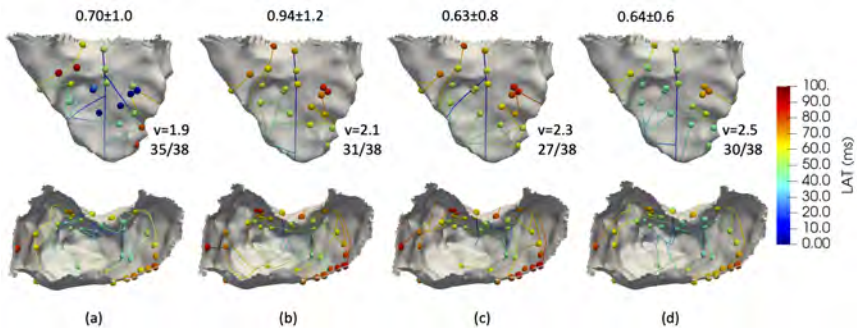

Figure A.10: Estimated PKN for P2 RV EAM for different CVs. Colors correspond to the LATs. PMJs (spheres) together with Δ_{PMJs} and standard deviations (in ms) are included for each velocity, together with the PMJs connected ($\epsilon_{max} < 5ms$).

Bibliography

[1] Pooja J Sheth, Gary H Danton, Yoel Siegel, Richard E Kardon, Juan C Infante, Jr, Eduard Ghersin, and Joel E Fishman. Cardiac physiology for radiologists: Review of relevant physiology for interpretation of cardiac mr imaging and ct. *Radiographics*, 35(5):1335–51, 2015.

[2] Adelina Doltra, Brage Hoyem Amundsen, Rolf Gebker, Eckart Fleck, and Sebastian Kelle. Emerging concepts for myocardial late gadolinium enhancement mri. *Curr Cardiol Rev*, 9(3):185–90, Aug 2013.

[3] Hugh Calkins, Karl Heinz Kuck, Riccardo Cappato, Josep Brugada, A John Camm, Shih-Ann Chen, Harry J G Crijns, Ralph J Damiano, Jr, D Wyn Davies, John DiMarco, James Edgerton, Kenneth Ellenbogen, Michael D Ezekowitz, David E Haines, Michel Haissaguerre, Gerhard Hindricks, Yoshito Iesaka, Warren Jackman, Jose Jalife, Pierre Jais, Jonathan Kalman, David Keane, Young-Hoon Kim, Paulus Kirchhof, George Klein, Hans Kottkamp, Koichiro Kumagai, Bruce D Lindsay, Moussa Mansour, Francis E Marchlinski, Patrick M McCarthy, J Lluis Mont, Fred Morady, Koonlawee Nademanee, Hiroshi Nakagawa, Andrea Natale, Stanley Nattel, Douglas L Packer, Carlo Pappone, Eric Prystowsky, Antonio Raviele, Vivek Reddy, Jeremy N Ruskin, Richard J Shemin, Hsuan-Ming Tsao, and David Wilber. 2012 hrs/ehra/ecas expert consensus statement on catheter and surgical ablation of atrial fibrillation: recommendations for patient selection, procedural techniques, patient management and follow-up, definitions, endpoints, and research trial design. *Europace*, 14(4):528–606, Apr 2012.

[4] Steven A Niederer, Joost Lumens, and Natalia A Trayanova. Computational models in cardiology. *Nat Rev Cardiol*, 16(2):100–111, Feb 2019.

[5] Natalia A Trayanova and Patrick M Boyle. Advances in modeling ventricular arrhythmias: from mechanisms to the clinic. *Wiley Interdiscip Rev Syst Biol Med*, 6(2):209–24, 2014.

[6] Alejandro Lopez-Perez, Rafael Sebastian, and Jose M Ferrero. Three-dimensional cardiac computational modelling: methods, features and applications. *Biomed Eng Online*, 14:35, Apr 2015.

[7] Rafael Sebastian, Viviana Zimmerman, Daniel Romero, Damian Sanchez-

Quintana, and Alejandro F Frangi. Characterization and modeling of the peripheral cardiac conduction system. *IEEE Trans Med Imaging*, 32(1):45–55, Jan 2013.

[8] Ghassen Cheniti, Konstantinos Vlachos, Marianna Meo, Stephane Puyo, Nathaniel Thompson, Arnaud Denis, Josselin Duchateau, Masateru Takigawa, Claire Martin, Antonio Frontera, Takeshi Kitamura, Anna Lam, Felix Bourier, Nicolas Klotz, Nicolas Derval, Frederic Sacher, Pierre Jais, Remi Dubois, Meleze Hocini, and Michel Haissaguerre. Mapping and ablation of idiopathic ventricular fibrillation. *Front Cardiovasc Med*, 5:123, 2018.

[9] Michel Haissaguerre, Ghassen Cheniti, William Escande, Alexandre Zhao, Mélèze Hocini, and Olivier Bernus. Idiopathic ventricular fibrillation with repetitive activity inducible within the distal purkinje system. *Heart Rhythm*, 16(8):1268–1272, Aug 2019.

[10] John E Hall. *Guyton and Hall textbook of medical physiology e-Book*. Elsevier Health Sciences, 2015.

[11] Robert S Stephenson, Mark R Boyett, George Hart, Theodora Nikolaidou, Xue Cai, Antonio F Corno, Nelson Alphonso, Nathan Jeffery, and Jonathan C Jarvis. Contrast enhanced micro-computed tomography resolves the 3-dimensional morphology of the cardiac conduction system in mammalian hearts. *PLoS One*, 7(4):e35299, 2012.

[12] A Keith and M Flack. The form and nature of the muscular connections between the primary divisions of the vertebrate heart. *Journal of anatomy and physiology*, 41(Pt 3):172–189, 04 1907.

[13] R J Myerburg, K Nilsson, and H Gelband. Physiology of canine intraventricular conduction and endocardial excitation. *Circ Res*, 30(2):217–243, February 1972.

[14] S Tawara. Das Reizleitungssystem des Säugetierherzens. Eine anatomisch-histologische studie über das Atrioventricularbündel und die Purkinjeschen Fäden. *Jena, Verlag v. Gustav Fischer*, 1906.

[15] Damián Sanchez-Quintana and Siew Yen Ho. Anatomy of cardiac nodes and atrioventricular specialized conduction system. *Rev Esp Cardiol*, 56(11):1085–1092, November 2003.

[16] P W Oosthoek, S Viragh, W H Lamers, and A F Moorman. Immunohistochemical delineation of the conduction system. II: The atrioventricular node and Purkinje fibers. *Circ Res*, 73(3):482–491, September 1993.

[17] J C Demoulin and H E Kulbertus. Histopathological examination of concept of left hemiblock. *Heart*, 34(8):807–814, August 1972.

[18] A Ansari, S Y Ho, and R H Anderson. Distribution of the Purkinje fibres in the sheep heart. *Anat Rec*, 254(1):92–97, January 1999.

[19] Shonosuke Ryu, Shoji Yamamoto, Clark R Andersen, Kiyoshi Nakazawa, Fumihiko Miyake, and Thomas N James. Intramural purkinje cell network of sheep ventricles as the terminal pathway of conduction system. *Anat Rec*

(Hoboken), 292(1):12–22, January 2009.

[20] J Tranum-Jensen, A A Wilde, J T Vermeulen, and M J Janse. Morphology of electrophysiologically identified junctions between Purkinje fibers and ventricular muscle in rabbit and pig hearts. *Circ Res*, 69(2):429–437, August 1991.

[21] Daniel Romero, Oscar Camara, Frank Sachse, and Rafael Sebastian. Analysis of microstructure of the cardiac conduction system based on three-dimensional confocal microscopy. *PLoS One*, 11(10):e0164093, 2016.

[22] V Garcia-Bustos, R Sebastian, M Izquierdo, P Molina, F J Chorro, and A Ruiz-Sauri. A quantitative structural and morphometric analysis of the purkinje network and the purkinje-myocardial junctions in pig hearts. *J Anat*, 230(5):664–678, May 2017.

[23] Robert S Stephenson, Andrew Atkinson, Petros Kottas, Filip Perde, Fatemeh Jafarzadeh, Mike Bateman, Paul A Iaizzo, Jichao Zhao, Henggui Zhang, Robert H Anderson, Jonathan C Jarvis, and Halina Dobrzynski. High resolution 3-dimensional imaging of the human cardiac conduction system from microanatomy to mathematical modeling. *Sci Rep*, 7(1):7188, Aug 2017.

[24] A W Cates, W M Smith, R E Ideker, and A E Pollard. Purkinje and ventricular contributions to endocardial activation sequence in perfused rabbit right ventricle. *Am J Physiol Heart Circ Physiol*, 281(2):H490—-H505, August 2001.

[25] Frits W Prinzen and Maaike Peschar. Relation between the pacing induced sequence of activation and left ventricular pump function in animals. *Pacing Clin Electrophysiol*, 25(4 Pt 1):484–498, April 2002.

[26] D Durrer, R T van Dam, G E Freud, M J Janse, F L Meijler, and R C Arzbaecher. Total excitation of the isolated human heart. *Circulation*, 41(6):899–912, Jun 1970.

[27] Aksana Baldzizhar, Ekaterina Manuylova, Roman Marchenko, Yury Kryvalap, and Mary G Carey. Ventricular tachycardias: Characteristics and management. *Crit Care Nurs Clin North Am*, 28(3):317–29, Sep 2016.

[28] O Berenfeld and J Jalife. Purkinje-muscle reentry as a mechanism of polymorphic ventricular arrhythmias in a 3-dimensional model of the ventricles. *Circ Res*, 82(10):1063–77, Jun 1998.

[29] Yuki Komatsu, Mélèze Hocini, Akihiko Nogami, Philippe Maury, Petr Peichl, Yu-Ki Iwasaki, Keita Masuda, Arnaud Denis, Quentin Voglimacci-Stephanopoli, Dan Wichterle, Mitsuharu Kawamura, Seiji Fukamizu, Yasuhiro Yokoyama, Yasushi Mukai, Tomoo Harada, Kentaro Yoshida, Ryobun Yasuoka, Masayuki Igawa, Koji Ohira, Wataru Shimizu, Kazutaka Aonuma, Josef Kautzner, Michel Haïssaguerre, and Masaki Ieda. Catheter ablation of refractory ventricular fibrillation storm after myocardial infarction. *Circulation*, 139(20):2315–2325, May 2019.

[30] Michel Haissaguerre, Edward Vigmond, Bruno Stuyvers, Meleze Hocini, and Olivier Bernus. Ventricular arrhythmias and the his-purkinje system. *Nat*

Rev Cardiol, 13(3):155–66, Mar 2016.

[31] Beixin Julie He, Penelope Boyden, and Melvin Scheinman. Ventricular arrhythmias involving the his-purkinje system in the structurally abnormal heart. *Pacing Clin Electrophysiol*, 41(9):1051–1059, 09 2018.

[32] Akihiko Nogami. Purkinje-related arrhythmias part i: monomorphic ventricular tachycardias. *Pacing Clin Electrophysiol*, 34(5):624–50, May 2011.

[33] L Gepstein and S J Evans. Electroanatomical mapping of the heart: basic concepts and implications for the treatment of cardiac arrhythmias. *Pacing Clin Electrophysiol*, 21(6):1268–78, Jun 1998.

[34] Martin Rotter, Yoshihide Takahashi, Prashanthan Sanders, Michel Haïssaguerre, Pierre Jaïs, Li-Fern Hsu, Fréderic Sacher, Jean-Luc Pasquié, Jacques Clementy, and Mélèze Hocini. Reduction of fluoroscopy exposure and procedure duration during ablation of atrial fibrillation using a novel anatomical navigation system. *Eur Heart J*, 26(14):1415–21, Jul 2005.

[35] Emmanuel Koutalas, Sascha Rolf, Borislav Dinov, Sergio Richter, Arash Arya, Andreas Bollmann, Gerhard Hindricks, and Philipp Sommer. Contemporary mapping techniques of complex cardiac arrhythmias - identifying and modifying the arrhythmogenic substrate. *Arrhythm Electrophysiol Rev*, 4(1):19–27, May 2015.

[36] Carlo Pappone, Carmine Garzillo, Simonetta Crisa, and Vincenzo Santinelli. *Electroanatomical Mapping Systems. An Epochal Change in Cardiac Electrophysiology*, pages 237–255. Springer International Publishing, Cham, 2016.

[37] Mathias Forkmann, Carolina Schwab, and Sonia Busch. [catheter ablation of supraventricular tachycardia]. *Herzschrittmacherther Elektrophysiol*, Nov 2019.

[38] Sana M Al-Khatib, William G Stevenson, Michael J Ackerman, William J Bryant, David J Callans, Anne B Curtis, Barbara J Deal, Timm Dickfeld, Michael E Field, Gregg C Fonarow, Anne M Gillis, Christopher B Granger, Stephen C Hammill, Mark A Hlatky, José A Joglar, G Neal Kay, Daniel D Matlock, Robert J Myerburg, and Richard L Page. 2017 aha/acc/hrs guideline for management of patients with ventricular arrhythmias and the prevention of sudden cardiac death: Executive summary. *Circulation*, 138(13):e210–e271, 09 2018.

[39] A L Hodgkin and A F Huxley. A quantitative description of membrane current and its application to conduction and excitation in nerve. 1952. *Bull Math Biol*, 52(1-2):25–71; discussion 5–23, 1990.

[40] Denis Noble. Successes and failures in modeling heart cell electrophysiology. *Heart Rhythm*, 8(11):1798–803, Nov 2011.

[41] Denis Noble. From the hodgkin-huxley axon to the virtual heart. *J Physiol*, 580(Pt 1):15–22, Apr 2007.

[42] Hermenegild J Arevalo, Patrick M Boyle, and Natalia A Trayanova. Computational rabbit models to investigate the initiation, perpetuation, and ter-

mination of ventricular arrhythmia. *Prog Biophys Mol Biol*, 121(2):185–94, 07 2016.

[43] Edward Vigmond, Fijoy Vadakkumpadan, Viatcheslav Gurev, Hermenegild Arevalo, Makarand Deo, Gernot Plank, and Natalia Trayanova. Towards predictive modelling of the electrophysiology of the heart. *Exp Physiol*, 94(5):563–77, May 2009.

[44] K H Ten Tusscher and A V Panfilov. Cell model for efficient simulation of wave propagation in human ventricular tissue under normal and pathological conditions. *Phys Med Biol*, 51(23):6141–6156, December 2006.

[45] Lydia Dux-Santoy, Rafael Sebastian, Jose Felix-Rodriguez, Jose Maria Ferrero, and Javier Saiz. Interaction of specialized cardiac conduction system with antiarrhythmic drugs: a simulation study. *IEEE Trans Biomed Eng*, 58(12):3475–8, Dec 2011.

[46] Natalia A Trayanova and Kelly C Chang. How computer simulations of the human heart can improve anti-arrhythmia therapy. *J Physiol*, 594(9):2483–502, May 2016.

[47] M L Buist and A J Pullan. From cell to body surface: a fully coupled approach. *J Electrocardiol*, 34 Suppl:191–5, 2001.

[48] Raimond L Winslow, Natalia Trayanova, Donald Geman, and Michael I Miller. Computational medicine: translating models to clinical care. *Sci Transl Med*, 4(158):158rv11, Oct 2012.

[49] J P Keener and K Bogar. A numerical method for the solution of the bidomain equations in cardiac tissue. *Chaos*, 8(1):234–241, March 1998.

[50] Mark Potse, Bruno Dubé, Jacques Richer, Alain Vinet, and Ramesh M Gulrajani. A comparison of monodomain and bidomain reaction-diffusion models for action potential propagation in the human heart. *IEEE Trans Biomed Eng*, 53(12 Pt 1):2425–2435, December 2006.

[51] Dongdong Deng, Hermenegild J Arevalo, Adityo Prakosa, David J Callans, and Natalia A Trayanova. A feasibility study of arrhythmia risk prediction in patients with myocardial infarction and preserved ejection fraction. *Europace*, 18(suppl 4):iv60–iv66, Dec 2016.

[52] Chris Bradley, Andy Bowery, Randall Britten, Vincent Budelmann, Oscar Camara, Richard Christie, Andrew Cookson, Alejandro F Frangi, Thiranja Babarenda Gamage, Thomas Heidlauf, Sebastian Krittian, David Ladd, Caton Little, Kumar Mithraratne, Martyn Nash, David Nickerson, Poul Nielsen, Oyvind Nordbø, Stig Omholt, Ali Pashaei, David Paterson, Vijayaraghavan Rajagopal, Adam Reeve, Oliver Röhrle, Soroush Safaei, Rafael Sebastián, Martin Steghöfer, Tim Wu, Ting Yu, Heye Zhang, and Peter Hunter. Opencmiss: a multi-physics & multi-scale computational infrastructure for the vph/physiome project. *Prog Biophys Mol Biol*, 107(1):32–47, Oct 2011.

[53] Travis Austin, Mark Trew, and Andrew Pullan. A comparison of multilevel solvers for the cardiac bidomain equations. *Conf Proc IEEE Eng Med Biol*

Soc, 7:7204–7207, 2005.

[54] D Sanchez-Quintana, V Garcia-Martinez, V Climent, and J M Hurle. Morphological changes in the normal pattern of ventricular myoarchitecture in the developing human heart. *Anat Rec*, 243(4):483–95, Dec 1995.

[55] Nathan S Jeffery, Robert S Stephenson, James A Gallagher, Jonathan C Jarvis, and Philip G Cox. Micro-computed tomography with iodine staining resolves the arrangement of muscle fibres. *J Biomech*, 44(1):189–92, Jan 2011.

[56] D D Streeter, Jr, H M Spotnitz, D P Patel, J Ross, Jr, and E H Sonnenblick. Fiber orientation in the canine left ventricle during diastole and systole. *Circ Res*, 24(3):339–47, Mar 1969.

[57] Farhad Pashakhanloo, Daniel A Herzka, Susumu Mori, Muz Zviman, Henry Halperin, Neville Gai, David A Bluemke, Natalia A Trayanova, and Elliot R McVeigh. Submillimeter diffusion tensor imaging and late gadolinium enhancement cardiovascular magnetic resonance of chronic myocardial infarction. *J Cardiovasc Magn Reson*, 19(1):9, Jan 2017.

[58] Elham Behradfar, Anders Nygren, and Edward J Vigmond. The role of purkinje-myocardial coupling during ventricular arrhythmia: a modeling study. *PLoS One*, 9(2):e88000, 2014.

[59] S Abboud, O Berenfeld, and D Sadeh. Simulation of high-resolution qrs complex using a ventricular model with a fractal conduction system. effects of ischemia on high-frequency qrs potentials. *Circ Res*, 68(6):1751–60, Jun 1991.

[60] Takashi Ijiri, Takashi Ashihara, Takeshi Yamaguchi, Kenshi Takayama, Takeo Igarashi, Tatsuo Shimada, Tsunetoyo Namba, Ryo Haraguchi, and Kazuo Nakazawa. A procedural method for modeling the purkinje fibers of the heart. *J Physiol Sci*, 58(7):481–6, Dec 2008.

[61] Daniel Romero, Rafael Sebastian, Bart H Bijnens, Viviana Zimmerman, Patrick M Boyle, Edward J Vigmond, and Alejandro F Frangi. Effects of the purkinje system and cardiac geometry on biventricular pacing: a model study. *Ann Biomed Eng*, 38(4):1388–98, Apr 2010.

[62] Edward J Vigmond and Clyde Clements. Construction of a computer model to investigate sawtooth effects in the purkinje system. *IEEE Trans Biomed Eng*, 54(3):389–99, Mar 2007.

[63] Benjamin R. Liu and Elizabeth M. Cherry. Image-based structural modeling of the cardiac purkinje network. *BioMed Research International*, 2015(621034):1 –15, 2015.

[64] Fijoy Vadakkumpadan, Lukas J Rantner, Brock Tice, Patrick Boyle, Anton J Prassl, Edward Vigmond, Gernot Plank, and Natalia Trayanova. Image-based models of cardiac structure with applications in arrhythmia and defibrillation studies. *J Electrocardiol*, 42(2):157.e1—-157.10, 2009.

[65] Gernot Plank, Rebecca A B Burton, Patrick Hales, Martin Bishop, Tahir

Mansoori, Miguel O Bernabeu, Alan Garny, Anton J Prassl, Christian Bollensdorff, Fleur Mason, Fahd Mahmood, Blanca Rodriguez, Vicente Grau, Jürgen E Schneider, David Gavaghan, and Peter Kohl. Generation of histo-anatomically representative models of the individual heart: tools and application. *Philos Transact A Math Phys Eng Sci*, 367(1896):2257–2292, June 2009.

[66] R Bordas, K Gillow, Q Lou, I R Efimov, D Gavaghan, P Kohl, V Grau, and B Rodriguez. Rabbit-specific ventricular model of cardiac electrophysiological function including specialized conduction system. *Prog Biophys Mol Biol*, 107(1):90–100, October 2011.

[67] Penelope A Boyden, Wen Dun, and Richard B Robinson. Cardiac purkinje fibers and arrhythmias; the gk moe award lecture 2015. *Heart Rhythm*, 13(5):1172–81, May 2016.

[68] Alexandra E Teng, Daniel L Lustgarten, Pugazhendhi Vijayaraman, Roderick Tung, Kalyanam Shivkumar, Galen S Wagner, and Olujimi A Ajijola. Usefulness of his bundle pacing to achieve electrical resynchronization in patients with complete left bundle branch block and the relation between native qrs axis, duration, and normalization. *Am J Cardiol*, 118(4):527–34, Aug 2016.

[69] Christian Vergara, Simone Palamara, Domenico Catanzariti, Fabio Nobile, Elena Faggiano, Cesarino Pangrazzi, Maurizio Centonze, Massimiliano Maines, Alfio Quarteroni, and Giuseppe Vergara. Patient-specific generation of the purkinje network driven by clinical measurements of a normal propagation. *Med Biol Eng Comput*, 52(10):813–26, Oct 2014.

[70] Simone Palamara, Christian Vergara, Domenico Catanzariti, Elena Faggiano, Cesarino Pangrazzi, Maurizio Centonze, Fabio Nobile, Massimiliano Maines, and Alfio Quarteroni. Computational generation of the purkinje network driven by clinical measurements: the case of pathological propagations. *Int J Numer Method Biomed Eng*, 30(12):1558–77, Dec 2014.

[71] Rubén Cárdenes, Rafael Sebastian, David Soto-Iglesias, Antonio Berruezo, and Oscar Camara. Estimation of purkinje trees from electro-anatomical mapping of the left ventricle using minimal cost geodesics. *Med Image Anal*, 24(1):52–62, Aug 2015.

[72] Simone Palamara, Christian Vergara, Elena Faggiano, and Fabio Nobile. An effective algorithm for the generation of patient-specific purkinje networks in computational electrocardiology. *Journal of Computational Physics*, 283(Supplement C):495 – 517, 2015.

[73] Fernando Barber, Miguel Lozano, Ignacio Garcia-Fernandez, and Rafael Sebastian. Inverse estimation of terminal connections in the cardiac conduction system. *Mathematical Methods in Applied Sciences*, 41(6):2340–2349, 2018.

[74] Natalia A Trayanova. Whole-heart modeling: applications to cardiac electrophysiology and electromechanics. *Circ Res*, 108(1):113–28, Jan 2011.

[75] Adityo Prakosa, Hermenegild J Arevalo, Dongdong Deng, Patrick M Boyle,

Plamen P Nikolov, Hiroshi Ashikaga, Joshua Je Blauer, Elyar Ghafoori, Carolyn J Park, Robert C Blake, 3rd, Frederick T Han, Rob S MacLeod, Henry R Halperin, David J Callans, Ravi Ranjan, Jonathan Chrispin, Saman Nazarian, and Natalia A Trayanova. Personalized virtual-heart technology for guiding the ablation of infarct-related ventricular tachycardia. *Nat Biomed Eng*, 2(10):732–740, Oct 2018.

[76] Daniel Romero, Rafael Sebastian, Bart H Bijnens, Viviana Zimmerman, Patrick M Boyle, Edward J Vigmond, and Alejandro F Frangi. Effects of the purkinje system and cardiac geometry on biventricular pacing: a model study. *Ann Biomed Eng*, 38(4):1388–1398, April 2010.

[77] Patrick M Boyle, Makarand Deo, Gernot Plank, and Edward J Vigmond. Purkinje-mediated effects in the response of quiescent ventricles to defibrillation shocks. *Ann Biomed Eng*, 38(2):456–468, February 2010.

[78] Sophie Giffard-Roisin, Herve Delingette, Thomas Jackson, Jessica Webb, Lauren Fovargue, Jack Lee, Christopher A Rinaldi, Reza Razavi, Nicholas Ayache, and Maxime Sermesant. Transfer learning from simulations on a reference anatomy for ecgi in personalized cardiac resynchronization therapy. *IEEE Trans Biomed Eng*, 66(2):343–353, 02 2019.

[79] Patrick M Boyle, Sohail Zahid, and Natalia A Trayanova. Using personalized computer models to custom-tailor ablation procedures for atrial fibrillation patients: are we there yet? *Expert Rev Cardiovasc Ther*, 15(5):339–341, May 2017.

[80] Patrick M. Boyle, Stephane Mass, Kumaraswamy Nanthakumar, and Edward J. Vigmond. Transmural ik(atp) heterogeneity as a determinant of activation rate gradient during early ventricular fibrillation: mechanistic insights from rabbit ventricular models. *Heart Rhythm*, 10(11):1710–1717, Nov 2013.

[81] Eoin R Hyde, Jonathan M Behar, Simon Claridge, Tom Jackson, Angela W C Lee, Espen W Remme, Manav Sohal, Gernot Plank, Reza Razavi, Christopher A Rinaldi, and Steven A Niederer. Beneficial effect on cardiac resynchronization from left ventricular endocardial pacing is mediated by early access to high conduction velocity tissue: Electrophysiological simulation study. *Circ Arrhythm Electrophysiol*, 8(5):1164–72, Oct 2015.

[82] Andrew Atkinson, Shin Inada, Jue Li, James O Tellez, Joseph Yanni, Rakan Sleiman, Eman Abd Allah, Robert H Anderson, Henggui Zhang, Mark R Boyett, and Halina Dobrzynski. Anatomical and molecular mapping of the left and right ventricular his-purkinje conduction networks. *J Mol Cell Cardiol*, 51(5):689–701, Nov 2011.

[83] Elena Deza and Michel-Marie Deza. *Dictionary of Distances*. Elsevier, 2006.

[84] Milad El Haddad, Richard Houben, Roland Stroobandt, Frederic Van Heuverswyn, Rene Tavernier, and Mattias Duytschaever. Algorithmic detection of the beginning and end of bipolar electrograms: Implications for novel methods to assess local activation time during atrial tachycardia. *Biomedical*

Signal Processing and Control, 8(6):981 – 991, 2013.

[85] A. Alcaine, D. Soto-Iglesias, M. Calvo, E. Guiu, D. Andreu, J. Fernández-Armenta, A. Berruezo, P. Laguna, O. Camara, and J. P. Martínez. A wavelet-based electrogram onset delineator for automatic ventricular activation mapping. *IEEE Transactions on Biomedical Engineering*, 61(12):2830–2839, 2014.

[86] Christopher Reithmann, Anton Hahnefeld, Nico Oversohl, Michael Ulbrich, Thomas Remp, and Gerhard Steinbeck. Reinitiation of ventricular macroreentry within the his-purkinje system by back-up ventricular pacing - a mechanism of ventricular tachycardia storm. *Pacing Clin Electrophysiol*, 30(2):225–35, Feb 2007.

[87] J. A. Sethian. Fast marching methods. *SIAM Review*, 41(2):199–235, 1999.

[88] J P Keener. An eikonal-curvature equation for action potential propagation in myocardium. *J Math Biol*, 29(7):629–51, 1991.

[89] Corné Hoogendoorn, Rafael Sebastian, José Félix Rodriguez, Karim Lekadir, and Alejandro F Frangi. An atlas- and data-driven approach to initializing reaction-diffusion systems in computer cardiac electrophysiology. *Int J Numer Method Biomed Eng*, Aug 2017.

[90] A. Bubien R. Arciniegas J Orosio J., Rajandra. Continuous multi-electrode mapping: Single-center experience. *EP Lab Digest*, 16(1), 2016.

[91] Edward J Vigmond and Bruno D Stuyvers. Modeling our understanding of the his-purkinje system. *Prog Biophys Mol Biol*, 120(1-3):179–88, Jan 2016.

[92] Fernando Barber, Ignacio García-Fernández, Miguel Lozano, and Rafael Sebastian. Automatic estimation of purkinje-myocardial junction hot-spots from noisy endocardial samples: A simulation study. *International Journal for Numerical Methods in Biomedical Engineering*, 34(7):e2988, 2018. e2988 cnm.2988.

[93] Alejandro Lopez-Perez, Rafael Sebastian, M. Izquierdo, Ricardo Ruiz, Martin Bishop, and Jose M. Ferrero. Personalized cardiac computational models: From clinical data to simulation of infarct-related ventricular tachycardia. *Frontiers in Physiology*, 10:580, 2019.

[94] David Soto Iglesias, Nicolas Duchateau, Constantine Butakoff Kostantyn Butakov, David Andreu, Juan Fernandez-Armenta, Bart Bijnens, Antonio Berruezo, Marta Sitges, and Oscar Camara. Quantitative analysis of electro-anatomical maps: Application to an experimental model of left bundle branch block/cardiac resynchronization therapy. *IEEE J Transl Eng Health Med*, 5:1900215, 2017.

[95] Mei-Heng Yueh, Wen-Wei Lin, Chin-Tien Wu, and Shing-Tung Yau. An efficient energy minimization for conformal parameterizations. *Journal of Scientific Computing*, 73(1):203–227, 2017.

[96] R Sebastian, V Zimmerman, F Sukno, BB Bijnens, and AF Frangi. Cardiac modelling for pathophysiology research and clinical applications. the need for

an automated pipeline. In *World Congress on Medical Physics and Biomedical Engineering, September 7-12, 2009, Munich, Germany*, pages 2207–2210. Springer, 2009.

[97] Ana Ferrer-Albero, Eduardo J Godoy, Miguel Lozano, Laura Martínez-Mateu, Felipe Atienza, Javier Saiz, and Rafael Sebastian. Non-invasive localization of atrial ectopic beats by using simulated body surface p-wave integral maps. *PLoS One*, 12(7):e0181263, 2017.

[98] Kirsten H W J Ten Tusscher, Olivier Bernus, Rok Hren, and Alexander V Panfilov. Comparison of electrophysiological models for human ventricular cells and tissues. *Prog Biophys Mol Biol*, 90(1-3):326–345, 2006.

[99] Philip Stewart, Oleg V Aslanidi, Denis Noble, Penelope J Noble, Mark R Boyett, and Henggui Zhang. Mathematical models of the electrical action potential of purkinje fibre cells. *Philos Trans A Math Phys Eng Sci*, 367(1896):2225–55, Jun 2009.

[100] E Heidenreich, J M Ferrero, M Doblare, and J F Rodriguez. Adaptive macro finite elements for the numerical solution of monodomain equation in cardiac electrophysiology. *Annals of biomedical engineering*, 38:2331–2345, 2010.

[101] K Yano, T Keida, K Suzuki, T Sasano, K Hiejima, and K Okishige. Catheter ablation of idiopathic left ventricular tachycardia with multiple breakthrough sites guided by an electroanatomical mapping system. *J Interv Card Electrophysiol*, 5(2):211–4, Jun 2001.

[102] Guram Imnadze and Thomas Zerm. Prevention of ventricular fibrillation through de-networking of the purkinje system: Proof-of-concept paper on the substrate modification of the purkinje network. *Pacing Clin Electrophysiol*, 42(10):1285–1290, Oct 2019.

[103] Francisco Sahli Costabal, Daniel E Hurtado, and Ellen Kuhl. Generating purkinje networks in the human heart. *J Biomech*, 49(12):2455–65, 08 2016.

[104] Jesuliana N Ulysses, Lucas A Berg, Elizabeth M Cherry, Ben R Liu, Rodrigo W Dos Santos, Bruno G de Barros, Bernardo M Rocha, and Rafael A B de Queiroz. An optimization-based algorithm for the construction of cardiac purkinje network models. *IEEE Trans Biomed Eng*, 65(12):2760–2768, 12 2018.

[105] Elizabeth M. Cherry and Flavio H. Fenton. Contribution of the purkinje network to wave propagation in the canine ventricle: insights from a combined electrophysiological-anatomical model. *Nonlinear Dynamics*, 68(3):365–379, May 2012.

[106] Dongdong Deng, Adityo Prakosa, Julie Shade, Plamen Nikolov, and Natalia A Trayanova. Sensitivity of ablation targets prediction to electrophysiological parameter variability in image-based computational models of ventricular tachycardia in post-infarction patients. *Front Physiol*, 10:628, 2019.

[107] Jun-Ichi Okada, Katsuhito Fujiu, Takumi Washio, Seiryo Sugiura, Toshiaki Hisada, Eriko Hasumi, and Issei Komuro. Longitudinal dissociation and transition in thickness of the his-purkinje system cause various qrs waveforms

of surface ecg under his bundle pacing: A simulation study based on clinical observations. *J Cardiovasc Electrophysiol*, 30(11):2582–2590, Nov 2019.

[108] Mark E Silverman, Daniel Grove, and Charles B Upshaw, Jr. Why does the heart beat? the discovery of the electrical system of the heart. *Circulation*, 113(23):2775–81, Jun 2006.

[109] K Suma. Sunao tawara: a father of modern cardiology. *Pacing Clin Electrophysiol*, 24(1):88–96, Jan 2001.

[110] Andrew J Atkinson, Sanjay R Kharche, Michael G Bateman, Paul A Iaizzo, and Halina Dobrzynski. 3d anatomical reconstruction of human cardiac conduction system and simulation of bundle branch block after tavi procedure. *Conf Proc IEEE Eng Med Biol Soc*, 2016:5583–5586, 08 2016.